

**FEMTOSECOND LASER MICROFABRICATION OF SPIRAL OPTOFLUIDIC
SENSOR AND ITS SENSING APPLICATIONS**

by

© Xiaoxi Man

A Thesis submitted to the

School of Graduate Studies

in partial fulfillment of the requirements for the degree of

Master of Science

Department of Physics and Physical Oceanography

Memorial University of Newfoundland

December 2017

St. John's Newfoundland and Labrador

Abstract

Optofluidics combines the advantages of optics and microfluidics to achieve new functionalities. On account of cost-effectiveness, size-miniaturization, and structure-flexibility of optofluidic devices, there has been an increasing interest in optofluidics-related research since the emergence of the concept of optofluidics, such as lab-on-a-chip devices, optofluidic-based lenses and sensors, fluid-based particle sorters, optofluidic lasers, and imaging tools.

In this thesis, femtosecond laser is explored to study the nonlinear interactions between ultrashort laser pulses and photoresist materials, and the possible applications in optofluidics. Based on the effect of two-photon absorption occurred in transparent photoresist materials, spiral-shaped waveguides of different specifications are fabricated with femtosecond laser in photoresist SU-8-2. Each of the waveguides, which contains one bus waveguide and one spiral-shaped waveguide with a distinct circumference, can be integrated into one microchannel on a glass substrate to form a spiral optofluidic device as an optofluidic sensor. The sensor with the highest sensitivity is utilized to measure physical properties of various fluidic samples (calcium chloride, cow milk and its related products, non-diary milk, and sucrose). These properties include temperature, refractive index, positive pressure and concentration. Experimental results indicate that the highest sensitivities for fluidic measurement are -0.47 ± 0.02 nm/°C for temperature sensing, 188.78 ± 3.76 nm/RIU for refractive index sensing, 0.089 ± 0.03 nm/ (N/m²) for

positive pressure sensing, and 1.66 ± 0.06 nm/wt% for concentration sensing. All devices have been fabricated with the use of small-sized low-cost materials and easy-to-replicate fabrication techniques. The effectiveness and applicability of the spiral optofluidic devices demonstrated in this thesis revealed the significance of nonlinear optical interactions between ultrashort light pulses and photosensitive materials, and their importance in many applications.

Acknowledgement

I would like to express my sincere gratitude to my supervisor, Dr. Qiyang Chen, for his excellent guidance and continuous support throughout the entire process; for his patience, motivation, encouragement and immense knowledge; and for his teaching, attentive editing, and valuable research discussions. I am also grateful to my co-supervisor, Dr. Liqiu Men, for providing me with an excellent environment for doing research, for her valuable ideas, and for her being always caring, patient and supportive. I would like to thank all my group members, especially Dr. Daiying Zhang, who has been incredibly helpful to my research and has been like a sister to me. My gratitude also goes to my course instructors, Dr. Kristin Poduska and Dr. Mykhaylo Evstigneev and their interesting and useful lectures. I would like to thank Dr. Rick Goulding, Dr. G. Todd Andrews, Dr. Ivan Saika-voivod, and Dr. Entcho Demirov for choosing to work with me, for the delightful working experience, and friendship.

This thesis would have not been possible without the support from my family and friends, Xiuxiang, Baodong, Elisa, Andy, Clara, Amit, Julia, Lucia, Noah, Xiyu, Yubo, Wendy Song, Brianna, Taisa, and Tatsuo. I am deeply grateful to Grandpa Fukuan Man, who I always cherish in my heart.

I am greatly thankful to my parents, Yubing and Qingli, for supporting me to pursue what I want, for being the most positive persons in my life, and for always being the warm and guiding light in my life. Last but not least, I am thankful to my partner, Tomas Sanguinetti, for his endless worrying from my healthy diet to the grammar of my thesis; for taking care of my family, for sharing life with me, and for showing me the path through the entire process.

Table of Contents

Abstract	I
Acknowledgement	III
Table of Contents	IV
List of Tables	VI
List of Figures	VII
List of Abbreviations	XVI
Chapter 1 Introduction	1
1.1 Genesis of Optofluidics.....	1
1.2 Optofluidic sensing.....	3
1.2.1 Applications of Optofluidics in sensing device.....	3
1.2.2 Optofluidic sensing principles.....	5
1.2.2.1 Total internal reflection.....	6
1.2.2.2 Effective refractive index (RI).....	10
1.3 Femtosecond laser in Optofluidics.....	13
1.3.1 Femtosecond laser inscription.....	13
1.3.2 Nonlinear photon absorption induced by fs laser.....	17
1.3.2.1 Multi-photon absorption.....	17
1.3.2.2 Photolithography in photoresist materials.....	21
1.4 Wave-guiding Optofluidics.....	24
1.5 Optofluidics for bio-sensing applications.....	28
1.6 Thesis objectives.....	29
Chapter 2 Spiral Optofluidic Waveguide Sensors	31
2.1 Waveguide fabrication processes.....	31
2.1.1. General procedures for processing SU-8-2.....	32
2.1.2 Improved procedures for processing SU-8-2 waveguide.....	34
2.2 Waveguide microfabrication with femtosecond laser.....	36
2.2.1 Exposure conditions.....	36
2.2.2 Waveguide design.....	41

2.3 Fabrication of the microchannels	44
2.4 Experimental setup	47
2.5 Results and discussions	49
2.5.1 Transmission spectra of the spiral optofluidic sensor	49
2.5.2 Temperature sensing	51
2.5.3 Refractive index sensing	74
2.5.4 Positive pressure sensing	91
2.6 Comparison of the sensing performance of spiral waveguide sensors.....	107
2.7 Conclusion	110
Chapter 3 Spiral Optofluidic Sensors for Bio-sensing Applications	111
3.1 Refractive indices of cow milk products	111
3.2. Refractive indices of milk and milk-like products	119
3.3 Aging process of milk at room temperature	128
3.4. Refractive indices of sucrose solution	131
3.5 Conclusion.....	143
Chapter 4 Conclusions.....	146
4.1 Temperature sensing	147
4 .2 Refractive index and concentration sensing	147
4.3 Positive pressure sensing.....	148
4.4 Spiral optofluidic sensor for bio-sensing applications	149
4.5 Future research	149
Bibliography	151

List of Tables

Table 2-1 Optical path differences of single, double, triple, and quadruple-spiral waveguide sensor	51
Table 2-2 Refractive indices of CaCl ₂ solutions with different concentrations. The weight percentage (wt%) denotes the mass of solute divided by total mass of solution, expressed in percentage [156].....	74
Table 3-1 RI sensing of the milk samples from Brand S	115
Table 3-2 RI sensing of the milk samples from Brand C.....	118
Table 3-3 RI sensing of the milk and milk-like products.....	125
Table 3-4 RI of sucrose concentration sensing with single-spiral optofluidic waveguide sensor	134
Table 3-5 RI of sucrose concentration sensing with double-spiral optofluidic waveguide sensor	137
Table 3-6 RI of sucrose concentration sensing with triple-spiral optofluidic waveguide sensor	140
Table 3-7 RI of sucrose concentration sensing with quadruple-spiral optofluidic waveguide sensor	141
Table 3-8 Refractive indices of sucrose solutions [156].....	143
Table 3-9 Main compositions in cow milk (per 100 g) [171]	144

List of Figures

Figure 1-1 Growth in publications with titles that include the keyword “Optofluidic.” Data obtained from Google Scholar.	3
Figure 1-2 Phase diagram of total internal reflection at the interface of two media with different refractive indices	7
Figure 1-3 Comparison between two SU-8-2 waveguides when transmitting light: (a) creates massive light loss during transmission, and (b) can smoothly transmit light.	10
Figure 1-4 The first propagation mode and direction of the propagation constant in a classic sandwiched planar waveguide.....	12
Figure 1-5 Comparison of the heat-affected zones (HAZ) induced by long pulse laser and ultrashort laser.....	13
Figure 1-6 (a) High density of photons from ultrafast laser pulses; (b) low and constant photon density from long laser pulses	15
Figure 1-7 Microchannels fabricated by fs laser microfabrication in S1813 (Microchem [®] , USA) with the fabrication speed in (b) are 7, 5, and 3 $\mu\text{m/s}$, respectively (from the top to the bottom line).	16
Figure 1-8 Schematic illustration of photon absorptions and transitions. $\hbar\omega$ is the photon energy, where ω is the optical frequency.....	18
Figure 1-9 Schematic illustration of the nonlinear optical process caused by simultaneous absorption.....	20
Figure 1-10 Schematic illustration of laser induced photochemical reaction process in photoresist materials	22
Figure 1-11 Experimental comparison between positive-tone and negative-tone photoresists (after the same laser irradiation and developing process): a) Image of positive-tone photoresist S1813 (MicroChem [®] , USA) taken with 3D optical surface profiler (Zygo [®] , USA). The gaps are the laser-exposed areas and are completely washed	

off. b) Image of negative-tone photoresist SU-8-2 under microscope (Leica, USA). The laser-exposed areas are precisely kept on the substrate while the rest are all washed off. 23

Figure 2-1 Comparison on the refractive index of four common negative photoresists: SU-8-2 negative photoresist (MicroChem®, USA), SU-8-2000 series negative photoresist (MicroChem®, USA), KMPR 1000 chemically amplified negative photoresist (MicroChem®, USA), and UVN® 30 DUV negative photoresist (SHIPLEY®, USA). The Cauchy coefficients of the four most common negative photoresists were obtained from their suppliers [138–141].32

Figure 2-2 Typical procedures for processing SU-8-2.....33

Figure 2-3 Experimental setup of fs laser microfabrication in this study. S is a shutter; P is the polarizer; S1 is the monitor which is connected to the CCD camera (Panasonic KR222, Japan); S2 is the computer that is connected to the motion stage; O is an objective lens (Leica, USA)37

Figure 2-4 A photo of the focusing process with the help of the objective lens-CCD Camera display system38

Figure 2-5 Effect of fs laser focusing conditions during SU-8-2 fabrication: (a) An SU-8-2 waveguide fabricated by fs laser focused onto its surface, (b) an SU-8-2 waveguide with a burnt area when the laser is focused on the bottom of the SU-8-2 film.....39

Figure 2-6 Effect of the duration of fs laser exposure on SU-8-2 thin film on the area of cross linkage, fs laser is focused with a 50× objective lens: (a) exposure duration is in the unit of millisecond (ms). The longest exposure duration is 4750 ms (bottom right dot), and the shortest exposure duration is 1000 ms (top left dot), and (b) Effect of the scan speed of the fs laser, the scan speeds are 10, 7, 5, 2, 1 μm/s.40

Figure 2-7 Design of the spiral waveguide with the sensing window shown in the rectangular shadow41

Figure 2-8 Microscopic images of the four spiral waveguides with the total lengths of the spiral curves of (a) 376.99; (b) 1096.73; (c) 2261.95; and (d) 3769.91 μm, respectively. 43

Figure 2-9 Soft lithography process to fabricate PDMS microchannel45

Figure 2-10 Waveguide-microchannel optofluidic system46

Figure 2-11 Experimental setup for sensing with the spiral waveguide sensor47

Figure 2-12 Experimental setup for achieving optimal coupling of the sensor	48
Figure 2-13 Original transmission spectra of spiral waveguide sensors with the total lengths of the spiral curves are 376.99, 1096.73, 2261.95, and 3769.91 μm , respectively.	49
Figure 2-14 Transmission spectra of the quadruple-spiral waveguide sensor with the background removed.....	50
Figure 2-15 (a) Image of the single-spiral waveguide; (b) 3D profiler image of the single-spiral waveguide. The width of the waveguides in this sensor is 5.724 μm	53
Figure 2-16 Near-filed image of Coupled light transmitted by the spiral waveguide shown in Fig. 2-15.	53
Figure 2-17 Temperature dependences of the transmission spectra of the single-spiral waveguide sensor.	54
Figure 2-18 Shifts of the peak wavelengths with an initial value at 1553.02 nm in the transmission spectra of temperature sensing by the single-spiral waveguide sensor	55
Figure 2-19 Shifts of the peak wavelengths with an initial value at 1565.97 nm in the transmission spectra of temperature sensing by the single-spiral waveguide sensor	56
Figure 2-20 Shifts of the peak wavelengths with an initial value at 1581.09 nm in the transmission spectra of temperature sensing by the single-spiral waveguide sensor	57
Figure 2-21 Shifts of the peak wavelengths with an initial value at 1598.91 nm in the transmission spectra of temperature sensing by the single-spiral waveguide sensor	57
Figure 2-22 (a) Image of the double-spiral waveguide (b) 3D profiler image of the double-spiral waveguide. The width of this group of waveguides is 5.872 μm	58
Figure 2-23 Near-filed image of Coupled light transmitted by the spiral waveguide shown in Fig. 2-22	59
Figure 2-24 Temperature dependence of the transmission spectra of the double-spiral waveguide sensor	60
Figure 2-25 Shifts of the valley wavelengths with an initial value at 1556.38 nm in the transmission spectra of temperature sensing by the double-spiral waveguide sensor	60
Figure 2-26 Shifts of the valley wavelengths with an initial value at 1573.82 nm in the transmission spectra of temperature sensing by the double-spiral waveguide sensor	61

Figure 2-27 Shifts of the valley wavelengths with an initial value at 1592.09 nm in the transmission spectra of temperature sensing by the double-spiral waveguide sensor	62
Figure 2-28 (a) Microscopic image, and (b) 3D profiler image of the triple-spiral waveguide. The width of the waveguide in the triple-spiral sensor is 6.918 μm	63
Figure 2-29 Near-field image of coupled light transmitted by the spiral waveguide shown in Fig. 2-28.....	63
Figure 2-30 The temperature dependence of the transmission spectra of the triple-spiral waveguide sensor	64
Figure 2-31 Shifts of the valley wavelengths with an initial value at 1557.92 nm in the transmission spectra of temperature sensing by the triple-spiral waveguide sensor	65
Figure 2-32 Shifts of the valley wavelengths with an initial value at 1570.54 nm in the transmission spectra of temperature sensing by the triple-spiral waveguide sensor	66
Figure 2-33 Shifts of the valley wavelengths with an initial value at 1581.46 nm in the transmission spectra of temperature sensing by the triple-spiral waveguide sensor	66
Figure 2-34 Near-field image of coupled light transmitted by the spiral waveguide shown in Fig. 2-35.....	67
Figure 2-35 (a) & (b) Microscopic image of the quadruple-spiral waveguide, and (c) is the 3D profiler image of the quadruple-spiral waveguide.	68
Figure 2-36 Temperature dependence of the transmission spectra of the quadruple-spiral waveguide sensor	69
Figure 2-37 Shifts of the valley wavelengths with an initial value at 1537.24 nm in the transmission spectra of temperature sensing by the quadruple-spiral waveguide sensor ..	70
Figure 2-38 Shifts of the valley wavelengths with an initial value at 1550.45 nm in the transmission spectra of temperature sensing by the quadruple-spiral waveguide sensor ..	71
Figure 2-39 Shifts of the valley wavelengths with an initial value at 1564.34 nm in the transmission spectra of temperature sensing by the quadruple-spiral waveguide sensor ..	72
Figure 2-40 Shifts of the valley wavelengths with an initial value at 1577.55 nm in the transmission spectra of temperature sensing by the quadruple-spiral waveguide sensor ..	73
Figure 2-41 Shifts of the valley wavelengths with an initial value at 1588.29 nm in the transmission spectra of temperature sensing by the quadruple-spiral waveguide sensor ..	73

Figure 2-43 Shifts of the valley wavelengths with an initial value at 1567.28 nm in the transmission spectra of RI sensing by the single-spiral waveguide sensor	77
Figure 2-44 Shifts of the peak wavelengths with an initial value at 1575.69 nm in the transmission spectra of RI sensing by the single-spiral waveguide sensor	77
Figure 2-45 Shifts of the valley wavelengths with an initial value at 1583.71 nm in the transmission spectra of RI sensing by the single-spiral waveguide sensor	78
Figure 2-46 Shifts of the valley wavelengths with an initial value at 1601.15 nm in the transmission spectra of RI sensing by the single-spiral waveguide sensor	79
Figure 2-47 The RI dependence of the transmission spectra of the double-spiral waveguide sensor	80
Figure 2-48 Shifts of the valley wavelengths with an initial value of 1549.49 nm in the transmission spectra of RI sensing by the double-spiral waveguide sensor	81
Figure 2-49 Shifts of the valley wavelengths with an initial value at 1571.43 nm in the transmission spectra of RI sensing by the double-spiral waveguide sensor	82
Figure 2-50 The RI dependence of the transmission spectra of the triple-spiral waveguide sensor	83
Figure 2-51 Shifts of the valley wavelengths with an initial value at 1533.55 nm in the transmission spectra of RI sensing by the triple-spiral waveguide sensor.....	84
Figure 2-52 Shifts of the valley wavelengths with an initial value at 1546.84 nm in the transmission spectra of RI sensing by the triple-spiral waveguide sensor.....	84
Figure 2-53 Shifts of the valley wavelengths with an initial value at 1569.89 nm in the transmission spectra of RI sensing by the triple-spiral waveguide sensor.....	85
Figure 2-54 Shifts of the valley wavelengths with an initial value at 1583.75 nm in the transmission spectra of RI sensing by the triple-spiral waveguide sensor.....	86
Figure 2-55 The RI dependence of the transmission spectra of the quadruple-spiral waveguide sensor	87
Figure 2-56 Shifts of the valley wavelengths with an initial value at 1546.16 nm in the transmission spectra of RI sensing by the quadruple-spiral waveguide sensor	88
Figure 2-57 Shifts of the valley wavelengths with an initial value at 1560.14 nm in the transmission spectra of RI sensing by the quadruple-spiral waveguide sensor	89

Figure 2-58 Shifts of the valley wavelengths with an initial value at 1573.46 nm in the transmission spectra of RI sensing by the quadruple-spiral waveguide sensor	90
Figure 2-59 Shifts of the valley wavelengths with an initial value at 1585.00 nm in the transmission spectra of RI sensing by the quadruple-spiral waveguide sensor	90
Figure 2-60 Experimental setup for positive pressure sensing	92
Figure 2-61 Microscopic image of the spiral sensor with water-filled microchannel	92
Figure 2-62 Positive pressure dependence of the transmission spectra of the single-spiral waveguide sensor	93
Figure 2-63 Shifts of the peak wavelengths with an initial value at 1534.06 nm in the transmission spectra of positive pressure sensing by the single-spiral waveguide sensor	94
Figure 2-64 Shifts of the peak wavelengths with an initial value at 1557.53 nm in the transmission spectra of positive pressure sensing by the single-spiral waveguide sensor	95
Figure 2-65 Shifts of the peak wavelengths with an initial value at 1572.98 nm in the transmission spectra of positive pressure sensing by the single-spiral waveguide sensor	95
Figure 2-66 Shifts of the peak wavelengths with an initial value at 1586.22 nm in the transmission spectra of positive pressure sensing by the single-spiral waveguide sensor	96
Figure 2-67 Positive pressure dependence of the transmission spectra of the double-spiral waveguide sensor	97
Figure 2-68 Shifts of the valley wavelengths with an initial value at 1529.23 nm in the transmission spectra of positive pressure sensing by the double-spiral waveguide sensor	97
Figure 2-69 Shifts of the valley wavelengths with an initial value at 1556.70 nm in the transmission spectra of positive pressure sensing by the double-spiral waveguide sensor	98
Figure 2-70 Shifts of the valley wavelengths with an initial value at 1574.84 nm in the transmission spectra of positive pressure sensing by the double-spiral waveguide sensor	99
Figure 2-71 Positive pressure dependence of the transmission spectra of the triple-spiral waveguide sensor	100
Figure 2-72 Shifts of the peak wavelengths with an initial value at 1537.28 nm in the transmission spectra of positive pressure sensing by the triple-spiral waveguide sensor	101
Figure 2-73 Shifts of the peak wavelengths with an initial value at 1547.65 nm in the transmission spectra of positive pressure sensing by the triple-spiral waveguide sensor	101

Figure 2-74 Shifts of the peak wavelengths with an initial value at 1559.27 nm in the transmission spectra of positive pressure sensing by the triple-spiral waveguide sensor	102
Figure 2-75 Shifts of the peak wavelengths with an initial value at 1580.84 nm in the transmission spectra of positive pressure sensing by the triple-spiral waveguide sensor	103
Figure 2-76 Shifts of the peak wavelengths with an initial value at 1590.48 nm in the transmission spectra of positive pressure sensing by the triple-spiral waveguide sensor	103
Figure 2-77 Positive pressure dependence of the transmission spectra of the quadruple-spiral waveguide sensor	104
Figure 2-78 Shifts of the peak wavelengths with an initial value at 1538.84 nm in the transmission spectra of positive pressure sensing by the quadruple-spiral waveguide sensor	105
Figure 2-79 Shifts of the peak wavelengths with an initial value at 1570.05 nm in the transmission spectra of positive pressure sensing by the quadruple-spiral waveguide sensor	106
Figure 2-80 Shifts of the peak wavelengths with an initial value at 1581.90 nm in the transmission spectra of positive pressure sensing by the quadruple-spiral waveguide sensor	106
Figure 2-81 Comparison on temperature sensitivities of the four spiral waveguide sensors	108
Figure 2-82 Comparison on RI sensitivities of the four spiral-shaped waveguide sensors	109
Figure 2-83 Comparison on positive pressure sensitivities of the four spiral waveguide sensors	109
Figure 3-1 A series of dairy and non-dairy products which are available in local stores in St. John's.....	112
Figure 3-2 Transmission spectra of five milk samples of Brand S with different fat percentages indicated inside the figure.	113
Figure 3-3 (a) – (e) shifts in the peak wavelengths of the triple-spiral waveguide sensor on testing five milk samples (0%, 0.5%, 1%, 2%, and 3.25%) of Brand S; (f) comparison on the results from these five milk samples.....	114

Figure 3-4 Transmission spectra of five milk samples of Brand C with different fat percentages indicated inside the figure.	116
Figure 3-5 (a) – (e) shifts in the peak wavelengths of the triple-spiral waveguide sensor on testing five milk samples (0%, 0.5%, 1%, 2%, and 3.25%) of Brand C; (f) comparison on the results from these five milk samples.	117
Figure 3-6 Transmission spectra of the original unsweetened coconut milk compared with that of the 0% and 3.25% milk of Brand S	120
Figure 3-7 Transmission spectra of the original unsweetened almond milk compared with that of the 0% and 3.25% milk of Brand S	120
Figure 3-8 Transmission spectra of the original unsweetened coconut milk compared with that of the 0% and 3.25% milk of Brand C	121
Figure 3-9 Transmission spectra of the original unsweetened almond milk compared with that of the 0% and 3.25% milk of Brand C	121
Figure 3-10 Transmission spectra of the original unsweetened almond and coconut 1:1 blend compared with that of the unsweetened coconut milk and unsweetened almond milk	122
Figure 3-11 Transmission spectra of Brand L lactose free milk compared with that of the 0% and 3.25% milk of Brand S	122
Figure 3-12 Transmission spectra of Brand L lactose free milk compared with that of the 0% and 3.25% milk of Brand C	123
Figure 3-13 Transmission spectra of raw farm milk compared with that of the 3.25% milk of Brand S and Brand C	123
Figure 3-14 Transmission spectra of the 0% lactose free milk from Brand L compared with that of the 2% lactose free milk from Brand N	124
Figure 3-15 Transmission spectra of the 2% lactose free milk from Brand L and N compared with that of the 2% milk from Brand S	124
Figure 3-16 Transmission spectra of the 1% organic cow milk of Brand N and its non-organic counterparts by a triple-spiral waveguide sensor	126
Figure 3-17 Transmission spectra of the evaporated skim cow milk compared with the 0% and 3.25% cow milk from Brand S by a triple-spiral waveguide sensor	127

Figure 3-18 Transmission spectra of the evaporated skim cow milk compared with the 0% and 3.25% cow milk from Brand C by a triple-spiral waveguide sensor	127
Figure 3-19 Transmission spectra of aging 3.25% homogenized cow milk kept at room temperature	128
Figure 3-20 Transmission spectra of aging raw farm milk kept at room temperature....	129
Figure 3-21 Changes in refractive indices of both the raw farm milk and the homogenized milk during aging process	130
Figure 3-22 Coupled light transmitted by the single-spiral waveguide sensor passing through sucrose solution	131
Figure 3-23 Shifts in transmission spectra of the single-spiral waveguide sensor with sucrose solutions of different concentrations.....	132
Figure 3-24 (a) – (e) Resonance peak shifts, and (f) comparison of peak shifts of single-spiral waveguide sensor for sucrose concentration sensing.....	133
Figure 3-25 Shifts in transmission spectra of the double-spiral waveguide sensor with sucrose solutions of different concentrations.....	135
Figure 3-26 (a) – (d) resonance peak shifts, and (e) comparison of peak shifts of double-spiral waveguide sensor for sucrose concentration sensing.....	136
Figure 3-27 Shifts in transmission spectra of the triple-spiral waveguide sensor with sucrose solutions of different concentrations.....	138
Figure 3-28 (a) – (d) Resonance peak shifts, and (e) comparison of peak shifts of triple-spiral waveguide sensor for sucrose concentration sensing.....	139
Figure 3-29 Shifts in transmission spectra of the quadruple-spiral waveguide sensor with sucrose solutions of different concentrations.....	141
Figure 3-30 (a) – (e) Resonance peak shifts, and (f) comparison of peak shifts of quadruple-spiral waveguide sensor for sucrose concentration sensing	142

List of Abbreviations

fs laser	Femtosecond laser
HAZ	Heat-affected zones
HF	Hydrofluoric Acid
TPP	Two-photon polymerization
MZI	Mach-Zehnder Interferometer
MPA	Multi-photon absorption
OSA	Optical spectrum analyzer
PCF	Photonic crystal fiber
PC	Polycarbonate
PDMS	Polydimethylsiloxane
PMMA	Polymethyl-methacrylate
PS	Polystyrene
RI	Refractive index
RIU	Refractive index unit
SMF	Single mode fiber
TOC	Thermo-optic coefficient
TIR	Total internal reflection
TPA	Two-photon absorption

Chapter 1 Introduction

This chapter provides an overview of the field of optofluidics, followed by an introduction to the sensing applications of optofluidic devices and the fundamentals of wave-guiding, sensing, and fluidic behaviors in waveguide microchannel chips. In addition, waveguide fabrication with femtosecond laser and its related fabrication mechanisms are reviewed. The objective of this thesis is presented at the end of this chapter.

1.1 Genesis of Optofluidics

Optofluidics emerged nearly one decade ago with the aim of miniaturization and integration of bulky lab equipment into compact devices in order to reduce reagent consumption [1] and waste in chemical reactions [2]. Microchips with a size smaller than a palm are capable of functioning as miniaturization devices. Optical, mechanical, and electrical microcomponents can be incorporated and integrated into microchips to achieve a miniature version of a lab [3–5]. This is of importance as laboratory miniaturization means not only less labor cost, but also higher efficiency in fields such as medical inspection and biological analysis [6–9].

To satisfy these demands, various microchip-based systems have been developed, including lab-on-a-chip devices [10–12], microreactors [13, 14], μ -TAS (micro-total analysis system) [15, 16], microfluidic systems [17–19] and optofluidic systems [20–22].

In particular, optofluidic systems have developed rapidly due to its versatility and adaptability. The hybrid of solid structure and liquid injection can easily control the propagation of light by manipulating fluids [23]. By changing liquids with different optical properties, various applications have been realized such as optofluidic optical switch, particle counter, optofluidic sensor, and optofluidic micro-spectroscopy [24–27]. The solid part of the optofluidic system can also be substituted with liquid. Due to their high flexibility, liquid-in-liquid optofluidic systems have multiple applications such as optofluidic lenses created by confining two immiscible liquids into one channel, and optical splitters using miscible liquids [3, 28, 29].

Optofluidics has evolved to be an exciting research field, and its applicability for different purposes has been widely studied [5, 30–32]. This development further confirms that the combination of fluidic microsystems with optical components, mechanical components, and/or electromagnetic components has enabled microchips to achieve high sensitivity, high accuracy, and high flexibility. In particular, the fusion of optics and microfluidics for the analysis of multiple types of fluids has overcome many obstacles facing free-space optics for decades. One prominent success in optofluidics is the integration of waveguides into optofluidic systems to realize the manipulation and transformation of light [33]. In 2013, Pao *et al.* fabricated a slot waveguide device and made use of the effect of discontinuity of the evanescent field to realize on-chip chemical sensing in the mid-IR region [34]. In a separate study, a jet waveguide-based optofluidic sensor was developed for the use as fluorescence spectroscopy, which achieved the detection of pollutants in water [35]. Benelarbi *et al.* fabricated a photonic

crystal waveguide sensor with engraved ring-shaped holes to accomplish high sensitive RI infiltration [36].

The synergy of fluids and optics has made it possible to develop highly tunable and versatile applications based on optofluidic techniques. As seen in Fig. 1-1, the increase in the number of publications on optofluidics reveals the potential of the field as a new framework for the creation of new integrated, multi-functional micro-devices.

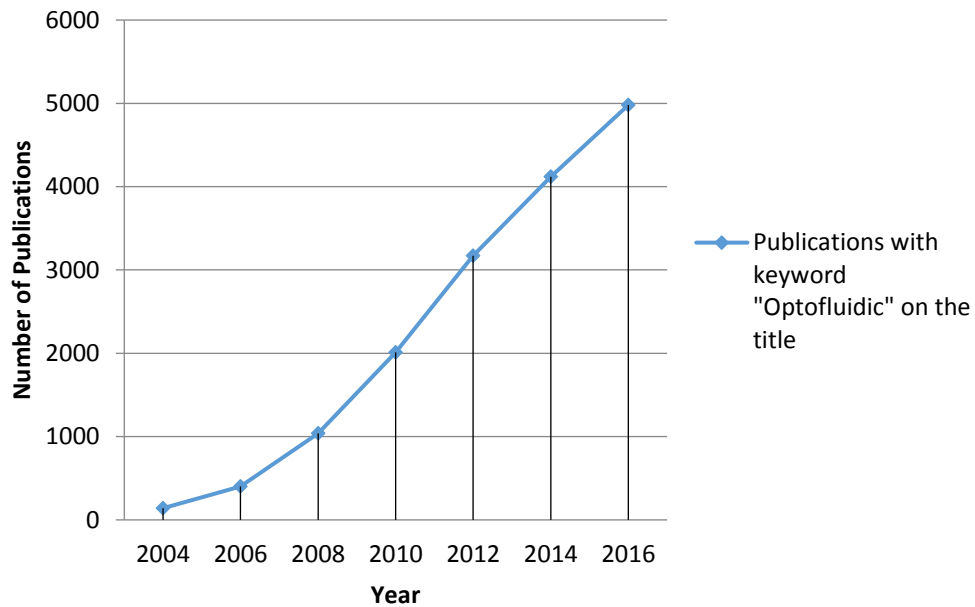


Figure 1-1 Growth in publications with titles that include the keyword “Optofluidic.” Data obtained from *Google Scholar*.

1.2 Optofluidic sensing

1.2.1 Applications of Optofluidics in sensing devices

The significance of optofluidic sensors with high sensitivity has been widely

acknowledged in academia as well as in various industrial fields due to their far-reaching applications in food sciences [37], biochemical analysis [38] and environmental technologies [39]. Before the advent of optofluidic sensors, various conventional sensors had been developed and utilized for decades for different applications. For example, pregnancy tests are based on the principle that the substrate of the test kit is sensitive to human chorionic gonadotropin, a hormone produced only by pregnant women [40]. The optical property of the test kit changes when encountering the “pregnancy hormone,” showing whether fertilization has taken place or not. A second example of a conventional sensor is the blood sugar test, which is based on the electrochemical reaction between an enzyme and the diabetes test kit [41]. Fluid-testing based sensors are broadly used and often based on optical principles. This is mainly due to the fact that devices that utilize optical effects take less time and provide more reliable results. In addition, light is weightless and easy to transmit and is almost harmless to the samples analyzed.

However, the use of conventional fluid sensors is restricted to limited types of fluids. In most cases, a sensor is developed for one specific fluid. Most conventional sensors come in larger sizes; smaller sensors are usually disposable and create significant waste [42]. In addition, large amounts of reagent are required to obtain reliable results. The environmental and economic needs for reducing laboratory waste and producing devices with higher portability and reusability led scientists to find new ways to modulate light. Consequently, this gave way to the integration of optic and microfluidics into the new field of optofluidics, and the subfield of optofluidic sensing devices.

Since the advent of optofluidics, different types of optofluidic sensors have been developed and used for multiple sensing applications. One such device is a photonic

crystal fiber (PCF), a hollow-core wave-guiding medium that is thicker than conventional fibers [43]. PCF is an ideal candidate as an optofluidic sensor due to its reconfigurability: as liquids are injected into the core of the PCF, its optical property changes completely. Ertman *et al.* fabricated a fully filled photonic crystal fiber optofluidic sensor and accomplished temperature sensing, refractive index (RI) sensing, and mechanical properties sensing of fluid samples [44]. In a different study, a double-layered photonic crystal microcavity device was utilized as a pressure sensor: when pressure was added to the device, a shift in the transmission spectra of the sensor allowed for the calculation of the weight change [45]. Sensing can also be achieved when an optofluidic sensor is integrated with a single-mode fiber (SMF) through the use of strong light signal, as demonstrated by Yan and Xu [46].

1.2.2 Optofluidic sensing principles

The mechanism of optofluidic devices have made them highly capable as sensors [4]. In this study, light is confined in the waveguide which is surrounded by liquids. The transmission spectrum of the guided light adapt to different types of liquid surroundings is the sensing mechanism in this study. The fundamental principle behind optical confinement in any type of light-guiding devices is total internal reflection [47]. This applies to all kinds of optical fibers and waveguides, including microchannel-based optofluidic devices. The idea is to guide the light through the inner media without diffusing any power into the surrounding medium. The physical properties and

mechanisms involved in the successful confinement and propagation of light in a wave-guided structure is introduced below.

1.2.2.1 Total internal reflection

In microchannel-based optofluidic devices, choices for cores and claddings can vary from the type of materials to the different phases of a material [48, 49]. Notwithstanding, there are three commonly used combinations of core and cladding materials in the field of optofluidics: solid core with liquid cladding [50]; liquid core with solid cladding [51]; and liquid core with liquid cladding [52]. In any of the cases listed above, total internal reflection (TIR) is the key criterion for choosing cores and claddings materials. A successful combination of materials is one in which a guided light that is transmitted through the core material bounces against the interface and back without any light refraction.

At the interface of the core and cladding materials, an incident plane electromagnetic wave is transmitted. The wave has the form

$$\vec{E}(\vec{x}, I, R, T) = E_0(I) \cdot e^{-j(\vec{k}_{||, R, T} \cdot \vec{x} - \omega t)} \quad (1.1)$$

where \vec{E} stands for the electric field, \vec{x} is the location vector, t is time, $\vec{k}_{||}$ is the sinusoidal projection of the wave vector \vec{k} on the interface, as can be seen in Fig. 1-2. I , R , T represents incident, reflected, and transmitted waves, respectively.

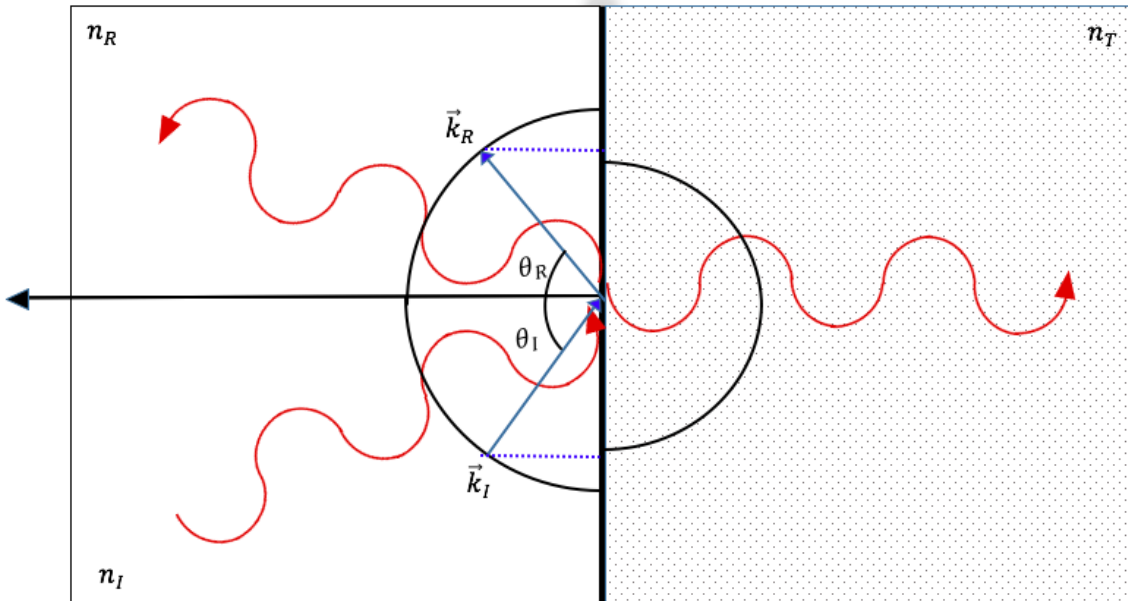


Figure 1-2 Phase diagram of total internal reflection at the interface of two media with different refractive indices

All the wave vectors mentioned are influenced by the refractive index of the propagation media in the same way

$$\vec{k}_\alpha = n_\alpha \vec{k}_0 \quad (1.2)$$

where $\alpha = I, R, T, n_\alpha$ are the refractive indices and \vec{k}_0 is the wave vector in vacuum.

It is shown from the wave equation (1.1) that the position dependence of the incident plane wave is $e^{(i\vec{k}_\alpha \cdot \vec{x})}$. This implies that the incident, reflected, and transmitted waves should all have identical wave vectors on the plane of the interface

$$k_I \sin q_I = k_R \sin q_R = k_T \sin q_T \quad (1.3)$$

where θ_T is the transmission or refraction angle. During the wave propagation, the reflected wave has the same wave number $\vec{k}_R = \vec{k}_I$ as the incident wave, as both waves are solutions of the same wave equation. Whereas for the transmitted wave, of which the wave number is determined by the refractive index of the transmission medium, it follows that

$$k_T = \frac{\omega \sqrt{\epsilon_T \mu_T}}{c} \quad (1.4)$$

There are two conditions under which, if satisfied, total internal reflection would occur. The first condition is that the refractive index of the transmission medium (n_T) is smaller than that of the reflection medium (n_R). The second condition is that the angle of the incident wave is larger than the critical angle ($\theta_{critical}$). The second condition can be expressed as

$$n \sin \theta_I > n_T \quad (1.5)$$

derived as

$$|k \sin \theta_I| > |k_T| \quad (1.6)$$

which means that the tangential projection of the wave vector of the incident wave is larger than the magnitude of the transmission wave vector. If the two components of the transmission wave are $k_{T,t}$ (tangential component into the interface) and $k_{T,n}$ (normal component to the interface), $k_{T,t}$ and $k_{T,n}$ must satisfy

$$k_{T,t}^2 + k_{T,n}^2 = \frac{W^2 n_T^2}{c^2} \quad (1.7)$$

where

$$k_{T,t} > \frac{W n_T}{c} \quad (1.8)$$

This means that $|k_{T,n}^2|$ must be a negative magnitude which, in turn, indicates that $k_{T,n}$ is imaginary. This brings a new form of the wave equation:

$$\vec{E}'(\vec{x}, I, R, T) = E'_0(I) \cdot e^{i(\vec{k}_{T,t} \cdot \vec{x} - \omega t)} e^{-|\vec{k}_{T,n}|z} \quad (1.9)$$

The Poynting vector for this equation is described as

$$\vec{S}_{T,z} = \frac{c}{8\pi} \Re(\vec{E}' \times \vec{B}'^*) \quad (1.10)$$

Equations (1.9) and (1.10) result in

$$\vec{S}_{T,z} = \frac{c}{8\pi} \Re \left(-E_{T,y} E_{T,y}^* \frac{c|k_{T,n}|}{-i\omega} \right) = 0 \quad (1.11)$$

which proves that if the incident angle of a plane wave is larger than the critical angle of Snell's Law, there will be no plane wave in the medium of transmission. The evaluation of the Poynting vector (Eq. 1.11) indicates that TIR happens when the light power is not refracted but is entirely reflected by the interface. The phenomenon of total internal reflection of any surface wave along with its energy during propagation is widely utilized in guided-optical sciences [53–57].

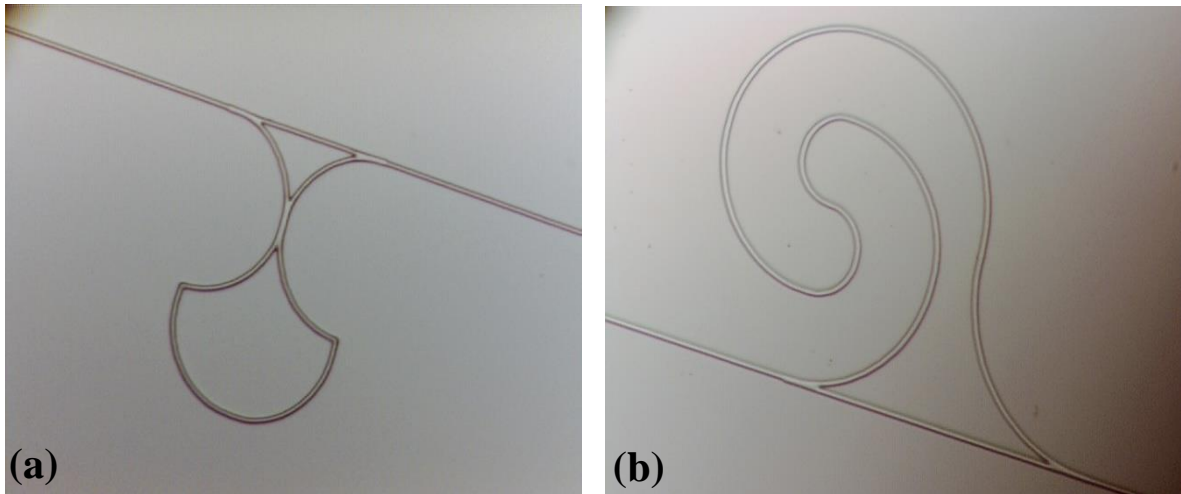


Figure 1-3 Comparison between two SU-8-2 waveguides when transmitting light: (a) creates massive light loss during transmission, and (b) can smoothly transmit light.

As a result, a beam of light can travel in a wave-guiding device ($RI_{Core} > RI_{Cladding}$) for long distance and along various curvatures. However, to reduce light loss, the shape of the waveguide should always avoid sharp turns. For instance, in Fig. 1-3, the shape of the waveguide in (a) will induce massive energy loss when the light reaches the sharp turns, while in (b), light is able to travel through all the curves with the only loss caused by potential imperfections in the guiding material or coating process.

1.2.2.2 Effective refractive index (RI)

The effective RI describes the change in refractive index of a material affected by the variation of external and internal factors such as temperature, pressure, electrical property, phase transition, elasticity, and by changes in the mode of light propagation. Since the first applications of optofluidic technology [58–64], many studies on optofluidic sensors

have been based on the concept of effective refractive index. Michael *et al.* developed a more accurate method to measure the physical properties of a material by only monitoring the Fabry-Perot resonance wavelength shifts [65]. In a different study, Wan *et al.* designed a single-mode fiber and microchannel hybrid system to realize optical attenuation with a large attenuation range from visible to near infrared [66]. Recently, a laser-induced optofluidic tunable lens with fast tuning speed and aberration-free focusing was designed and applied based on the effective refractive index theory by altering the thermo-gradient field [67].

The refractive index of an optical material, n , measures the bending of the incident ray of light from one medium to another medium. The index of refraction of a material is decided by the frequency of the incident light f , the relative permittivity ϵ_r and relative permeability μ_r :

$$n(f, \epsilon_r, \mu_r) = \sqrt{\epsilon_r(f) \mu_r(f)} \quad (1.12)$$

The relative permittivity represents the ratio of the electrical field between a pair of two-point charges in a material to that in a vacuum. The relative permeability is the comparison between the ability of a material to maintain its original magnetic field in the medium and in a vacuum. Therefore, the index of refraction n can quantify the change of a *unit phase* (phase per unit length, or wavenumber) caused by the medium:

$$k = nk_0 \quad (1.13)$$

The concept of *effective refractive index* is closely correlated to the propagation constant β , which, in a planar waveguide, refers to the variations of the phase and amplitude of the incident light along the direction of waveguide propagation

$$b = k_0 n_{eff} = \frac{2\rho}{l_0} n_{eff} \quad (1.14)$$

The reason for this is that, in a wave-guiding device with known polarization and mode, the propagation constant β is the wavenumber k in the given propagation direction, as shown in Fig. 1-4.

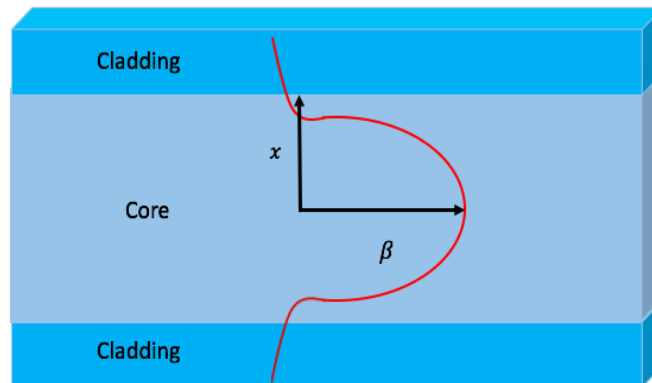


Figure 1-4 The first propagation mode and direction of the propagation constant in a classic sandwiched planar waveguide

Therefore, effective refractive index does not only depend on the electromagnetic property of the material itself, but it also depends on the entire design of the waveguide, which determines the way of propagation of the incident light.

1.3 Femtosecond laser in Optofluidics

1.3.1 Femtosecond laser inscription

Femtosecond laser is the main tool for waveguide fabrication in this study. Femtosecond laser (fs laser) emits optical pulses with a duration well below 1 ps (ultrashort pulses), which generates a negligible heat-affected zone, compared with long-pulse lasers [68] (explained in Fig. 1-5). This is a prominent advantage of femtosecond laser micromachining, especially when high resolution [69] and ultra-precision [70] are required.

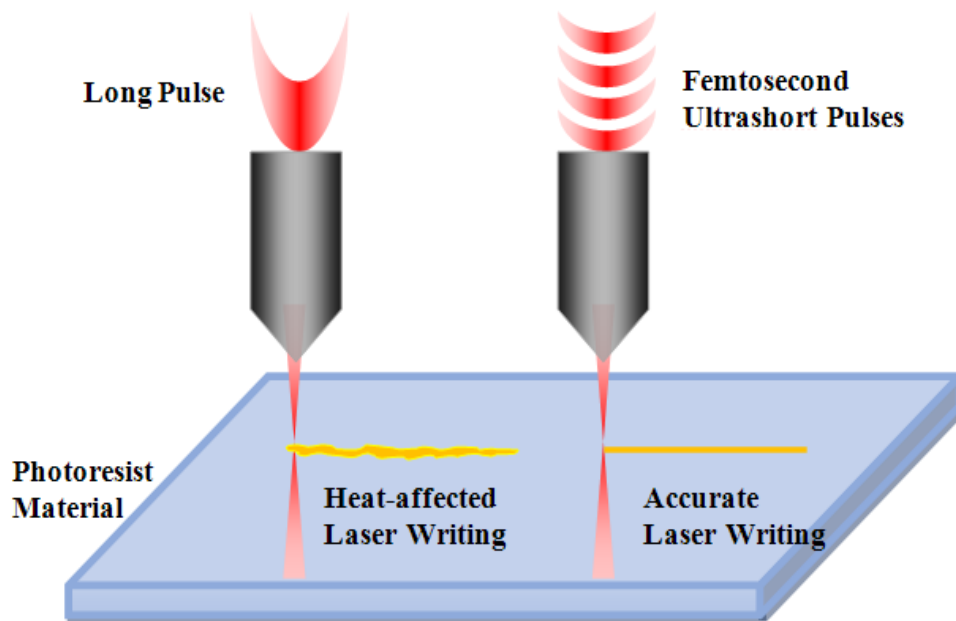


Figure 1-5 Comparison of the heat-affected zones (HAZ) induced by long pulse laser and ultrashort laser

This unique property of femtosecond laser has made it an attractive fabrication tool in all subfields of optofluidics. This is illustrated by a number of studies using fs laser microfabrication. Maselli *et al.* [71] fabricated microchannel and Bragg Grating waveguides simultaneously using femtosecond laser, and integrated them onto fused silica to create an optofluidic evanescent-field-sensing system. Bragheri *et al.* developed a fiber-based on-chip optofluidic system with single-cell stretching and controlling [72]. Dong *et al.* created a 2D-3D micro-optical structure on glass and 3D embedded microchannels to achieve a system with high accuracy and coupling-free cell counting [73]. Zhang, *et al.* achieved various microchannel and SU-8 waveguide structures that can be used as temperature and refractive index sensors, particle sorters and color filters [74, 75]. On-fiber fs-laser microfabrication of a sensor based on Mach-Zehnder Interferometer with high sensitivity was achieved by Ping and Chen [75]. Despite these studies using fs laser microfabrication, an on-chip, highly compact optofluidic waveguide sensor with controllable sensitivity has not yet been achieved. Figure 1-5 clearly illustrates the area differences of heat affected zones between long pulse lasers and ultrashort pulse lasers.

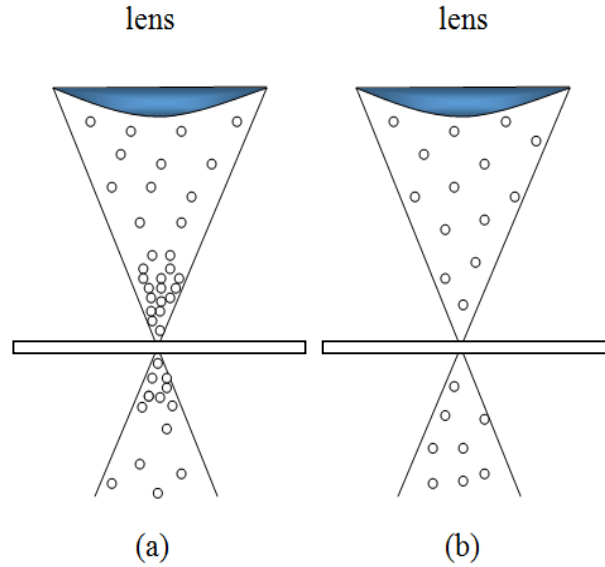


Figure 1-6 (a) High density of photons from ultrafast laser pulses; (b) low and constant photon density from long laser pulses

In addition, femtosecond laser generates extremely high peak photon density [77–79], which enables the realization of multi-photon absorption [79]. Without high peak density of photons, only single photon absorption can be induced. As is shown in Fig. 1.6 (a), femtosecond laser generates ultrashort pulses with extremely high photon density within each pulse.

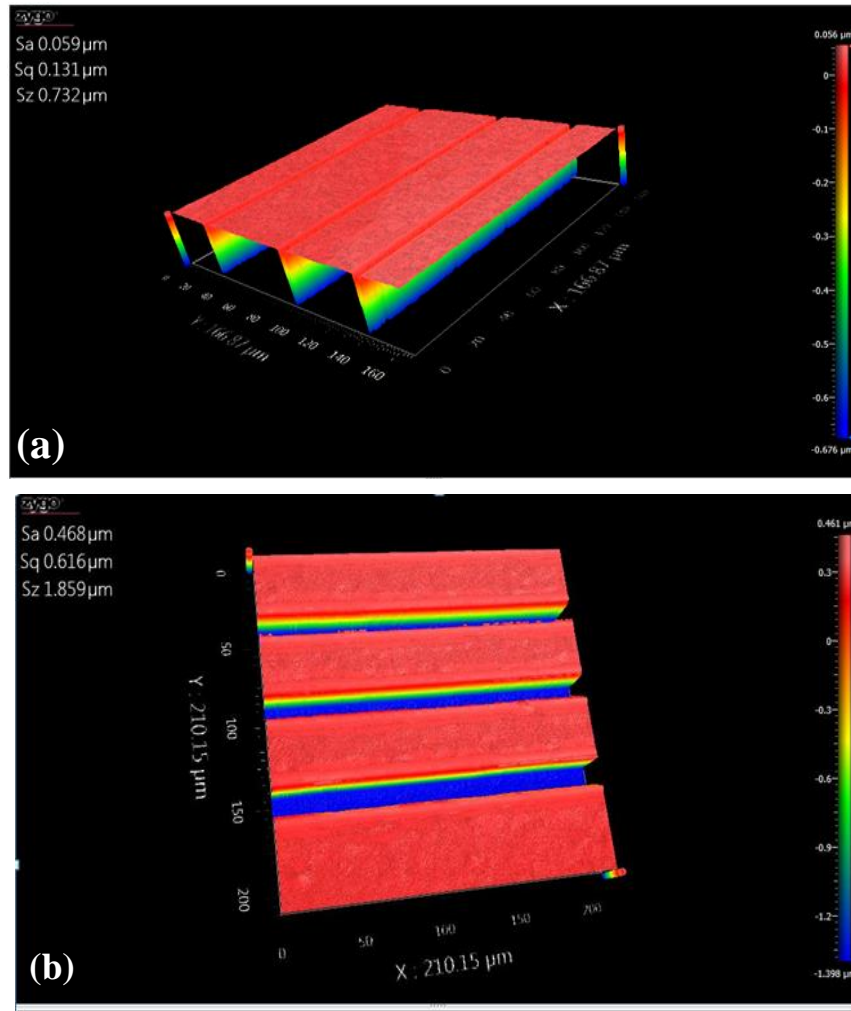


Figure 1-7 Microchannels fabricated by fs laser microfabrication in S1813 (Microchem[®], USA) with the fabrication speed in (b) are 7, 5, and 3 μm/s, respectively (from the top to the bottom line).

At the focus point on the surface of a photosensitive material, sufficient number of photons reach the surface at the same time so that two-photon absorption can occur. With the help of three-dimensional motion stages (introduced in Section 2.2.1), stereoscopic

structures can be easily and accurately fabricated by femtosecond laser, which will be discussed in Chapter 2.

1.3.2 Nonlinear photon absorption induced by fs laser

Femtosecond laser multi-photon polymerization is the main mechanism underlying the three-dimensional spatial microfabrication in this study. In 1997, Kawata *et al.* first proposed laser two-photon polymerization (TPP) as a direct writing technique for spatial structure microfabrication [80]. The basic conditions for achieving micro-fabrication of waveguide structures based on the principle of LTPP are: (a) simultaneous absorption, and (b) high power level. In order to realize an effective writing of waveguides, extremely high laser power is required. The latter is enabled by obtaining enough density of photons which is, in turn, required to create a significant number of two-photon absorption events [81]. Mode-locking femtosecond laser pulses can readily achieve extremely high power level at its focusing point [79]. This property has made it the most optimal candidate for inducing multi-photon simultaneous excitation from the valence band of ground state.

1.3.2.1 Multi-photon absorption

In general, nonlinear behavior occurs when the oscillation of a physical system is being overdriven by external fields. One example of an overdriven system is when the input intensity is significantly high. Specifically, this nonlinear process can be expressed by considering how the dipole moment per unit volume, or polarization $P(t)$, of an optical material evolves with the strength of the input field $E(t)$:

$$\begin{aligned}
 P(t) &= \varepsilon_0 [\chi^{(1)} E(t) + \chi^{(2)} E^2(t) + \chi^{(3)} E^3(t) + \dots] \\
 &= P^{(1)}(t) + P^{(2)}(t) + P^{(3)}(t) + \dots
 \end{aligned}
 \tag{1.15}$$

The higher order polarization $P^{(n)}(t)$ covers various nonlinear optical effects [82].

Figure 1-8 schematically illustrates how single photon absorption and multi-photon absorption take place in between energy levels.

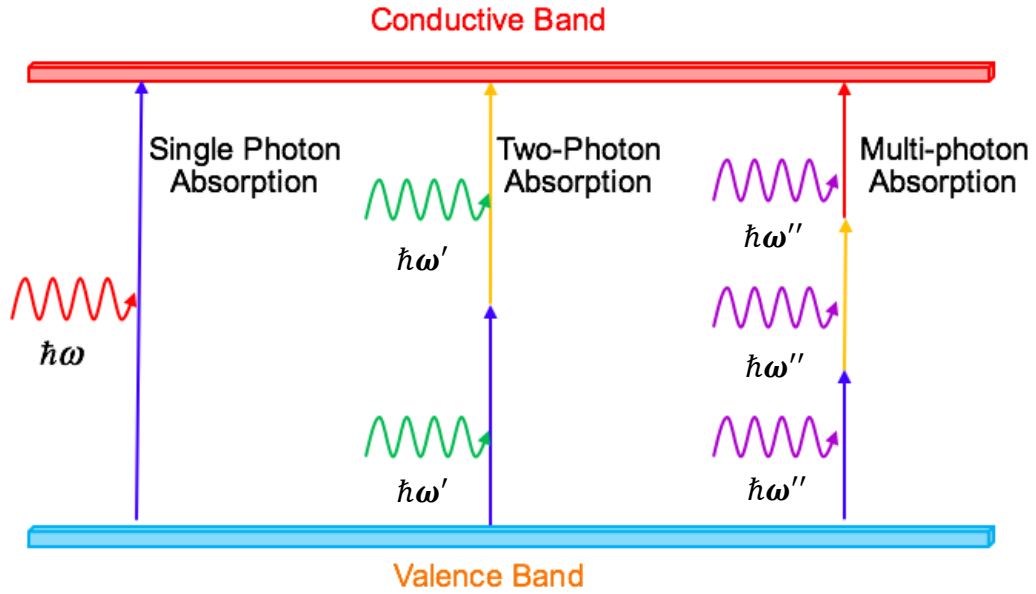


Figure 1-8 Schematic illustration of photon absorptions and transitions. $\hbar\omega$ is the photon energy, where ω is the optical frequency.

The oscillating wavelength between the valence band and conductive band is λ_1 .

In Fig. 1-8, for N -photon simultaneous absorption,

$$I_1 = N I_N \tag{1.16}$$

is always satisfied, where N represents the number of photons that are simultaneously excited. In other words, N -photon absorption is the process by which the energy gap between two real states is connected by the simultaneous excitation of n photons. However, unlike the ideal case discussed above, in reality, all the excited photons are not necessarily at the same frequency [83]. In all real transitions, the system energy is conserved, which means that

$$W = W_i + W_j + W_k, i, j, k = n \quad (1.17)$$

must be satisfied. Besides single photon absorption, the simplest variants would be two-photon absorption ($N = 2$) and three-photon absorption ($N = 3$), which are frequently utilized in laser microfabrication [86, 87] and microscopy [88–90]. In higher orders of photon nonlinear absorptions, none of the individual photons have sufficient energy to complete the transition from one energy state to another. For example, in two-photon absorption (TPA), both photons jump from ground state to an intermediate (virtual) energy state, where they constructively interfere to gain access to a higher-level eigenstate.

As stated above, neither of the two photons have enough energy to transit on their own as shown in Fig. 1-9. Let us assume that the system absorbed one photon and made a transition from the ground state $|g\rangle$ to an intermediate state $|a\rangle$. If the complete transition from the ground state to the nearest excited state could not be achieved within the ultra-short lifetime (10^{-15} s) of the virtual state, the ‘formed’ intermediate state would collapse back to the ground state.

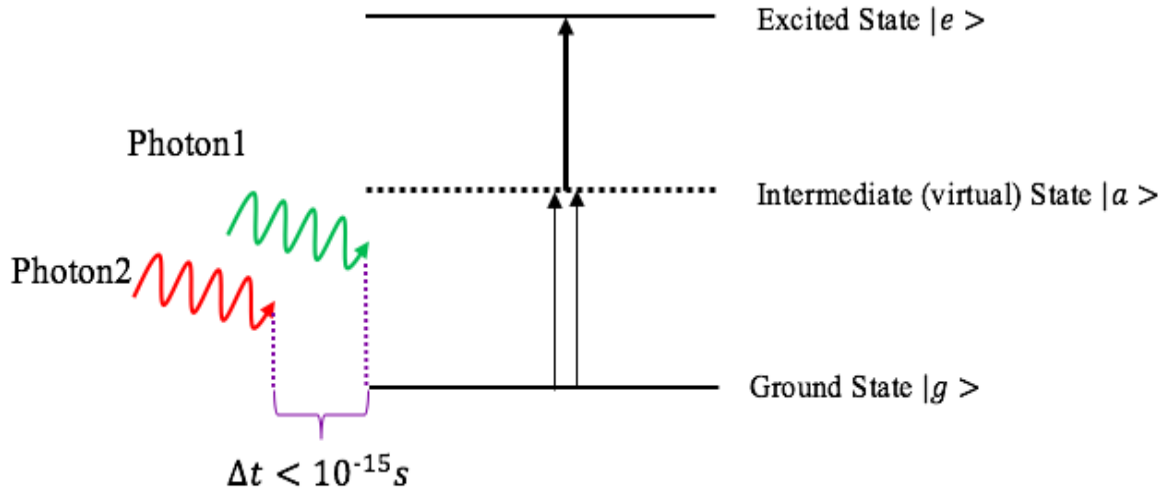


Figure 1-9 Schematic illustration of the nonlinear optical process caused by simultaneous absorption

To allow the first photon to jump to the nearest real electronic state, a second photon must be absorbed and complete the nonlinear interaction with the first photon within the virtual lifetime limit. In other words, the photon flux rate must be high enough to guarantee the presence of both photons before the virtual state collapses. This is such an essential condition for TPA to happen that experimental observation of TPA was not achieved until the invention of laser [89] and the related applications were not widespread until the commercialization of solid-state tunable ultrafast laser in the late 1990s [90].

Even though much higher power level is required for multi-photon absorption (MPA) to occur, significant interest in MPA remains among scientists and researchers of optical sciences because of MPA's distinct controllability [91] and flexibility [92]. Again, consider TPA as an example. Compared to its linear counterpart, multi-photon absorption

enables the infrared excitation light to suffer less scattering. The illumination only happens at the focal point [93]. This characteristic has made it possible for light to penetrate the interior of a material with much higher irradiation intensity. In addition, less scattering gives more accuracy, which makes MPA a very useful tool in any kind of laser-related microfabrication.

Consequently, multi-photon absorption is frequently involved in laser-related microfabrication with photo-sensitive materials [94]. While there is more than one method to induce optical damage, the most stable way to generate permanent damage of optical components is with laser beams. Specifically, lasers with ultrashort pulses (a duration within 10^{-15} s) generate significant pulse rates and extremely high optical intensities at the focal point. In such situation, a nonlinear process could happen at the focal point continuously.

1.3.2.2 Photolithography in photoresist materials

The photo-polymerizable optical material used in this study is NanoTMSU-8 Negative Tone Photoresist (Formulation 2, Microchem[®], USA). The number “8” comes from the fact that one single molecule of SU-8 contains an average of eight epoxy groups [95]. As a photoresist material, SU-8 is mixed with an epoxy derivative and a chemical photoinitiator with the amount equal to one tenth of the total weight of the SU-8 solution as is shown in Fig. 1-10 [96].

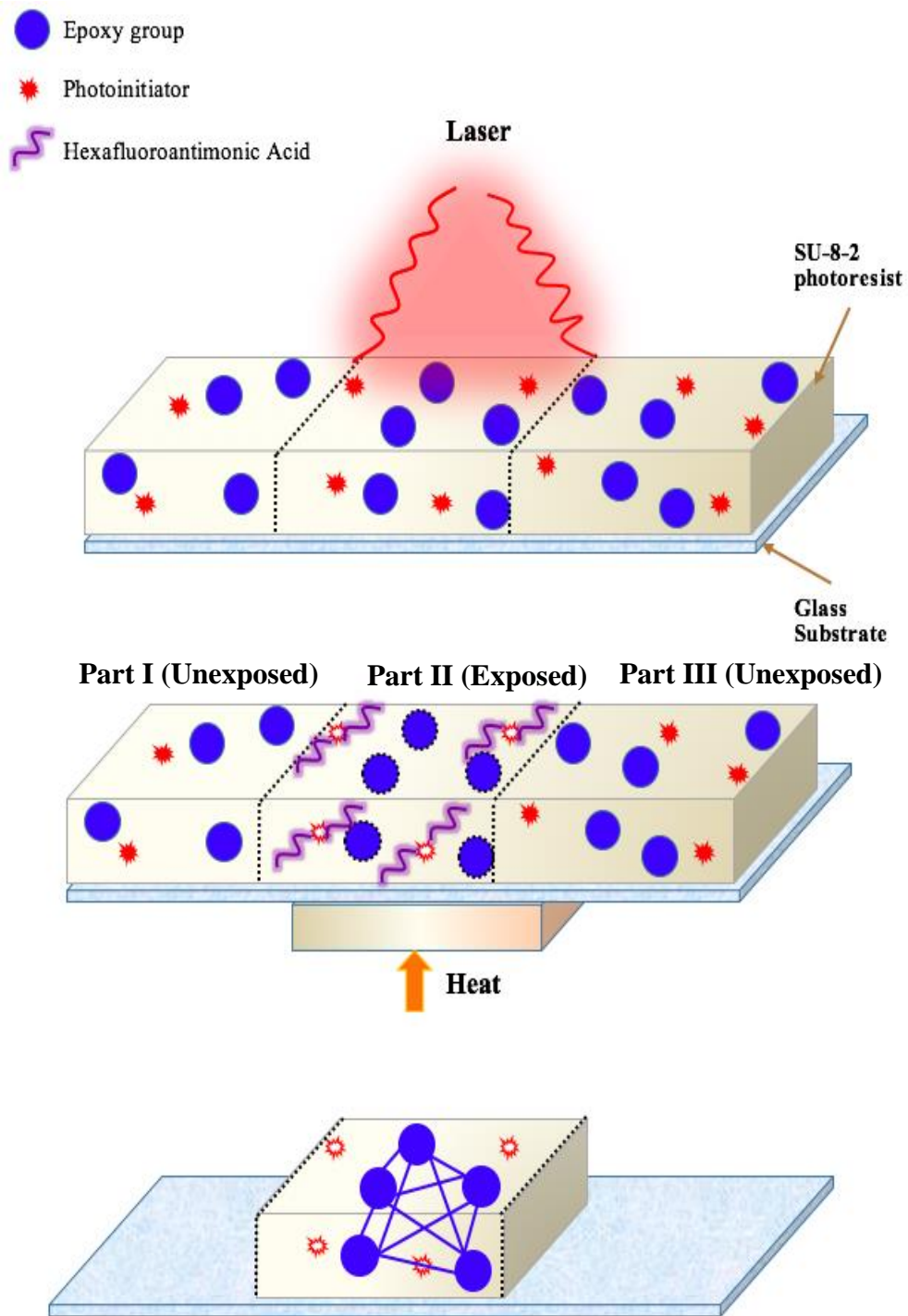


Figure 1-10 Schematic illustration of laser induced photochemical reaction process in photoresist materials

Figure 1-10 schematically describes the process of laser irradiation on commercial SU-8-2 photoresist material. The dots represent the grouped epoxy structures contained in SU-8-2 material. The irradiation of laser initiates the cross-linking process in SU-8-2. In Fig. 1-12, the area in between the two dashed lines is the laser-exposed area, where the photoinitiators absorb photon energy to decompose and release hexafluoro-antimonic acid inside the SU-8-2 photoresist layer. The acid works as a catalyst, opening up the eight benzene rings in the epoxy group (protonation) [97]. After baking the SU-8-2 chip on a hotplate, a cross-linking chemical reaction is activated among protonated and neutral epoxy rings, where the main chains or side chains of the epoxy polymer launches a random cross-linkage. Consequently, the exposed area of SU-8-2 has more cross-linking chains, strengthening its chemical force and making the exposed area much less soluble.

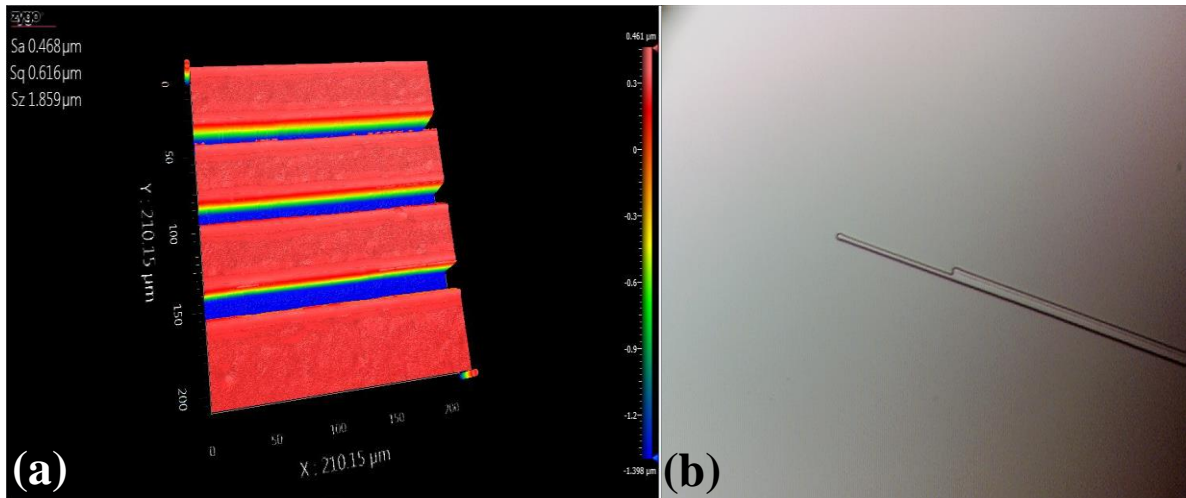


Figure 1-11 Experimental comparison between positive-tone and negative-tone photoresists (after the same laser irradiation and developing process): a) Image of positive-tone photoresist S1813 (MicroChem®, USA) taken with 3D optical surface profiler (Zygo®, USA). The gaps are the laser-exposed areas and are completely washed off. b) Image of negative-tone photoresist SU-8-2 under microscope (Leica, USA). The laser-exposed areas are precisely kept on the substrate while the rest are all washed off.

Photoresist materials like SU-8-2 are called negative tone photoresists [98]. The other type of photoresist material is called positive-tone photoresist. In the latter, the laser irradiation enables the photochemical reaction to rupture the existed linkages amongst monomers in the laser-exposed area [99]. The laser-irradiated area of positive photoresists produces weaker chemical bonding which makes it more soluble. As a result, the laser-exposed area of the positive photoresist film will be washed off during developing, while the unexposed areas (Part I and Part III in Fig. 1-10) will remain intact. The differences between a pair of negative and positive photoresist materials are experimentally shown in Fig. 1-11.

1.4 Wave-guiding Optofluidics

The above sections (1.1-1.3) provided a brief review of the newly emerging field of optofluidics and its applications in the realm of sensing analysis, followed by the background research applied in this study. In summary, micro-photonic components are being increasingly embedded into microfluidic systems to obtain highly integrated optofluidic-based devices. These micro-photonic components include waveguides, actuators, resonators, and optical gratings. Despite not reaching a stage of mass-scale production yet, multiple integrated multi-functional on-chip optofluidic devices have been developed within the past few decades [100], increasingly becoming cost-effective, environmentally sustainable [101], and highly adaptable.

Lithography was the main fabrication method for optofluidic devices in the early days of optofluidics. The substrates used for this technique are usually glass and silicon

[102]. However, demand for expensive substrate materials and cleanroom requirements have restricted the growth and application of lithography-based research into large-scale analysis. In the following years, several new techniques have been applied to fabricate optofluidic devices, such as hot embossing [103], micro-injection molding [104], and UV laser ablation [35], in order to strengthen the device functionalities while reducing fabrication costs.

It was not until the Whiteside Research Group developed the technique of soft lithography that microfluidic and optofluidic research started booming exponentially [105]. Soft lithography introduced polymer materials in the field of microfluidics, for the first time, as a cost-effective substitution of silicon substrate. The commonly used polymer materials include polydimethylsiloxane (PDMS), polymethyl-methacrylate (PMMA), polycarbonate (PC) and polystyrene (PS). PDMS [106] is the most employed material in microfluidic and optofluidic devices. It has the advantage of solving the shortcoming of lithography by being cost-effective, time-saving, easy to peel off, and by not requiring cleanroom facilities. In this study, we use soft lithography of PDMS to fabricate the microchannel chamber to achieve rapid prototyping, simplicity, and robustness in our optofluidic devices.

For large-scale microfabrication of the waveguide structures in optofluidic devices, silicon is the most widely used material. However, engraving deep trenches in silicon wafer takes a relatively long time: the common methods for fabricating silicon are, approximately, 0.5 $\mu\text{m}/\text{min}$ for dry etching, and 1.4 $\mu\text{m}/\text{min}$ for wet etching [107]. Other limitations of silicon are its high commercial price and its low optical transmittance in the visible wavelength regime [108]. Other than silicon, borosilicate glass is broadly used as

optical material [109]. It is fully transparent in the visible wavelength range, which is an important quality in optical applications. An effective way of fabricating borosilicate glass for microchip devices is chemical etching using Hydrofluoric Acid (HF) [110]. However, it is of great danger for the person who operates HF as it is highly corrosive and toxic. Thus, a lab with special safety equipment is required prior to conducting experiments with HF. This significantly decreases its possibility as an active element in optofluidic research. Compared to the aforementioned materials, SU-8 series (MicroChem[®], USA) is the most suitable and safe material as the waveguide element in an optofluidic integrated system. It has a relatively short fabrication time – this study used a scan speed of 5 $\mu\text{m/s}$ for exposing SU-8-2 negative photoresist thin film – reasonable price, and full transparency in the visible wavelength range [111]. Furthermore, SU-8 is adhesive to both silicon and glass, which allows glass to substitute silicon to be the substrate of waveguides.

The UV light sources can also be fabrication tools for SU-8 photoresist [28]. However, not all the UV light sources are ideal candidates for optofluidic waveguide microfabrication. For instance, for long-pulse UV lasers, the heat-affected zone around the exposed area is not negligible, therefore high accuracy and structure smoothness cannot be achieved. For the past decade, a new fabrication technique has been developed based on the nonlinear optical effect that occurs when photosensitive transparent materials are exposed to ultrashort photon pulses. This technique is often referred to in the literature as femtosecond laser microfabrication and is widely used in the fabrication of photonic components [112].

Over the last few years, direct writing with fs laser has been applied to the fabrication of optofluidic devices, such as waveguides and microchannels [115–122]. Ring resonators and racetrack resonators are two examples of waveguides structures microfabricated with fs laser and used to sense changes in the environment [23]. Both the waveguides and the microchannels can be shaped accurately and tapered in different ways to serve different purposes. Tapered microchannels can be used for cell sorting and counting in liquid media, with many practical uses, such as red blood cell counting [123–125]. Furthermore, integration of waveguides in an optofluidic microchannel system with fs laser has high potential in biological, chemical, and medical sensing and analysis [42, 126, 127]. The refractive index of the waveguide material should be higher than that of the surrounding fluid environment, which allows light to be transmitted along the waveguide structure. Polymers with RI lower than water can be coated on the inside of the microchannel to keep light going through the waveguide alone [125]. Reconfigurable photonic fiber is another vital application of femtosecond laser microfabrication. Due to the nonlinear effect induced by fs laser, various types of nonlinear materials in different phases can be injected into the PCF resulting in numerous optical applications[128–136].

However, as the most important quality of an optofluidic sensing device, the mechanism behind changes in sensitivity is not thoroughly studied. In this study, the principle of optical nonlinear effect is utilized to the fabrication of a compact optofluidic waveguide sensing system to achieve precise and controllable sensing. This greatly increases the reconfigurability of optofluidic devices. This thesis presents a novel, integrated optofluidic waveguide micro-photonic system. It incorporates the power of femtosecond-laser-induced multiphoton absorption and the capability of microfluidic

systems to realize tunable and reconfigurable sensing. The micro-photonic system contains a waveguide whose sensing window has the shape of a spiral and a PDMS-based microchannel. The optofluidic waveguide sensing system was designed and fabricated for the very first time in the field of optofluidics and holds the promise of robustness, controllability and adjustable sensitivity with high tunability. Its fabrication and use will be elaborated in the following chapters.

1.5 Optofluidics for bio-sensing applications

Optofluidic devices have been widely used in bio-sensing applications [135-138]. Especially, optofluidic sensing system is well-suited for the analysis of biological materials of very small volume. Before the emergence of optofluidics, fluorescence labeling was widely used to detect biomolecules, such as red blood cells, antibody, or protein [139-141]. However, it could cause potential modification to the analytes when applying fluorescence labeling [142]. Optofluidic sensors provide the option of label-free bio-sensing, which the particles can be detected by monitoring the changes in the transmission spectra. Also optofluidic sensors combine more merits from the integration of both optics and microfluidics, which includes small volume of reagent required, high portability, and high reusability [143-146]. On account of the advantages of sensing with optofluidic devices, biomaterials have been investigated with optofluidic sensors since nearly one decade ago. Li *et al.* fabricated an optofluidic ring resonator biosensor, and the detection of biotin molecules was carried out to investigate its sensing performance [143, 147]. Gutierrez *et al.* designed an integrated optofluidic system to study how the variety

of grapes can influence the quality of red wine [148]. Optofluidic devices have been utilized in human biology as well, to study microstructures in human bodies such as DNA [149-151].

Long regarded as a nutritious drink, cow milk and milk-like products related studies have attracted considerable attention of researchers. However, most research focused on their biological, medical, and chemical aspects to understand the compositions of milk and milk-like products, and their interactions with human body [153-155]. The optical properties of milk and milk-like products demand further investigation to help humans to understand their composition. While milk has already been considered as an important source of nutrients, nowadays milk-like products such as almond and coconut milk have emerged in grocery stores in order to meet various diet needs for different individuals. In this study, the optical properties of cow milk, lactose free milk, organic milk, almond milk, coconut milk, and evaporated milk are investigated with the spiral optofluidic waveguide sensor to study how the pre- and post-milking processes, and milk aging influence the optical properties of cow milk and milk-like products.

1.6 Thesis objectives

The objective of this thesis is to use the optical nonlinearity induced by femtosecond laser to fabricate waveguide structures in photoresist material and to explore the possibility to apply waveguide-integrated optofluidic systems for sensing multiple environmental parameters. More specifically, this research focuses on:

1. Waveguide microfabrication in photosensitive materials using the multi-photon absorption induced by femtosecond laser
2. Investigation of various physical and chemical properties of fluidic samples through the use of the optofluidic sensing system (spiral-shaped optofluidic waveguide sensors) fabricated with fs laser
3. The application of an optofluidic sensor system on biomaterials

Chapter 2 Spiral Optofluidic Waveguide Sensors

This chapter consists of two parts. The first part demonstrates the microfabrication of spiral optofluidic sensors, including the fabrication of waveguides using femtosecond laser and the fabrication of microchannels with soft lithography. The second part of this chapter describes the sensing of temperature change, refractive indices of liquids, and change of positive pressure of several types of liquids via the use of spiral optofluidic sensor. Sensitivities for the physical properties under investigation are compared at the end of the chapter.

2.1 Waveguide fabrication processes

The NanoTM SU-8-2 (MicroChem[®], USA) negative tone photoresist series (abbreviated as SU-8-2) is used as the core material for the waveguides. SU-8-2 is a suitable candidate for the core material of an optofluidic waveguiding device given its advantages. Firstly, SU-8-2 is a negative photoresist, for which the area exposed by light irradiation will remain intact while the rest of the film will be washed off during developing stage. Secondly, SU-8-2 possesses a high index of refraction and excellent thermal and chemical resistance. Thirdly, the absorbance peak of SU-8-2 is in the near UV range (350~400 nm) [156], allowing two-photon absorption to occur when exposed to fs laser (wavelength of 800

nm). Figure 2-1 indicates the difference in refractive index of four common commercial negative photoresists.

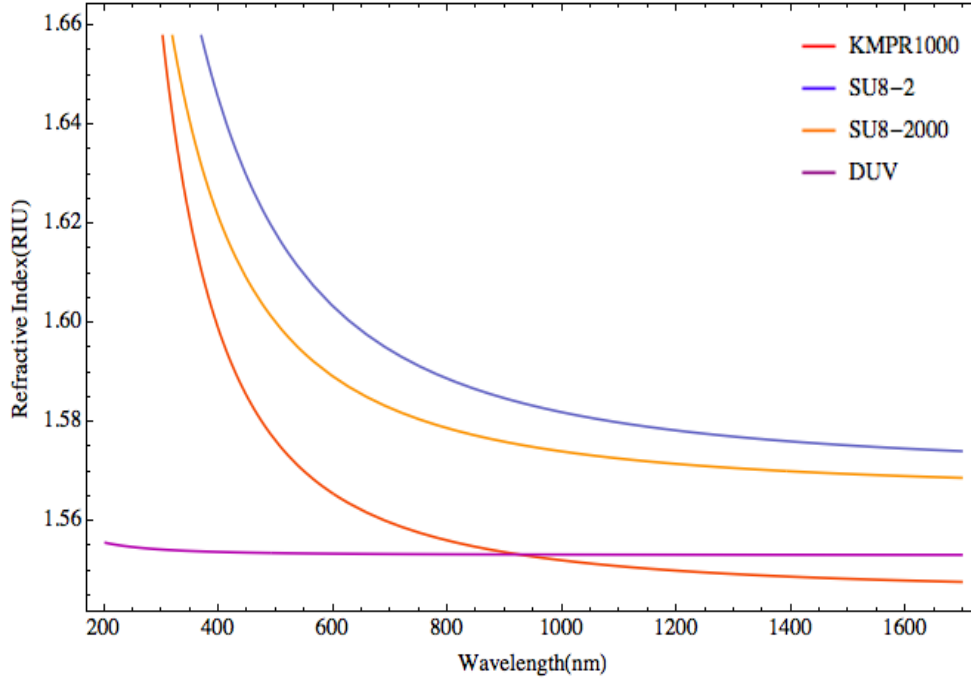


Figure 2-1 Comparison on the refractive index of four common negative photoresists: SU-8-2 negative photoresist (MicroChem®, USA), SU-8-2000 series negative photoresist (MicroChem®, USA), KMPR 1000 chemically amplified negative photoresist (MicroChem®, USA), and UVN® 30 DUV negative photoresist (SHIPLEY®, USA). The Cauchy coefficients of the four most common negative photoresists were obtained from their suppliers [145–148].

2.1.1. General procedures for processing SU-8-2

Figure 2-2 shows the general procedure for processing SU-8 series and the relevant instruments used in each step. These procedures follow the suggestions from the datasheet provided by MicroChem® [159]. With these suggested procedures, microstructures of various sizes and shapes have been fabricated in SU-8-2 [49, 142].

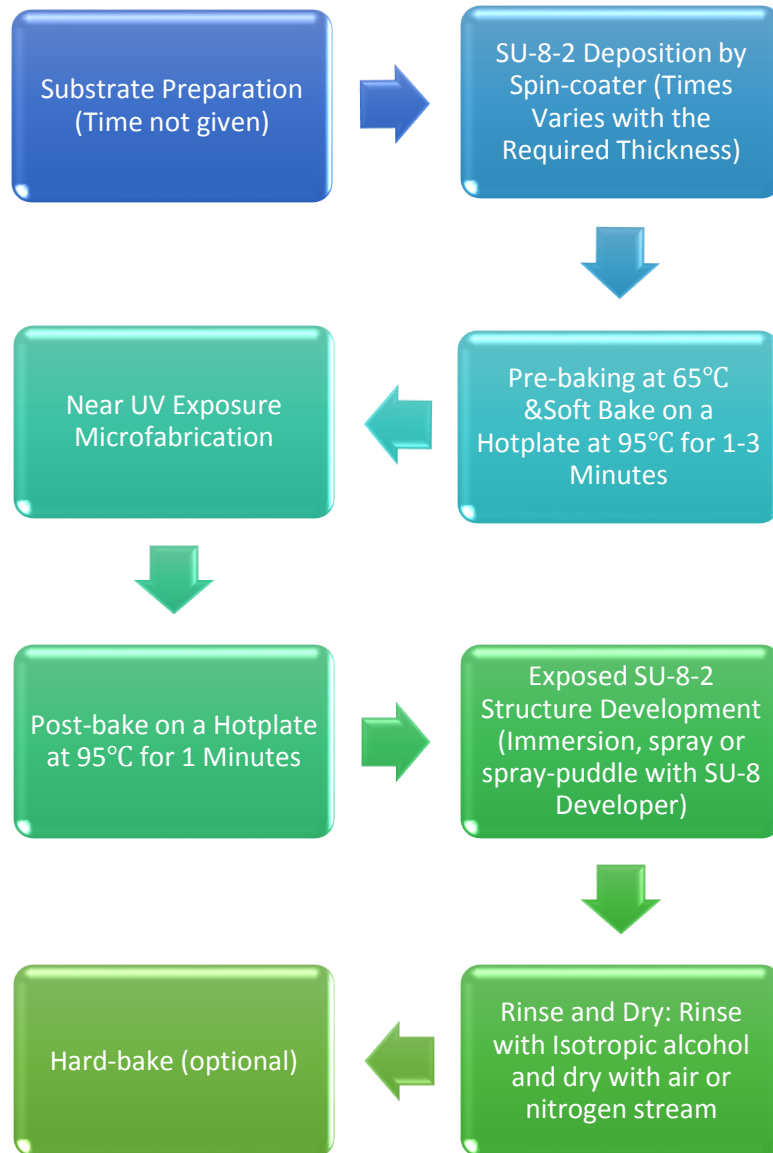


Figure 2-2 Typical procedures for processing SU-8-2

The first step of SU-8-2 lithography is to thoroughly clean the glass substrate. The substrate treatment is necessary as the adhesion strength between glass and SU-8-2 is relatively weak. As the core material of an optofluidic device, SU-8-2 waveguide needs to be tightly attached to the glass substrate to prevent the waveguide from lifting off from the substrate by the injecting liquid flow. SU-8-2 is then deposited on the glass substrate followed by a post-baking at 65 °C and a soft-baking at 95 °C for 1 to 3 minutes. After exposure to a light source, the SU-8-2 thin film is placed on a hotplate for post-baking before being developed in developer. Next, the developed SU-8-2 thin film is rinsed with isotropic alcohol and dried with either air or nitrogen stream. The last step is to hard-bake the SU-8-2 film on a hot plate to harden its structure.

2.1.2 Improved procedures for processing SU-8-2 waveguide

The parameters adopted in the fabrication of SU-8-2 in this study differ from the typical procedures illustrated in Fig. 2-2 owing to the variation of experimental conditions and the equipment specifications. The modified procedures for the fabrication of the spiral optofluidic waveguide sensors in this study are described in detail as follows.

The substrates used for SU-8-2 microfabrication are standard microscopic glass slides (76 × 26 mm). Before coating SU-8-2 onto the glass substrate, the glass is cleaned for optimal coating and to prevent the edges of the film from detaching during sensing experiments. The glass substrate is then fully immersed into a beaker filled with acetone and placed in the ultra-sonicator (Branson[®] 8510, USA) for 10 minutes to remove dust particles from the surface. Subsequently, the substrate is bathed in ethanol and placed in

the ultra-sonicator for 5 minutes to remove acetone residue. Next, the substrate is laid in a beaker filled with distilled water and treated in the sonicator for 15 minutes for rinsing. Finally, the fully-cleaned glass substrates are quickly blow-dried by compressed air stream and then placed into the oven (Thermolyne[®] 1400, USA) at 200°C overnight.

After baking the glass substrate in the oven, SU-8-2 solution is poured onto the substrate. The substrate carrying SU-8-2 is carefully placed onto the spin head of a spin coater previously leveled (Headway Research Inc., USA) and is then spin-coated at 800 ± 5 rpm for 40 s. The spin coater is pre-leveled every time before carrying out spin coating to ensure even thickness throughout the entire SU-8-2 film on the glass substrate. Subsequently, the spin-coated SU-8-2 substrate is removed from the spin coater to a hot plate (Sigma Systems, USA), pre-baked at 65°C for 1 minute. This is followed by baking at 95°C for 5 minutes or more to ensure that the waveguide structure is sturdy enough when fluid flows into the microchannel.

The SU-8-2 film is exposed to femtosecond laser to create the desired waveguide pattern on the film. A more detailed explanation of this procedure is provided in Section 2.2. The exposed SU-8-2 substrate is then transferred back onto the hot plate for post-baking. The temperature of post-baking is increased gradually from 65°C to 95°C for 2 minutes. The post-baking ensures that the exposed area of SU-8-2 film is fully cross-linked and is completely resistant to the developer. The post-baked substrate is cooled down before developing to prevent thermal shock. Finally, the SU-8-2 is immersed into the SU-8-2 developer (MicroChem[®], USA) for 1 to 3 minutes. The sample is gently spun in the developer to thoroughly develop the unexposed area of the SU-8-2 thin film. Once

developed, the SU-8-2 sample is laid on the spin coater and ethanol is sprayed on its surface before spinning to clean the residue of the developer. The spin speed applied in this step is 2700 rpm or higher. To harden the fabricated structure, the SU-8-2 sample is hard-baked for at least 2 minutes.

2.2 Waveguide microfabrication with femtosecond laser

2.2.1 Exposure conditions

In this study, a near-IR, mode-locking femtosecond Titanium-sapphire (Ti:sapphire) laser (Coherent[®], USA) is used as the light source. Its oscillating wavelength, pulse width, and repetition frequency are 800 nm, ~100 fs, and 80 MHz, respectively. When the fs laser is focused onto a photo-polymerizable photoresist material at the focal point, there is a sufficient cluster of photons to generate a significant amount of multi-photon excitations [162]. TPP with fs laser enables accurate and controllable laser damage of the photoresist materials, or optical materials in general [163]. Therefore, exposure of photoresist materials by laser irradiation is a highly effective way to fabricate complicated structures onto the surface or inside exposed material.

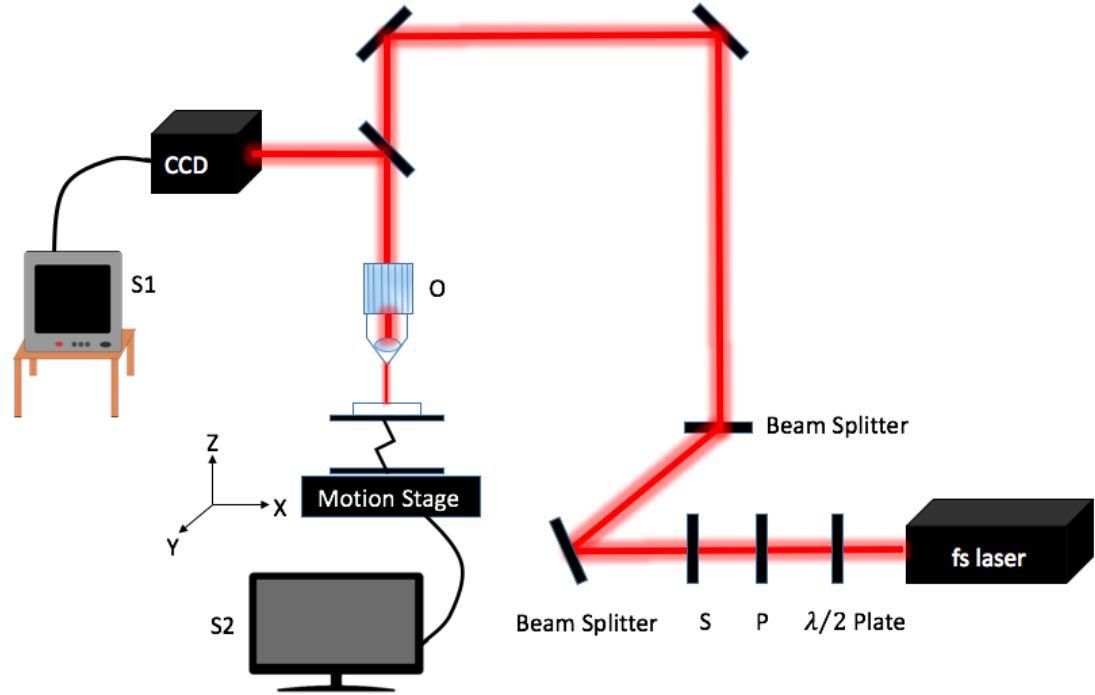


Figure 2-3 Experimental setup of fs laser microfabrication in this study. S is a shutter; P is the polarizer; S1 is the monitor which is connected to the CCD camera (Panasonic KR222, Japan); S2 is the computer that is connected to the motion stage; O is an objective lens (Leica, USA)

Figure 2-3 describes the components and optical path of the femtosecond laser microfabrication system in this study. The laser intensity guided into objective lens *O* can be adjusted by placing a $\lambda/2$ plate and a polarizer in front of the laser output. Laser irradiation onto the photoresist SU-8-2 (introduced below) results in a change in the photoresist's chemical structure. The exposure time of laser determines the size of the structure-modified area of the photoresist sample.

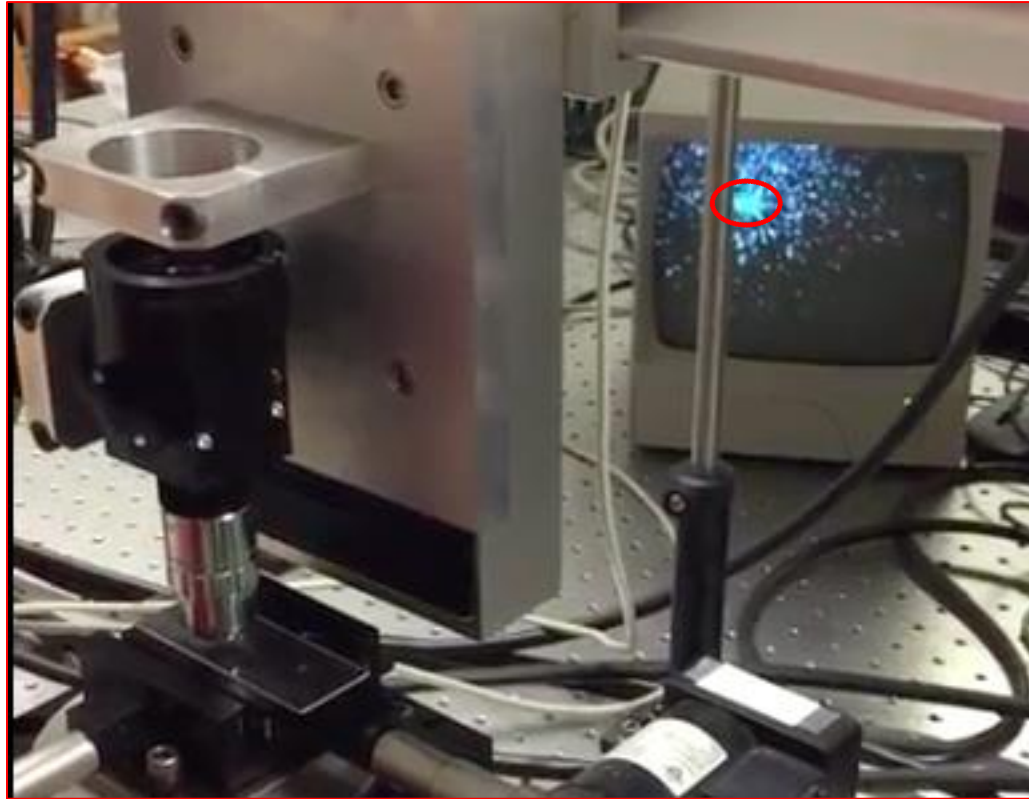


Figure 2-4 A photo of the focusing process with the help of the objective lens-CCD Camera display system

In this setup (Fig. 2-3), exposure time is accurately controlled by a mechanical shutter placed next to the polarizer. A 50 \times objective lens is set above the sample platform and assisted by a reflection image system (CCD camera with a display screen) to achieve its focusing purpose. The sample platform is placed onto a positioning system. The positioning system consists of a three-way motion stage (Newport, USA) of which the precision is 0.5 mm. The motion stage can be precisely repositioned with programming in X, Y, and Z directions and is connected to a computer for real-time monitoring during the waveguide fabrication process.

The waveguides of the spiral optofluidic sensors are fabricated with femtosecond laser direct inscription. The laser beam must be accurately focused onto the surface of the SU-8-2 film for it to have sufficient exposure to the fs laser. If the laser focus point is on the top surface of the SU-8-2 film, simultaneous absorption of two photons may not occur and the film will not be cross-linked. As there is no cross-linkage to strengthen the chemical bonding of the SU-8-2 film, the entire film will be washed off after developing. On the other hand, if the laser is focused around the bottom area, the SU-8-2 thin film may be burnt due to excessive exposure to laser energy, as shown in Fig. 2-5(b).

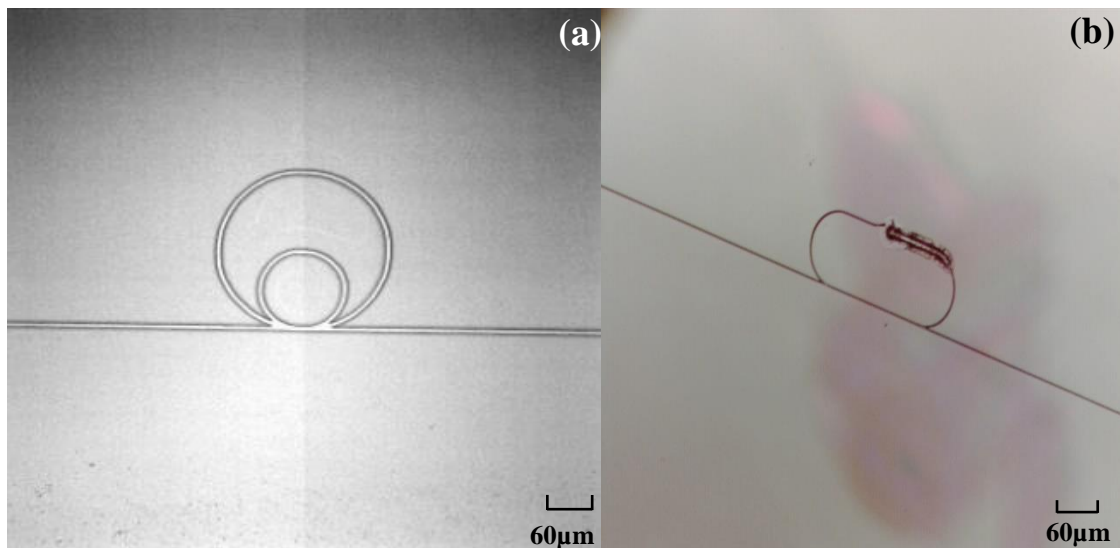


Figure 2-5 Effect of fs laser focusing conditions during SU-8-2 fabrication: (a) An SU-8-2 waveguide fabricated by fs laser focused onto its surface, (b) an SU-8-2 waveguide with a burnt area when the laser is focused on the bottom of the SU-8-2 film.

Apart from the appropriate point of focus, the successful fabrication of waveguides with femtosecond laser also depends on the duration of laser exposure as shown in Figure 2-6(a), and the speed of scanning of the sample film which is illustrated in Fig. 2-6(b).

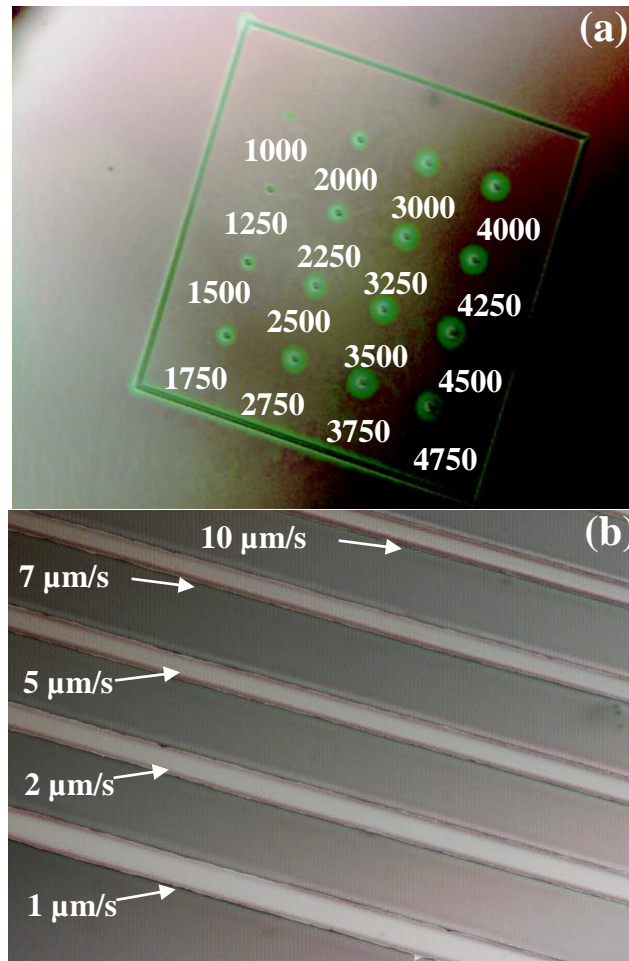


Figure 2-6 Effect of the duration of fs laser exposure on SU-8-2 thin film on the area of cross linkage, fs laser is focused with a 50× objective lens: (a) exposure duration is in the unit of millisecond (ms). The longest exposure duration is 4750 ms (bottom right dot), and the shortest exposure duration is 1000 ms (top left dot), and (b) Effect of the scan speed of the fs laser, the scan speeds are 10, 7, 5, 2, 1 $\mu\text{m/s}$.

2.2.2 Waveguide design

Spiral waveguides are designed based on the Mach-Zehnder Interferometer (MZI) [164], consisting of an input waveguide, an output waveguide, and a sensing area, which includes a beam splitter, a bus waveguide, a spiral-shaped waveguide, and a beam combiner, as shown in Fig. 2-7.

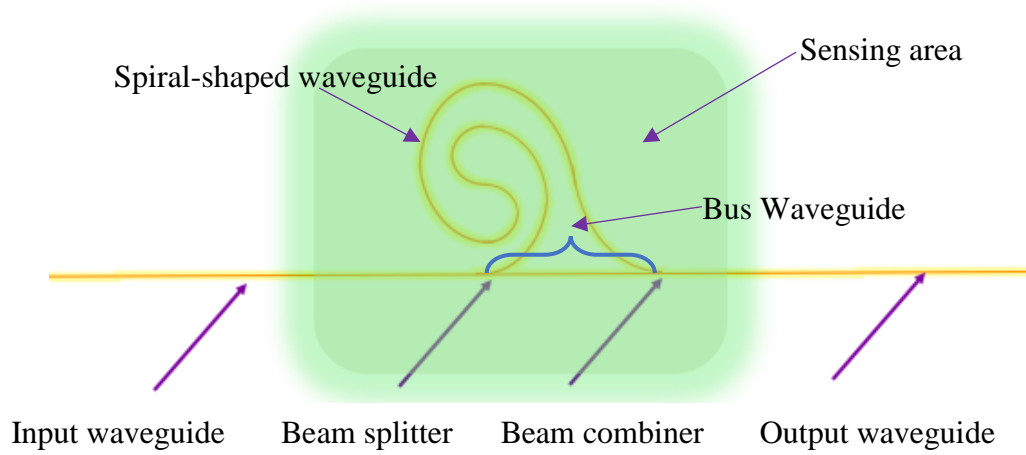


Figure 2-7 Design of the spiral waveguide with the sensing window shown in the rectangular shadow

For homogeneous sensing, the linear sensitivity of the MZI-based waveguide sensor can be expressed as [165]:

$$S = \frac{\sum_0^n I_n}{\Delta x} = \frac{\Delta I}{\Delta x} \quad (2.1)$$

where ΔI represents the shift of the interference patterns of the normalized output light and Δx represents the change of the physical properties (e.g. refractive index,

temperature, pressure, or concentration). In the sensing area, a phase shift $\Delta\varphi$ occurs, which is due to the change of the effective refractive index in the guiding mode of the propagation light around the sensing area. The phase shift can be expressed as:

$$Dj = \frac{2\rho}{l} Dn_{eff} D \quad (2.2)$$

where n_{eff} is the effective refractive index, D is the length of the optical path difference, and λ is the wavelength of the incident light. Equation 2.3 provides the relation between the sensitivity of the spiral waveguide sensors S and the optical path difference as [153]:

$$S = \frac{2\rho}{l} \cdot \frac{DI}{Dj} \cdot \frac{Dn_{eff}}{Dx} \cdot D \quad (2.3)$$

where $(\Delta I/\Delta\varphi)$ is the partial sensitivity of the interference, and $(\Delta n_{eff}/\Delta x)$ is the partial sensitivity of the change of the effective refractive index due to changes in physical properties and the surrounding environment. Equation 2.3 indicates that the sensitivity of the MZI-based spiral waveguide sensors is related to the change of length of the sensing window.

Based on the sensing theory described above, four SU-8-2 waveguides with spirals of different numbers of spiral curves are designed and fabricated. Each sample contains one spiral-shaped waveguide and one bus waveguide. Figure 2-8 shows the shapes of the spiral waveguides with the total lengths of the spiral curves of 376.99, 1096.73, 2261.95 and 3769.91 μm , respectively. The shape of a spiral enables the possibility to adjust the optical path difference between the spiral waveguide and the bus waveguide, while avoiding unnecessary transmission loss of the propagating light caused by sharp turns.

The smallest radii of the four waveguides are all equal to $30.0\ \mu\text{m}$. The value of the smallest radius is chosen based on two criteria: one is to make sure the entire waveguide is able to be fitted the microchannel (width around 1mm); the other is the accuracy of the motion stage used in this study, which is $0.5\ \mu\text{m}$. Consequently, the smallest circle or half circle with consistent and smooth curves that can be achieved are the ones with radii of $30.0\ \mu\text{m}$.

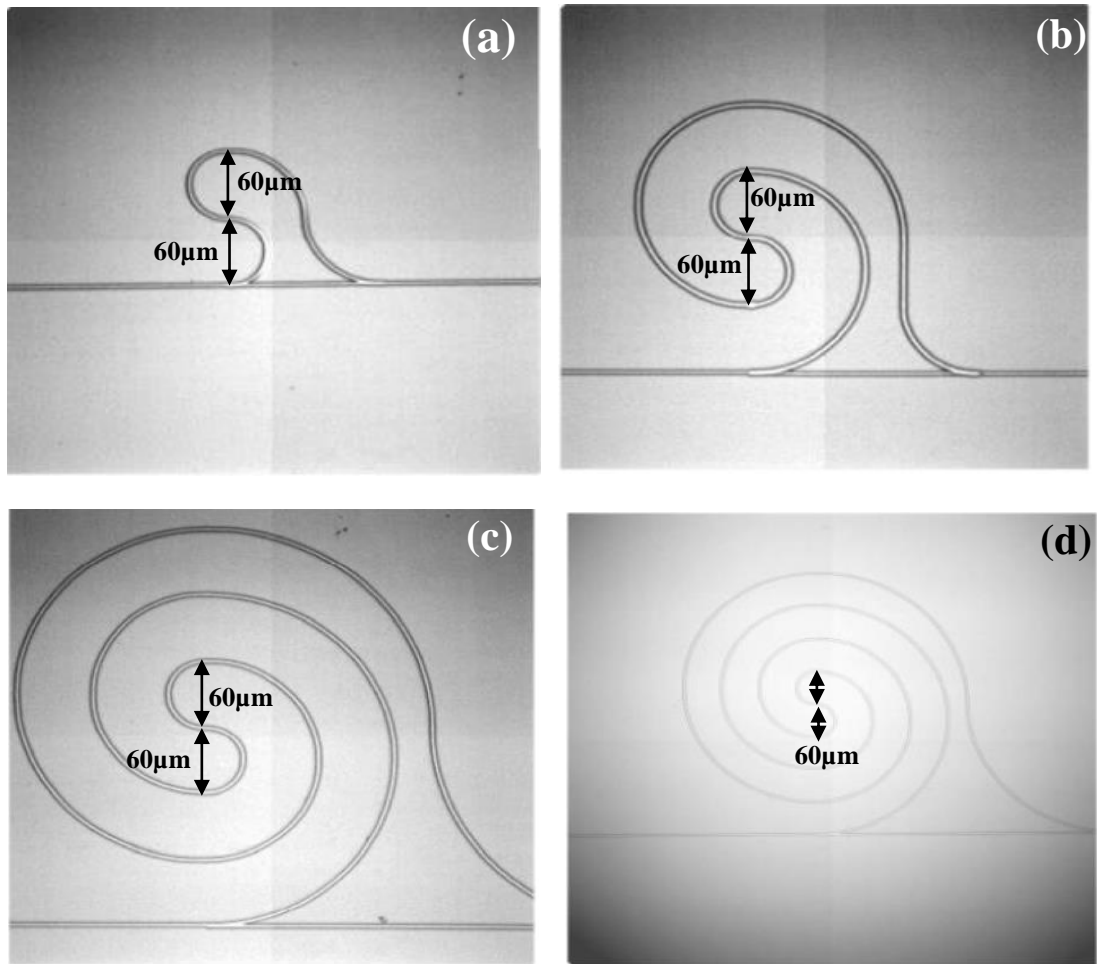


Figure 2-8 Microscopic images of the four spiral waveguides with the total lengths of the spiral curves of (a) 376.99 ; (b) 1096.73 ; (c) 2261.95 ; and (d) $3769.91\ \mu\text{m}$, respectively.

For simplification, the waveguide which contains one spiral with a total spiral length of 376.99 μm will be referred as single-spiral waveguide. Similarly, double-spiral waveguide, triple-spiral waveguide and quadruple-spiral waveguide will stand for the waveguides with spiral lengths of 1096.73, 2261.95, and 3769.91 μm , respectively.

2.3 Fabrication of the microchannels

The microfluidic channel is the cladding of the entire optofluidic waveguide sensor structure. For the cladding material, polydimethylsiloxane (PDMS) is a suitable candidate [154]. PDMS has a refractive index of 1.40 over the range 240 nm – 1100 nm [154], which is much lower than that of SU-8-2, the waveguide material used in this study.

PDMS can be attached to the glass substrate covalently by treating the polymer with Plasma Cleaner (PDC-001, Harrick Plasma[®], USA) to form a leak-free fluidic connection. The master (pattern of the microchannel) is fabricated by exposing the SU-8-2075 thin film to a white light source. SU-8-2075 has a much higher viscosity than most SU-8 series products, thus can form a much thicker film on the substrate with the help of a spin coater. The PDMS polymer and the curing agent (Dow Corning Sylgard-184, USA) are mixed with a ratio of 10:1 and stirred until they are thoroughly mixed to form the material of the microchannels. The fabrication process of PDMS is described in Fig. 2-9. The amount of PDMS in which the microchannel is formed has a mass of 4.5 g. After mixing, the PDMS channel is then degassed in a vacuum desiccator for 30 minutes and baked for at least half an hour. Subsequently, the microchannel is carefully peeled off from the master. The microchannel is then punched on two ends with a 22-gauge needle

(Inner Diameter 0.413 mm, Outer Diameter 0.718 mm) to create two holes where the fluid can pass through.

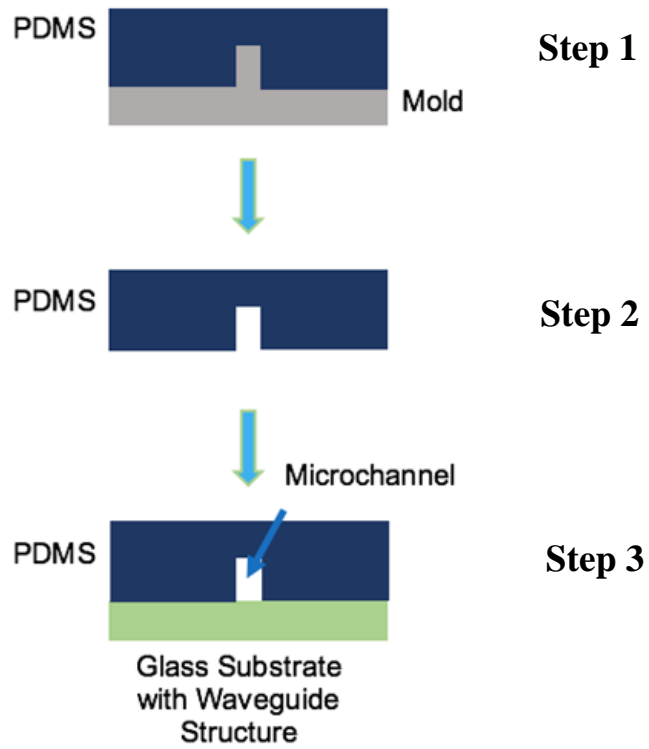


Figure 2-9 Soft lithography process to fabricate PDMS microchannel

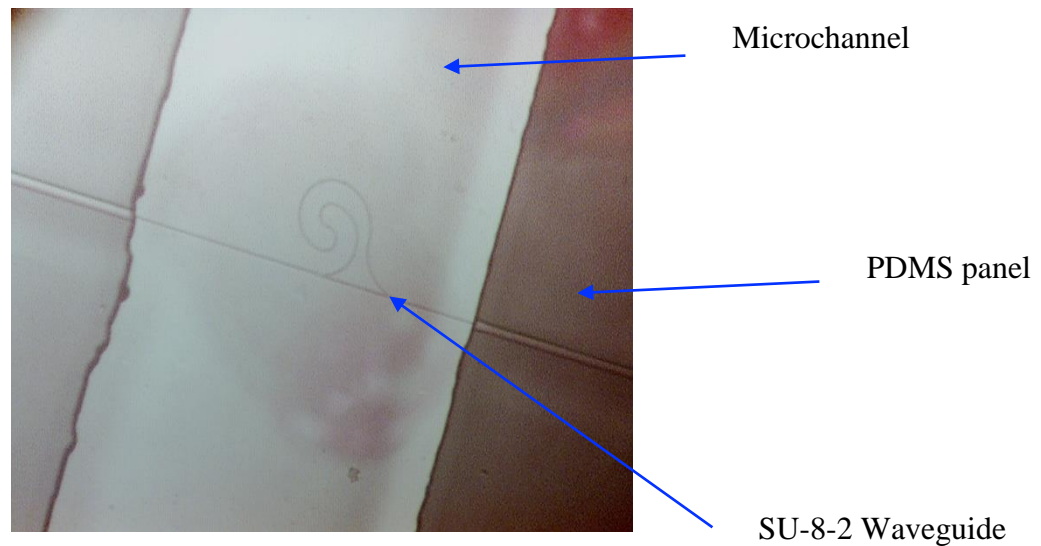


Figure 2-10 Waveguide-microchannel optofluidic system

As a final step on the microchannel preparation, thorough cleaning is needed before attaching the PDMS microchannel onto the glass substrate. First, a tape is quickly applied on and off (at least three times) on both sides of the microchannel. Second, a covalent bonding between the glass substrate and the PDMS microchannel panel is created on the surface with plasma treatment. The purpose of plasma treatment is to oxidize the surface of PDMS so that an irreversible bonding can occur between glass substrates and oxidized PDMS. Both the glass substrate and the PDMS mold are placed in the chamber of the plasma cleaner (PDC-001, Harrick Plasma, USA) and are then treated at high radio frequency (8 – 12 GHz) for 30-40 s (including the short time period the plasma cleaner needs to increase from low to high radio frequency). After the plasma treatment, the glass substrate and PDMS microchannel are removed from the chamber and then quickly attached together with sufficient force to achieve a Si-OH bonding on

the surface, which is irreversible. Figure 2-10 illustrates an example of the bonded optofluidic waveguide-microchannel structure. The bonded optofluidic chip is then placed on a hotplate for an hour or more to strengthen the bonding.

2.4 Experimental setup

After sufficient hard-baking, the bonding of the optofluidic sensor chip has become tight and irreversible. Then the sensor chip is placed onto an optical adjustment stand (Thorlabs, USA) that enables 3D and inclination adjustments.

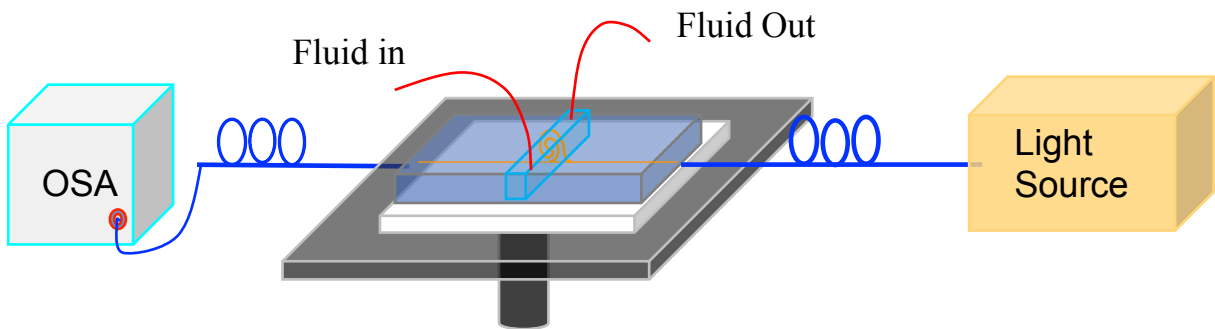


Figure 2-11 Experimental setup for sensing with the spiral waveguide sensor

A broadband light source (MPB Technologies Inc., Canada) is connected to a single-mode fiber (SMF) (Corning SMF28e) from one side of the sensor chip. Through proper adjustment of the location parameters of the optical stand, the SMF is able to couple the light beam into the SU-8-2 waveguide. The experimental setup for this is shown in Fig. 2-11.

The entire experimental set up is adjusted to minimize the power loss of the light beam during coupling. The coupling process is assisted by a CCD camera (Panasonic GP-KR222 color digital camera, Japan) and a Hamamatsu camera system (Japan), which includes a camera head C2741-03 and controller C2471 to receive the coupled light from the output side of the waveguide. The Hamamatsu camera head is then replaced by a power meter (2832-C, USA) to measure the actual value of the coupled light from the output.

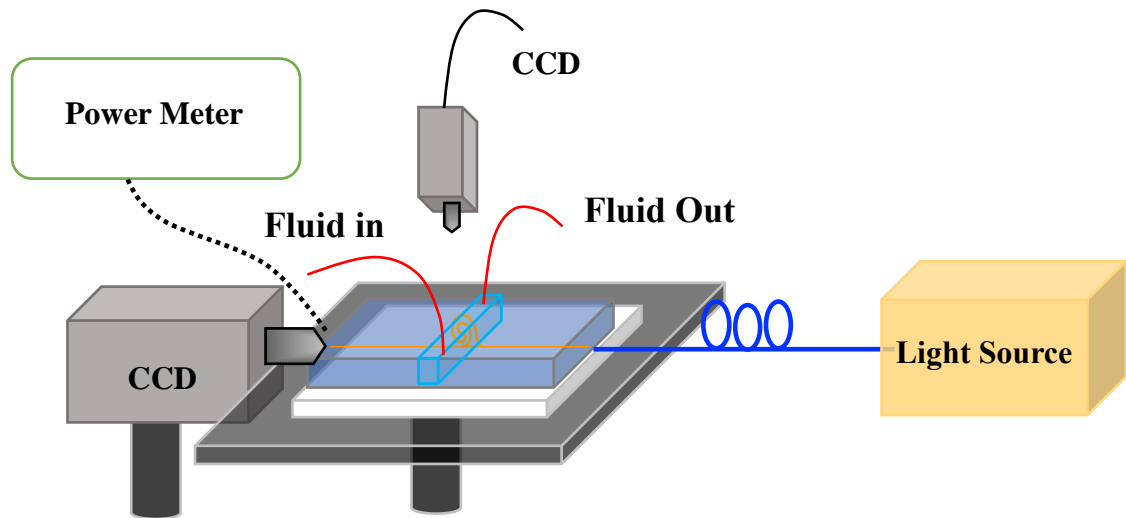


Figure 2-12 Experimental setup for achieving optimal coupling of the sensor

The utilization of the Hamamatsu camera system and the power meter ensures that the coupled light is strong enough before connecting the waveguide sensor chip to the optical spectrum analyzer, as shown in Fig. 2-12.

2.5 Results and discussions

2.5.1 Transmission spectra of the spiral optofluidic sensor

After the coupling process, the transmission spectra of the four optofluidic sensor chips are recorded. The transmission spectra are received by the optical spectrum analyzer (OSA) (Ando AQ-6315). Figure 2-13 shows the transmission spectra of single-spiral waveguide sensor, double-spiral waveguide sensor, triple-spiral waveguide sensor, and quadruple-spiral waveguide sensor, respectively.

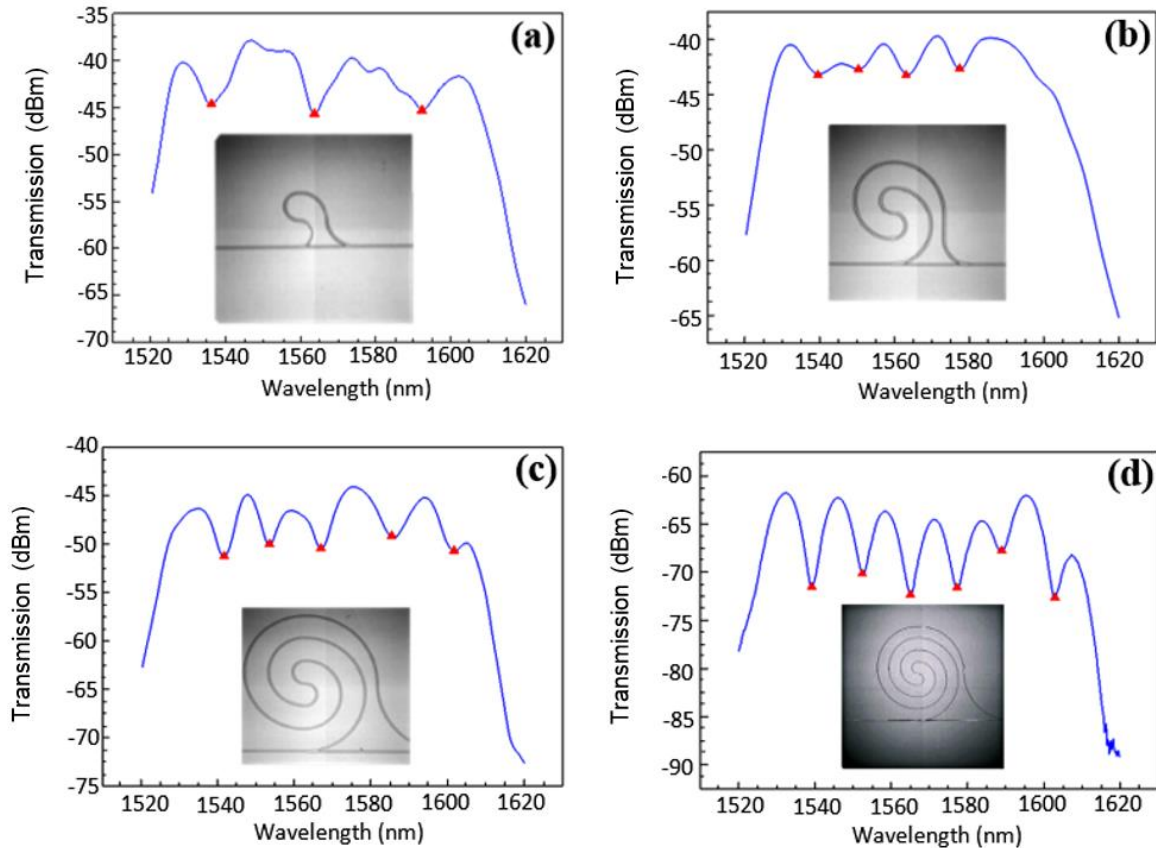


Figure 2-13 Original transmission spectra of spiral waveguide sensors with the total lengths of the spiral curves are 376.99, 1096.73, 2261.95, and 3769.91 μm , respectively.

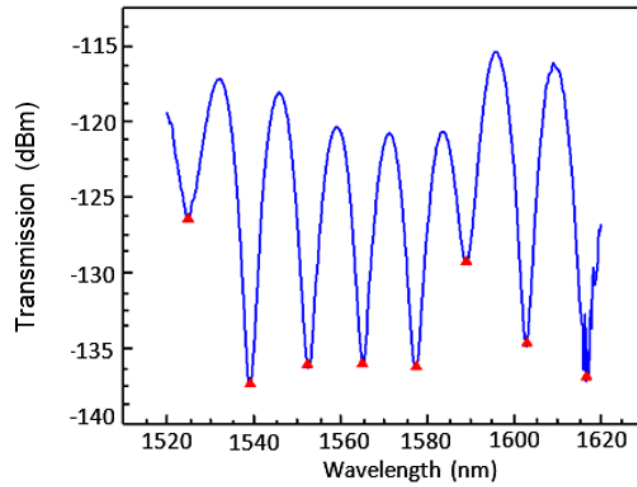


Figure 2-14 Transmission spectra of the quadruple-spiral waveguide sensor with the background removed

As the lengths of the spiral curves increase, more peaks and valleys appear, and the interference patterns become clearer and more organized. In this study, the backgrounds of all the transmission spectra have been removed so that the interference patterns are clearly shown in the figures, such as Fig. 2-14. The interference patterns are deduced from the optical path difference between the reference arm (the bus waveguide) and the sensing arm (the spiral waveguide). The values of the optical path differences of the four waveguides are described in Table 2-1.

Table 2-1 Optical path differences of single, double, triple, and quadruple-spiral waveguide sensor

Length of the spiral curves of the spiral waveguides (μm)	Length of the bus waveguides (μm)	Optical path difference (μm)
376.99	90	192.74
1096.73	180	916.73
2261.95	250	2011.95
3769.91	480	3289.91

2.5.2 Temperature sensing

A copper hotplate is utilized for adjusting the temperature of the sensor chip during temperature sensing. The area of the hotplate surface is larger than that of the sensor chip to ensure unified temperature across the whole sensor chip. The hotplate is first installed on the optical stand, and then the sensor chip is stacked on top of the hotplate and fixed with adjustable screws. A temperature monitor is connected to the hotplate to control the temperature variation. Upon every change in temperature, a few minutes must be allowed for the environment of the sensor chip to reach thermal equilibrium. As stated before, the spiral-shaped waveguide sensor can be considered as an unbalanced MZI with the sensing window structures denoted here as L_1 and L_2 . The shift in the resonance wavelength of the transmission spectra with respect to temperature T is described as follows [155] :

$$S = \frac{D\lambda}{DT} = \frac{a_{eff} \cdot (L_1 - L_2)}{m} \quad (2.4)$$

where $\Delta\lambda$ is the change of resonance wavelength, and can be expressed as

$$D/I = \frac{(L_1 - L_2)}{m} \Delta n_{eff} \quad (2.5)$$

and where ΔT is the variation of temperature, L_1 is the length of the sensing arm, L_2 is the length of the reference arm, m is the order of the transmission mode and α_{eff} is the thermo-optic coefficient (TOC) of the waveguide material. In our case, the waveguide material SU-8-2 has a negative TOC of around $-1.1 \times 10^{-4} K^{-1}$. Δn_{eff} denotes the change in the effective refractive index of the waveguide, which is caused by the sensing media.

The experiment of temperature sensing starts with no liquid infusion inside the microchannel and with a continuous increase in the hotplate temperature. The single-spiral optofluidic waveguide sensor is tested first. Figure 2-15 shows the microscopic image and 3D image of the waveguides of the single-spiral optofluidic sensor. The SU-8-2 waveguide is fabricated with an fs laser scan speed of 5 $\mu\text{m/s}$. The width of the waveguide is 5.724 μm and is measured based on the 3D image collected by a 3D optical surface profiler (Zygo[®], USA). Figure 2-16 is an image of the coupled light recorded by the Hamamatsu camera head.

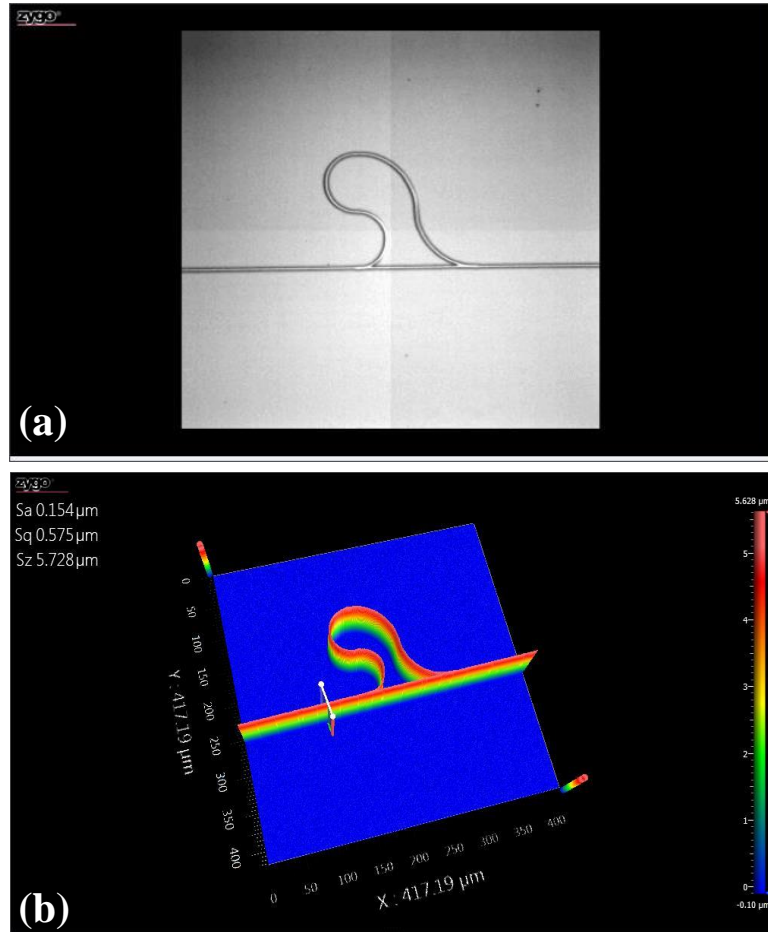


Figure 2-15 (a) Image of the single-spiral waveguide; (b) 3D profiler image of the single-spiral waveguide. The width of the waveguides in this sensor is 5.724 μm.

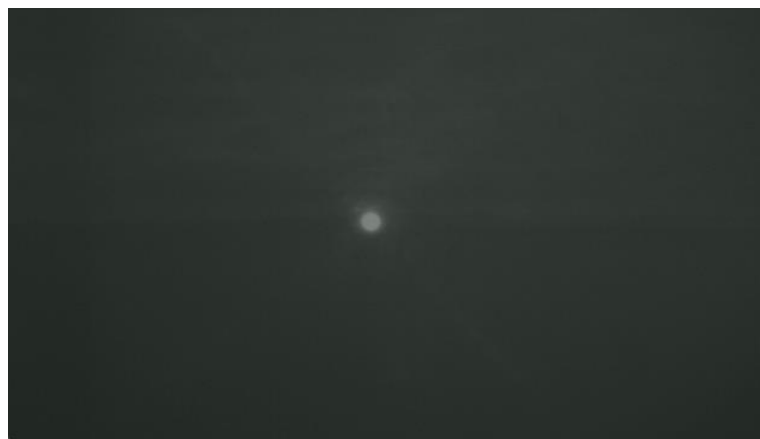


Figure 2-16 Near-field image of Coupled light transmitted by the spiral waveguide shown in Fig. 2-15.

Figure 2-17 displays the transmission spectra of the single-spiral waveguide sensor at five temperatures (22.2, 24.2, 26.2, 28.2, and 30.2°C). The temperature dependences of the individual peaks and valleys of the transmission spectra are shown in Figs. 2-18, 19, 20, and 21. A blue shift is seen from the transmission spectra, which is caused by the negative TOC of the SU-8-2 waveguides.

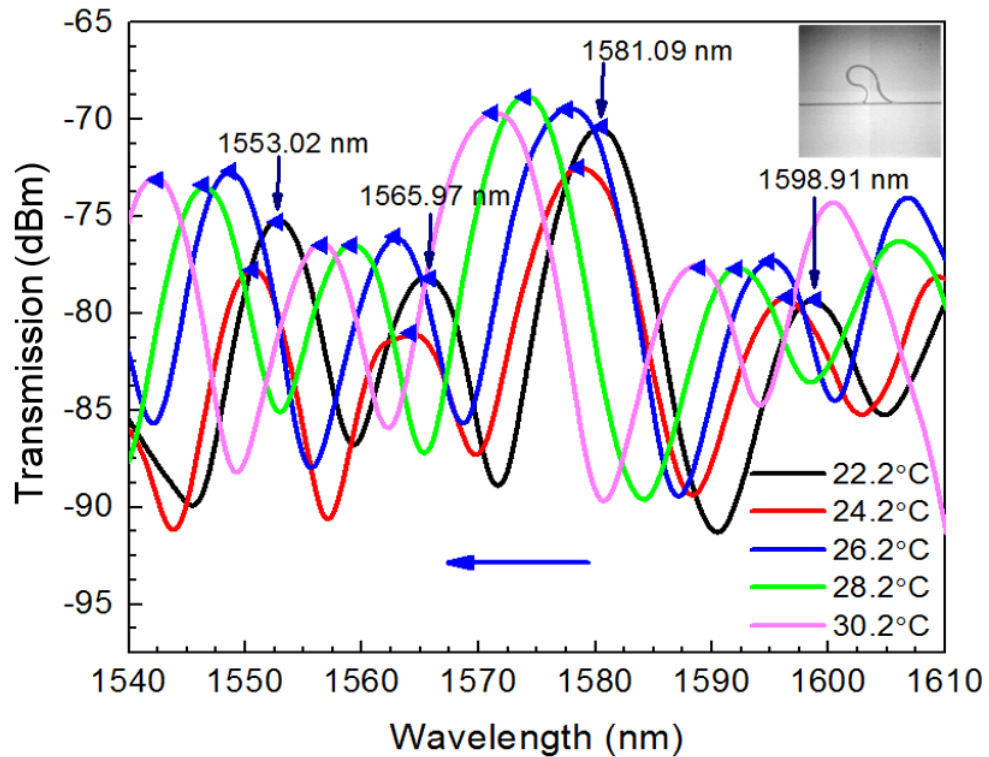


Figure 2-17 Temperature dependences of the transmission spectra of the single-spiral waveguide sensor.

In order to calibrate for further measurement of the temperature change, peak wavelengths are identified from the transmission spectra. Four shifts of the peak wavelengths are measured to calculate the sensitivities of the single-spiral sensor. The shift of the peak wavelengths at an initial peak wavelength of 1553.02 nm is shown in Fig.

2-18. The sensitivity of these shifts is measure by calculating the slope of the linear fit of the shifts of these peak wavelengths. The equation $y = Sx + I$ fits into the peak shifts, where $S = -1.31 \pm 0.06 \text{ nm}/^\circ\text{C}$ is the sensitivity, and $I = 1582.17 \pm 1.52 \text{ nm}$ is the intercept.

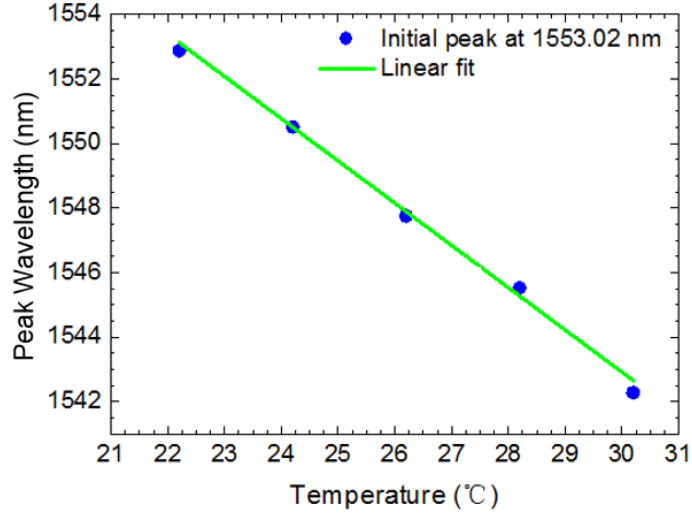


Figure 2-18 Shifts of the peak wavelengths with an initial value at 1553.02 nm in the transmission spectra of temperature sensing by the single-spiral waveguide sensor

Next, the shifts with an initial peak wavelength of 1565.97 nm are read from the transmission spectra (Fig. 2-17) and the values are shown in Fig. 2-19. The sensitivity of these shifts is $-1.20 \pm 0.02 \text{ nm}/^\circ\text{C}$. It is calculated by fitting the equation $y = Sx + I$ into the shifts of the peak wavelengths, where the sensitivity S is the slope and the intercept $I = 1592.39 \pm 1.47 \text{ nm}$.

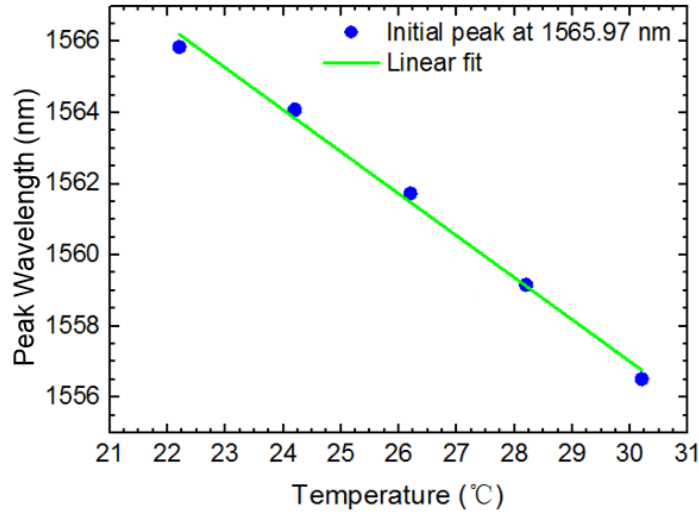


Figure 2-19 Shifts of the peak wavelengths with an initial value at 1565.97 nm in the transmission spectra of temperature sensing by the single-spiral waveguide sensor

Figure 2-20 gives the shifts with an initial peak wavelength at 1581.09 nm in the transmission spectra (Fig. 2-17). For the above shifts, the sensitivity is -1.21 ± 0.06 nm/°C, which is obtained from the slope of the linear fitting equation of the peak shifts of which the intercept is 1590.68 ± 1.47 nm. The last group of shifts with an initial peak wavelength of 1598.91 nm are demonstrated in Fig. 2-21. The sensitivity of these shifts is -1.23 ± 0.02 nm/°C, and $I = 1626.24 \pm 1.48$ nm is the intercept of the linear fit equation of the peak shifts. It can be observed that the sensitivities of the single-spiral waveguide sensor varying from -1.20 to -1.31 nm/°C. The difference in sensitivities of the four groups of peaks indicates that it is not accurate enough to calculate an average sensitivity of this sensor. Instead, sensitivities for each group of peak wavelengths should be calibrated for further temperature sensing.

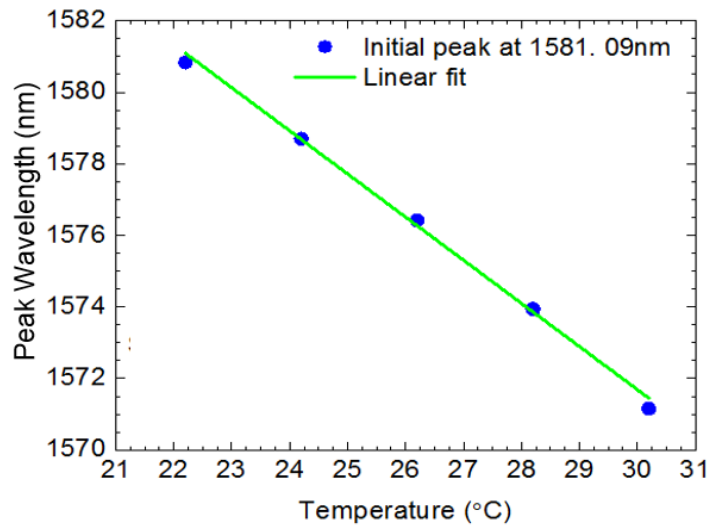


Figure 2-20 Shifts of the peak wavelengths with an initial value at 1581.09 nm in the transmission spectra of temperature sensing by the single-spiral waveguide sensor

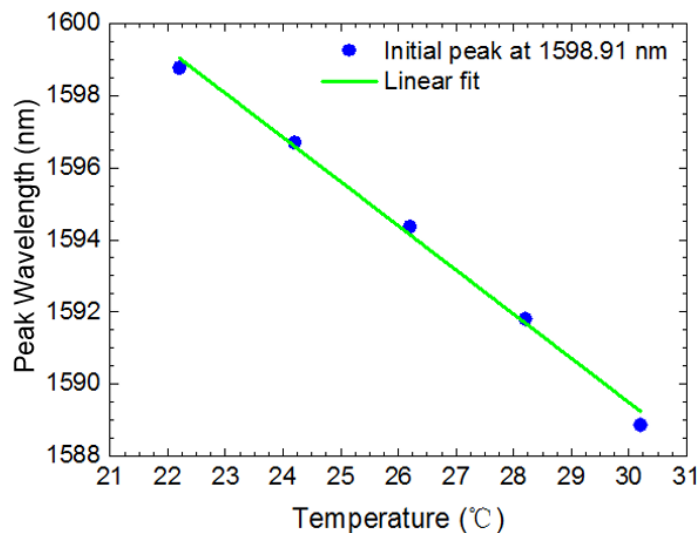


Figure 2-21 Shifts of the peak wavelengths with an initial value at 1598.91 nm in the transmission spectra of temperature sensing by the single-spiral waveguide sensor

Temperature sensing of the double-spiral optofluidic sensor is carried out by attaching the hotplate of increased temperature below the sensor chip. The microscopic image and 3D image of the double-spiral waveguide are first recorded to present the

shape of these waveguides. By measuring the sizes of the waveguides with the 3D optical surface profiler, the widths of the bus waveguide and the spiral waveguide are obtained, which are of the same value. This shows that under the same scan speed, the nonlinear interaction between femtosecond laser pulses and photoresist material is not influenced by the shape of the structure that is being fabricated.

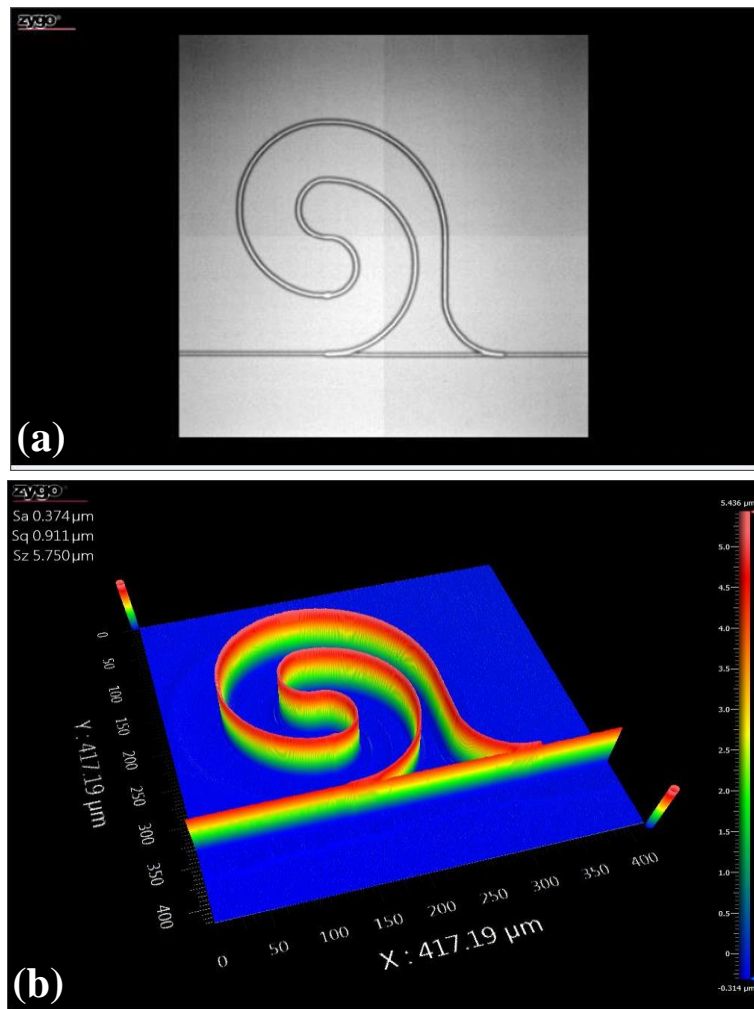


Figure 2-22 (a) Image of the double-spiral waveguide (b) 3D profiler image of the double-spiral waveguide. The width of this group of waveguides is 5.872 μm.

The SU-8-2 waveguide is fabricated with the fs laser scan speed of 5 $\mu\text{m/s}$. Figure 2-23 shows an image of the coupled light collected by the Hamamatsu camera head. The sensing of temperature change can start once the coupled light captured by the camera is bright enough.

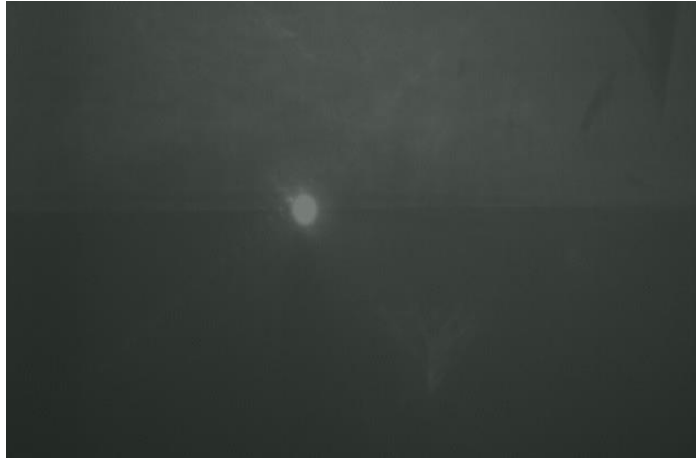


Figure 2-23 Near-filed image of Coupled light transmitted by the spiral waveguide shown in Fig. 2-22

Seven temperatures (21.8, 23.8, 25.8, 27.8, 29.8, 31.8, and 33.8°C) are tested with the double-spiral waveguide sensor and its transmission spectra are shown in Fig. 2-24. A blue shift is seen from the transmission spectra, which is caused by the negative TOC of the SU-8-2 waveguides. Figures 2-25, 2-26, and 2-27 describe the temperature dependences of the individual peaks and valleys of the transmission spectra in Fig. 2-24. Three shifts are identified from the transmission spectra in order to calibrate for further measurement. Figure 2-25 describes wavelength values of the shifts with an initial peak wavelength of 1556.38 nm, of which the sensitivity is $-0.68 \pm 0.01 \text{ nm/}^\circ\text{C}$. The sensitivity

value is obtained from the slope of the linear fitting equation of the peak shifts, of which the intercept is 1570.86 ± 0.42 nm.

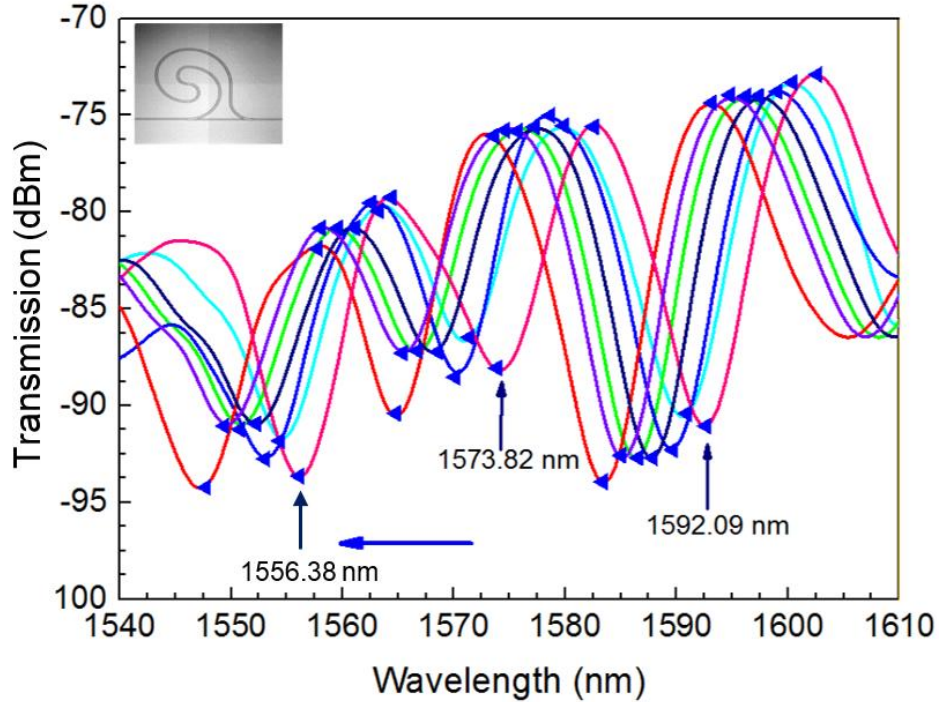


Figure 2-24 Temperature dependence of the transmission spectra of the double-spiral waveguide sensor

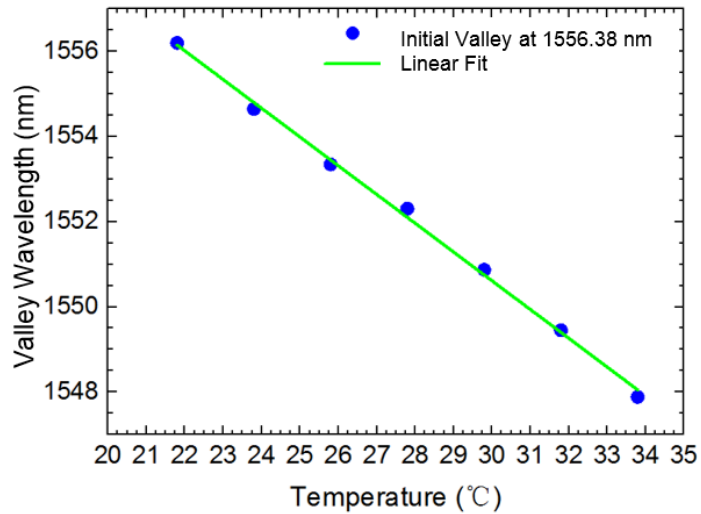


Figure 2-25 Shifts of the valley wavelengths with an initial value at 1556.38 nm in the transmission spectra of temperature sensing by the double-spiral waveguide sensor

The shifts of the valley wavelengths with an initial valley wavelength of 1573.82 nm are shown in Fig. 2-26. The sensitivity of this valley range is measured by calculating the slope of the linear fit of the valley wavelengths. The linear equation $y = Sx + I$ fits into the valley shifts, where the sensitivity is $-0.76 \pm 0.03 \text{ nm}/^\circ\text{C}$, and $I = 1589.93 \pm 0.73 \text{ nm}$ is the intercept.

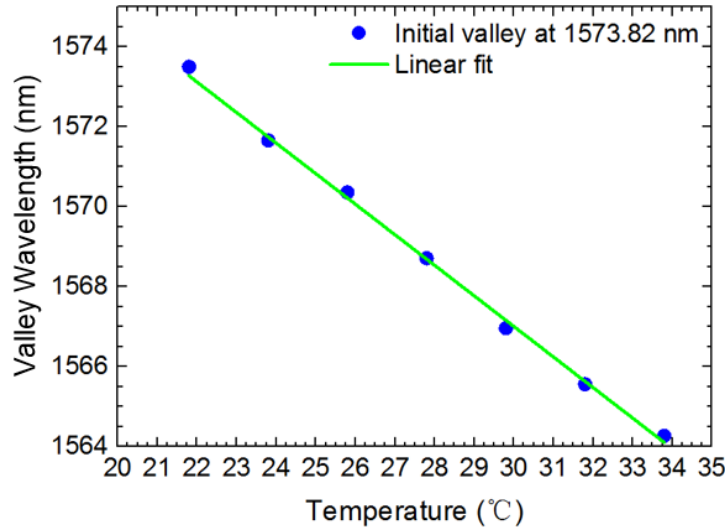


Figure 2-26 Shifts of the valley wavelengths with an initial value at 1573.82 nm in the transmission spectra of temperature sensing by the double-spiral waveguide sensor

Next, the shifts of the valleys with an initial valley wavelength of 1592.09 nm are read from the transmission spectra (Fig. 2-24) and the values are shown in Fig. 2-27. The sensitivity of the valley shifts in this range is $-0.74 \pm 0.02 \text{ nm}/^\circ\text{C}$. It is calculated by fitting the equation $y = Sx + I$ with the shift of the valley wavelengths, where the sensitivity S is the slope and the intercept $I = 1608.68 \pm 0.42 \text{ nm}$. The sensitivities of the double-spiral waveguide sensor varying from -0.68 to $-0.74 \text{ nm}/^\circ\text{C}$, which is higher than those of the

single-spiral waveguide sensor. This is expected as the optical path difference increased from 192.74 to 916.73 μm .

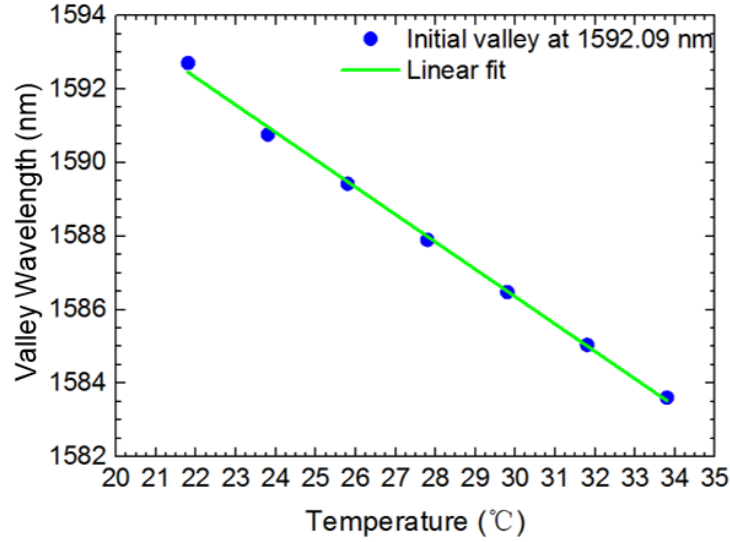


Figure 2-27 Shifts of the valley wavelengths with an initial value at 1592.09 nm in the transmission spectra of temperature sensing by the double-spiral waveguide sensor

The triple-spiral optofluidic sensor, whose spiral waveguide has spiral curves of 2261.95 μm in length, is then heated up with the hotplate for temperature sensing. Figure 2-28 shows the microscopic image and 3D image of the triple-spiral optofluidic sensor. Similarly, the SU-8-2 waveguide is fabricated with an fs laser scan speed of 5 $\mu\text{m/s}$. The width of the waveguide is 6.918 μm , read from the 3D image taken by the optical surface profiler (Zygo[®], USA). Figure 2-29 is a near-field image of the coupled light collected by the Hamamatsu camera head.

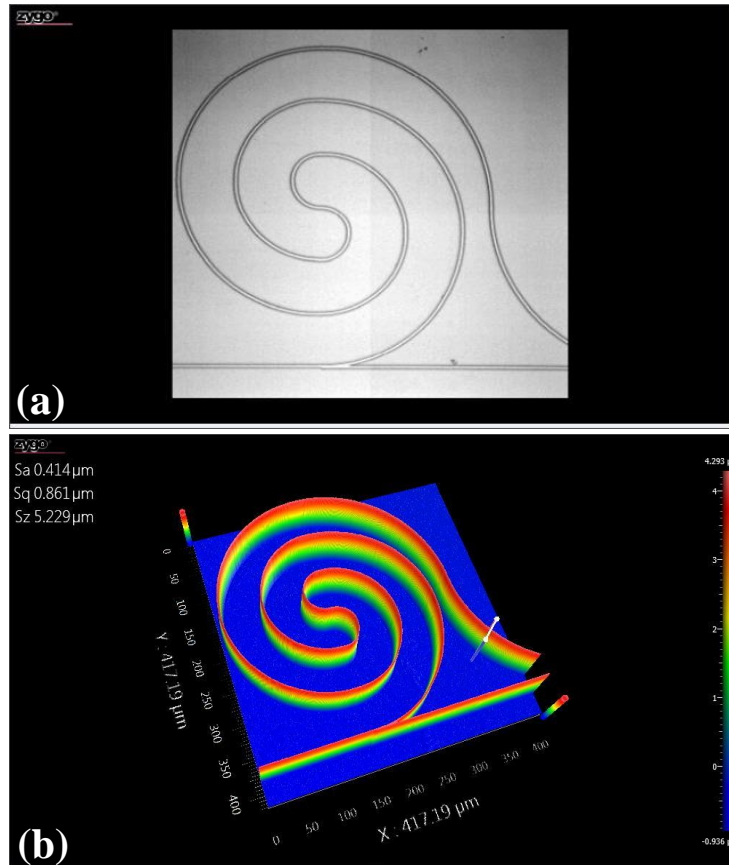


Figure 2-28 (a) Microscopic image, and (b) 3D profiler image of the triple-spiral waveguide. The width of the waveguide in the triple-spiral sensor is 6.918 μm.



Figure 2-29 Near-field image of coupled light transmitted by the spiral waveguide shown in Fig. 2-28

The triple-spiral waveguide sensor chip is heated up at five different temperatures during temperature sensing. Figure 2-30 shows the transmission spectra of the triple-spiral waveguide sensor at 23, 25, 27, 29, and 31°C, respectively. A blue shift is seen from the transmission spectra, which is a result of the negative TOC of the SU-8-2 waveguides. The temperature dependences of the individual valleys of the transmission spectra in Fig. 2-30 are shown in Figs. 2-31, 2-32, and 2-33, respectively.

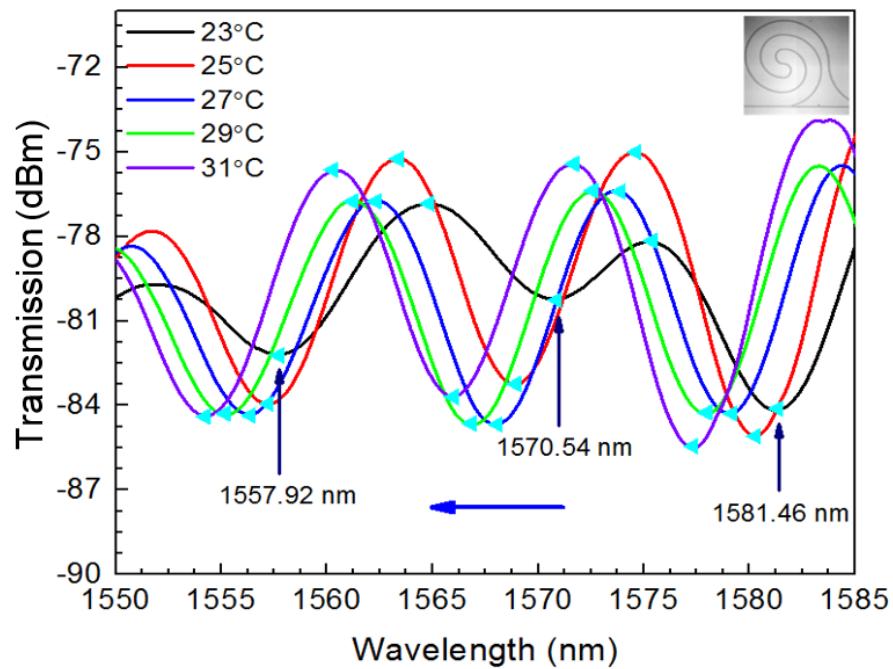


Figure 2-30 The temperature dependence of the transmission spectra of the triple-spiral waveguide sensor

In order to calibrate the spiral waveguide sensors for further measurement of temperature change, three valleys are identified from the transmission spectra in Fig. 2-30, and the shifts of the valleys are measured to calculate the sensitivities of the triple-spiral sensor. The shifts with an initial wavelength of 1557.92 nm are shown in Fig. 2-31 with a

sensitivity of -0.47 ± 0.02 nm/°C, which is measured by calculating the slope of the linear fit of the valley wavelengths. The linear fit of the valley shift is received by fitting the equation $y = Sx + I$ with the data, where $I = 1584.35 \pm 0.45$ nm is the intercept.

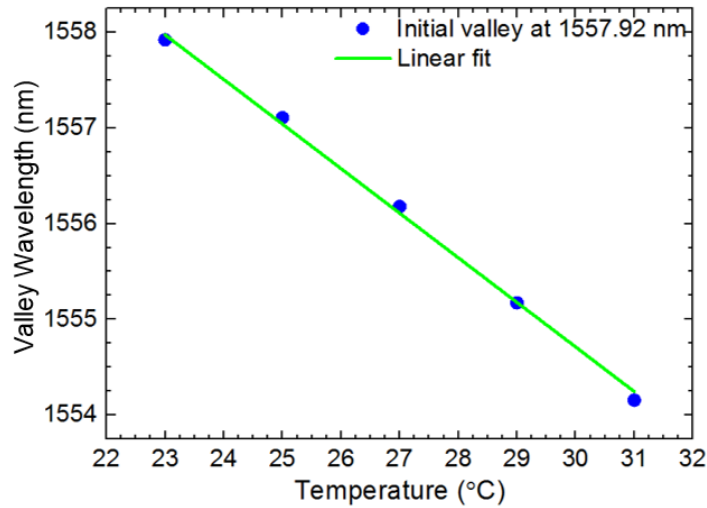


Figure 2-31 Shifts of the valley wavelengths with an initial value at 1557.92 nm in the transmission spectra of temperature sensing by the triple-spiral waveguide sensor

Next, another group of valleys with an initial valley wavelength at 1570.54 nm are read from the transmission spectra (Fig. 2-32). The sensitivity of this valley group is revealed from the linear fit of the shifts in Fig. 2-32, which is -0.51 ± 0.02 nm/°C. The linear fit follows the equation $y = Sx + I$, where $I = 1583.51 \pm 0.72$ nm is the intercept. The last group of shifts with an initial valley wavelength of 1581.46 nm and whose valley shifts are shown in Fig. 2-33. The sensitivity of this valley group is -0.54 ± 0.02 nm/°C, and $I = 1594.01 \pm 0.35$ nm is the intercept of the linear fit equation of the valley shift. It can be seen from the peak shifts (Figs. 2-31, 2-32, and 2-33) that the sensitivity values

varying from -0.51 to -0.47 nm/°C, which are the highest sensitivities achieved so far among single, double, and triple-spiral waveguide sensors.

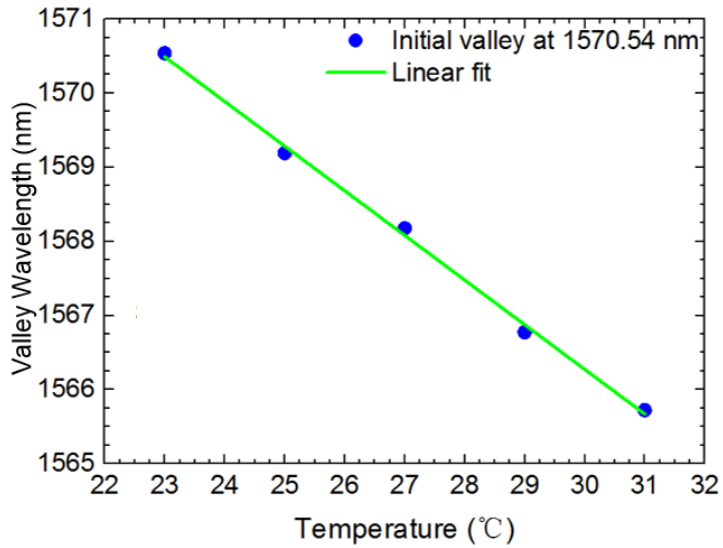


Figure 2-32 Shifts of the valley wavelengths with an initial value at 1570.54 nm in the transmission spectra of temperature sensing by the triple-spiral waveguide sensor

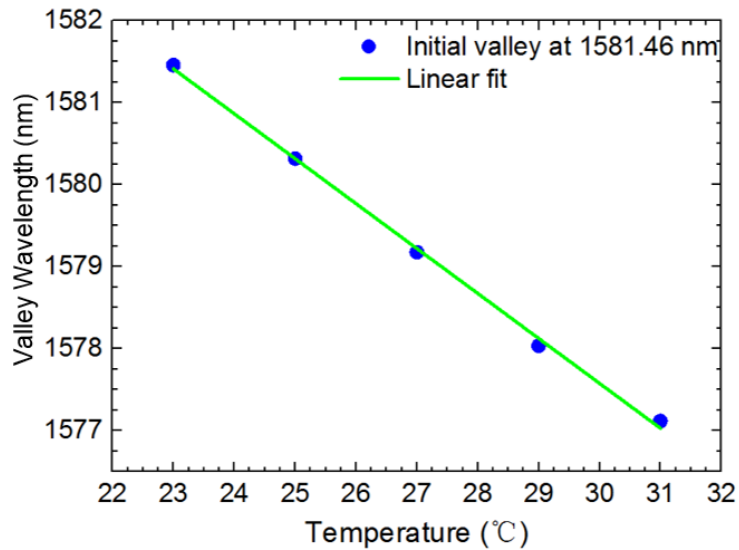


Figure 2-33 Shifts of the valley wavelengths with an initial value at 1581.46 nm in the transmission spectra of temperature sensing by the triple-spiral waveguide sensor

Temperature sensing of the quadruple-spiral optofluidic sensor is carried out by attaching the hotplate of increased temperature below this sensor chip. The microscopic image and 3D image of the quadruple-spiral waveguide group are first collected to identify the shape of the waveguides. The SU-8-2 waveguide is fabricated with an fs laser scan speed of 5 $\mu\text{m/s}$. By measuring the waveguides with the 3D optical surface profiler, the widths of the bus waveguide and the spiral waveguide are obtained, which are of the same value at 6.078 μm . Figure 2-34 is a near-field image of the coupled light collected by the Hamamatsu camera head.



Figure 2-34 Near-field image of coupled light transmitted by the spiral waveguide shown in Fig. 2-35

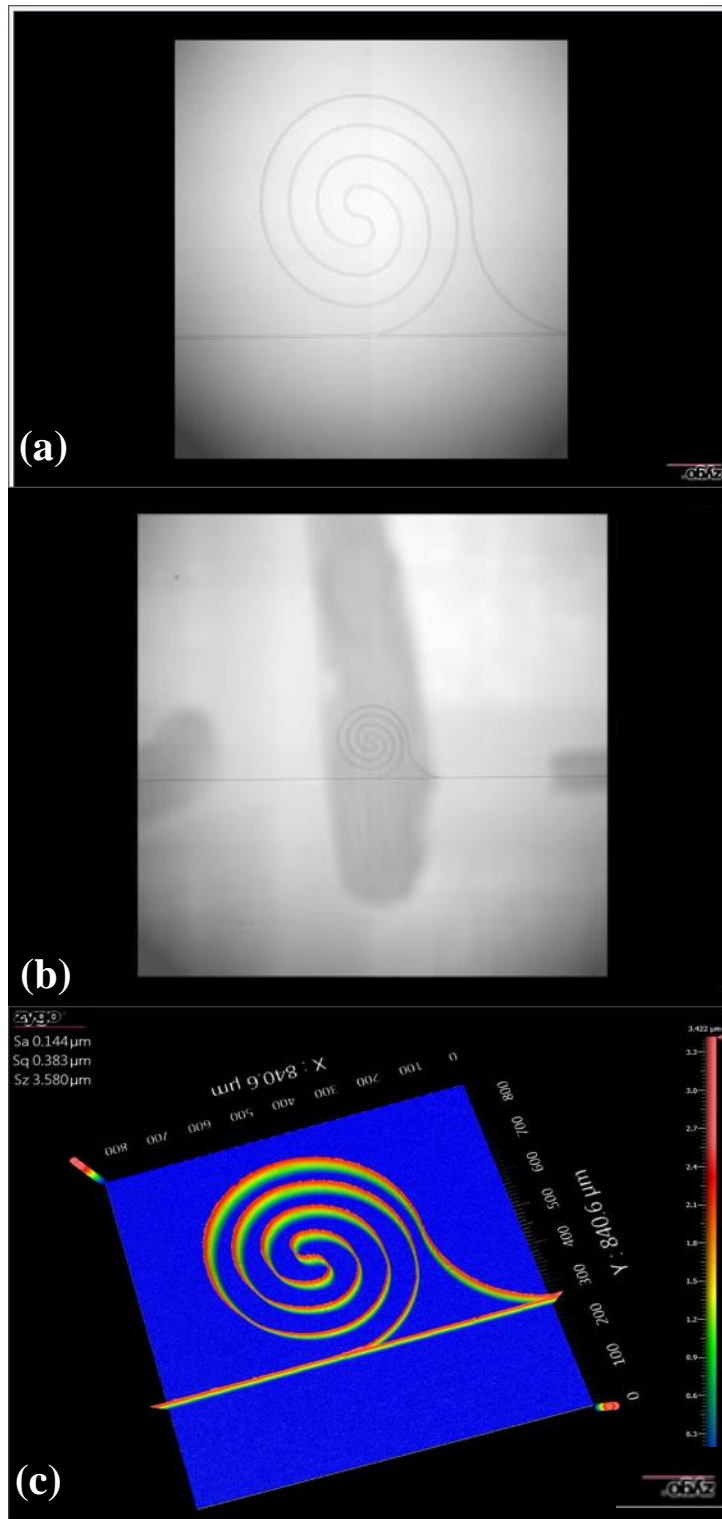


Figure 2-35 (a) & (b) Microscopic image of the quadruple-spiral waveguide, and (c) is the 3D profiler image of the quadruple-spiral waveguide.

Temperature sensing of the quadruple-spiral waveguide sensor chip is carried out by applying five temperatures (22, 24, 26, 28, and 30°C) on this sensor chip. Figure 2-36 shows the transmission spectra of the quadruple-spiral waveguide sensor at the five different temperatures. A blue shift is seen from the transmission spectra, which is a result of the negative TOC of the SU-8-2 waveguides. The temperature dependences of the individual valleys of the transmission spectra (Fig. 2-36) are shown in Figs. 2-37, 2-38, 2-39, 2-40, and 2-41, respectively. Figure 2-37 describes wavelength values of the shifts with an initial valley wavelength at 1537.24 nm in the transmission spectra (Fig. 2-36). The sensitivity is $-0.81 \pm 0.03 \text{ nm}/^\circ\text{C}$, which is obtained from the value of the slope of the linear fitting equation of the valley shift, and the intercept is $1555.87 \pm 0.69 \text{ nm}$.

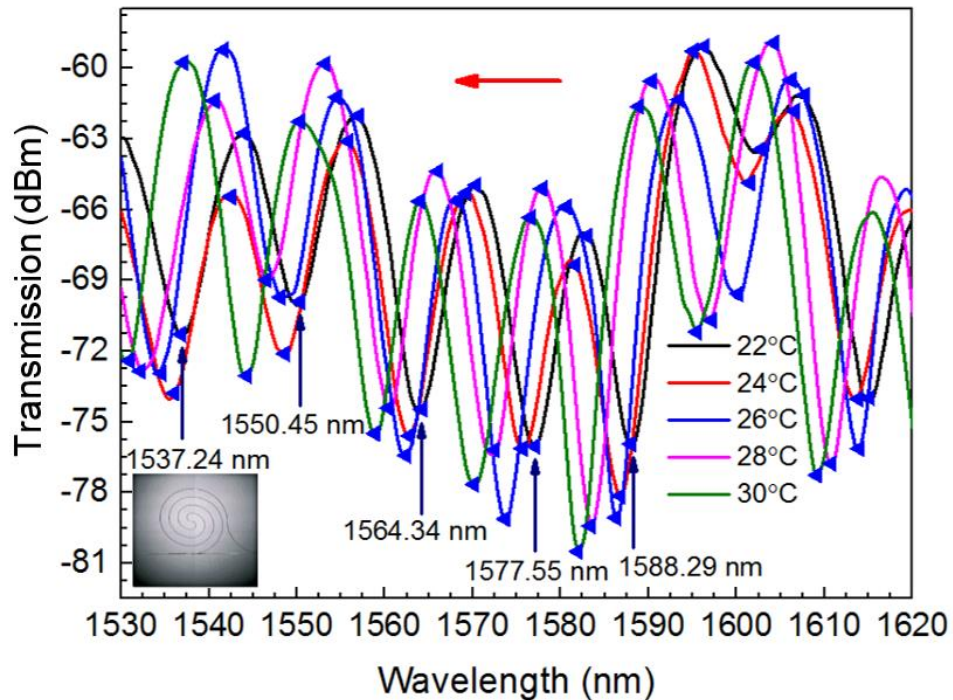


Figure 2-36 Temperature dependence of the transmission spectra of the quadruple-spiral waveguide sensor

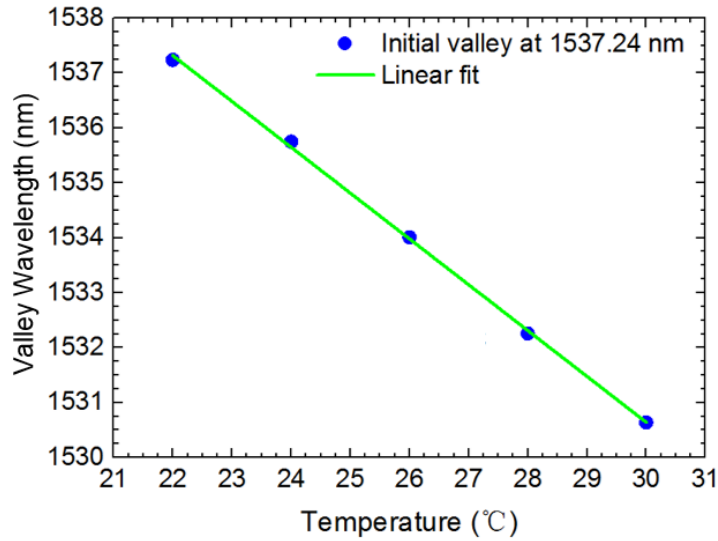


Figure 2-37 Shifts of the valley wavelengths with an initial value at 1537.24 nm in the transmission spectra of temperature sensing by the quadruple-spiral waveguide sensor

Compare with the sensitivities obtained with the triple-spiral waveguide sensor (-0.51 to -0.47 nm/°C), the sensitivity of the quadruple-spiral waveguide sensor at the valley range of 1537.24 to 1530.64 nm decreased (-0.81 ± 0.03 nm/°C). Multiple reasons can lead to this result. Firstly, quadruple-spiral waveguide sensor occupies a larger area on the SU-8-2 thin film. The height of each spiral could be different if the thickness of SU-8-2 film varies. In addition, fabricating quadruple-spiral waveguide requires the motion stage to make more stops to change its routes. It takes less than 1s to change routes, however, fs laser keeps interacting with SU-8-2 during this short period of time. This reflects on the SU-8-2 waveguide that at the points where the motion stage changes its routes, the width of the waveguide is slightly wider as the exposure time at those points is somewhat longer. Moreover, transmission loss is much higher in the quadruple-spiral waveguide as light travels the longest paths in it, in comparing with the cases of

single-spiral, double-spiral, and triple-spiral waveguides. These factors can result in unwanted propagation modes of the transmitting light, which would subsequently lead to the degradation of the sensitivity of the quadruple-spiral waveguide.

The sensitivity of the peaks with an initial valley wavelength at 1550.45 nm is -0.70 ± 0.05 nm/°C, which is also smaller than the sensitivities of the triple-spiral waveguide sensor. The sensitivity of these shifts is achieved from the linear fit of the shift of the valley wavelengths from the above range, which is illustrated in Fig. 2-38. The linear fit of the valley shift has the shape of $y = Sx + I$, where $I = 1565.89 \pm 0.91$ nm is the intercept.

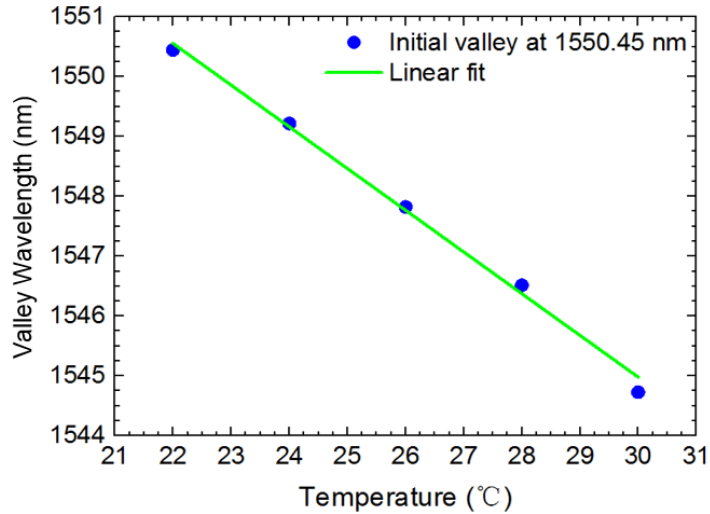


Figure 2-38 Shifts of the valley wavelengths with an initial value at 1550.45 nm in the transmission spectra of temperature sensing by the quadruple-spiral waveguide sensor

Three more groups of valley wavelengths are identified from the transmission spectra (Fig. 2-36). The shifts have initial peak wavelengths of 1564.34 nm (Fig. 2-39), 1577.55 nm (Fig. 2-40), and 1588.29 nm (Fig. 2-41), respectively. By applying linear fit

to each of the groups of valley wavelengths, the values of their sensitivities are obtained. A sensitivity of $-0.67 \pm 0.02 \text{ nm}/^\circ\text{C}$ is achieved in Fig. 2-39, while the sensitivities of the valley shifts shown in Figs. 2-40 and 2-41 are $-0.89 \pm 0.02 \text{ nm}/^\circ\text{C}$ and $-0.77 \pm 0.02 \text{ nm}/^\circ\text{C}$, respectively. As a result, the sensitivity values varying from -0.89 to $-0.67 \text{ nm}/^\circ\text{C}$, which are smaller than the sensitivities achieved by the triple-spiral waveguide sensor.

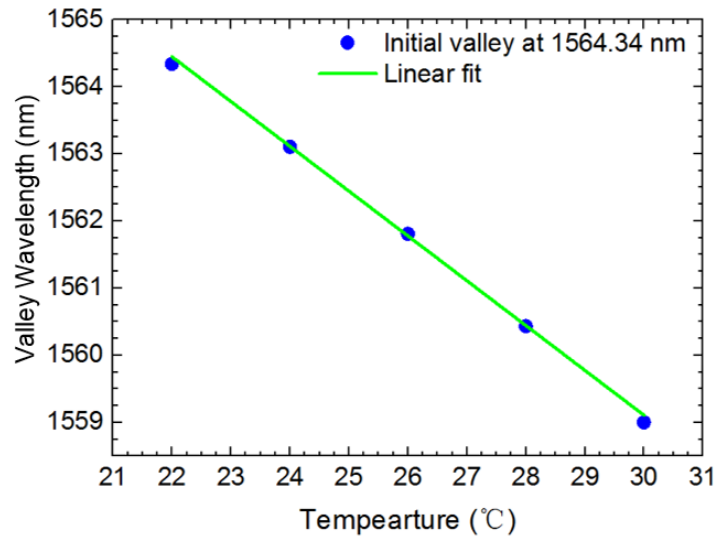


Figure 2-39 Shifts of the valley wavelengths with an initial value at 1564.34 nm in the transmission spectra of temperature sensing by the quadruple-spiral waveguide sensor

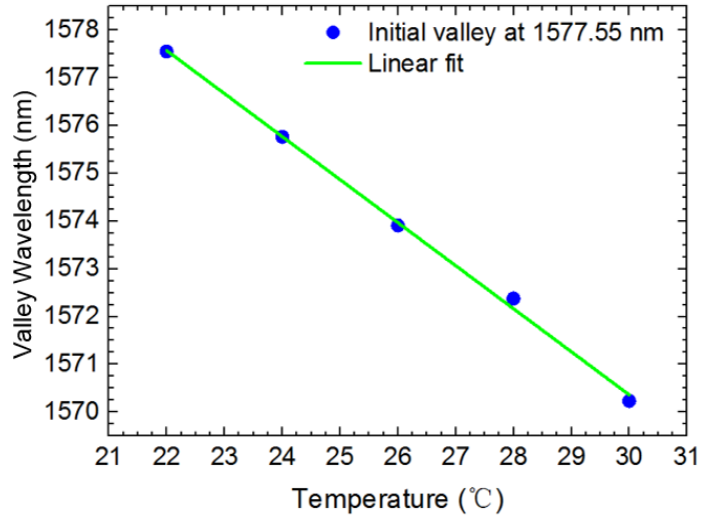


Figure 2-40 Shifts of the valley wavelengths with an initial value at 1577.55 nm in the transmission spectra of temperature sensing by the quadruple-spiral waveguide sensor

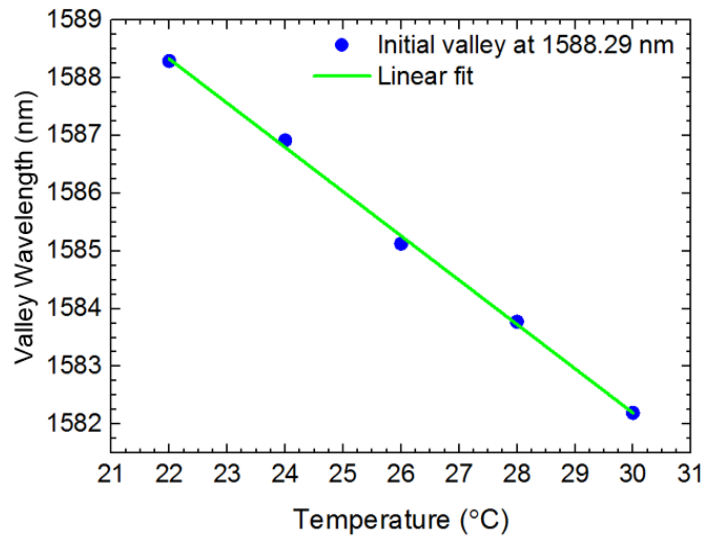


Figure 2-41 Shifts of the valley wavelengths with an initial value at 1588.29 nm in the transmission spectra of temperature sensing by the quadruple-spiral waveguide sensor

2.5.3 Refractive index sensing

The sensing of refractive index changes by the spiral-shaped optofluidic waveguide sensor was carried out by infusing liquid solutions of different refractive indices. In this study, the microchannel of the spiral waveguide sensor is filled with aqueous-based calcium chloride CaCl_2 solution. The refractive index of the CaCl_2 solution increases proportionally with respect to the solvent content in the solution, as is tested and shown below [156]:

Table 2-2 Refractive indices of CaCl_2 solutions with different concentrations. The weight percentage (wt%) denotes the mass of solute divided by total mass of solution, expressed in percentage [156].

(wt%)	Refractive Index
0.5	1.3342
7.0	1.3500
12.0	1.3625
18.0	1.3784
24.0	1.3895
30.0	1.4008

The transmission spectra of four spiral-shaped optofluidic waveguide sensors with injecting liquids of increasing refractive indices are recorded by the OSA (Ando AQ-6315). The shift in the resonance wavelength of the transmission spectra with respect to the change of refractive index is described as follows [153]:

$$S = \frac{D/\lambda}{\Delta n} = \frac{(L_1 - L_2)}{m \cdot \Delta n} \cdot \Delta n_{eff} \quad (2.6)$$

where the resonance wavelength shift is described as:

$$D/\lambda = \frac{(L_1 - L_2)}{m} \Delta n_{eff} \quad (2.7)$$

where Δn is the variation of refractive index, L_1 is the length of the sensing arm, L_2 is the length of the reference arm and m is the order or the transmission mode. Δn_{eff} denotes the change in the effective refractive index of the waveguide, which is caused by the sensing media. In this case, the cause of the change originates from the variation of the refractive index of the infused fluid solutions.

The experiment of refractive index sensing is carried out by altering the RI of the liquid inside the microchannels via the infusion of CaCl_2 solutions of different concentrations. In order to maintain the accuracy of the concentration of the injected solutions, the microchannel is thoroughly rinsed with distilled water between each injection and properly dried by blowing air into the microchannel. The single-spiral optofluidic waveguide sensor is tested first and the sensing results are shown below.

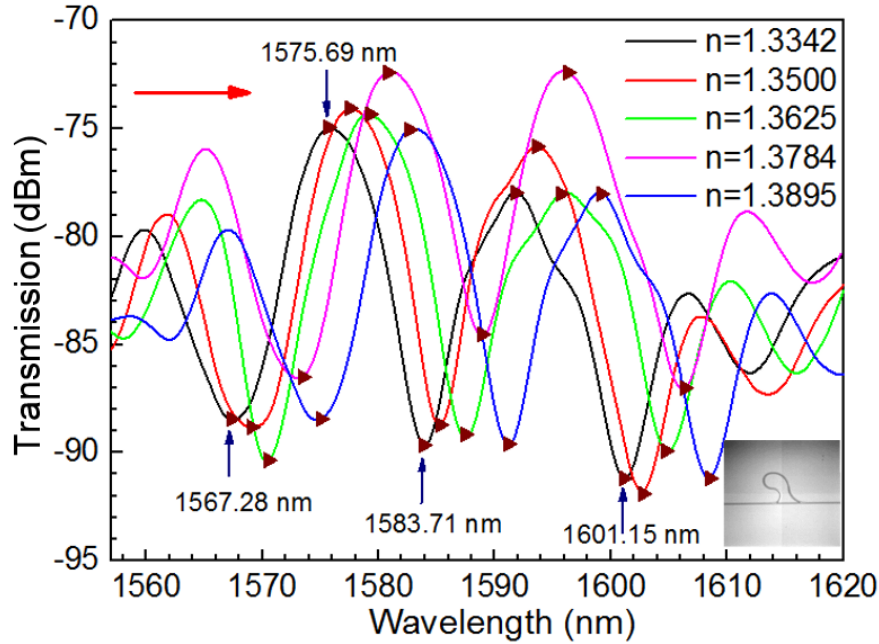


Figure 2-42 The RI dependence of the transmission spectra of the single-spiral waveguide sensor

A red shift is seen from the transmission spectra, which is caused by the increase of effective refractive index as the solutions of higher refractive indices are infused into the microchannel. In order to calibrate for further measurement of the refractive indices of different liquid samples, individual peaks and valleys are identified from the transmission spectra and the shifts of the four peaks and valleys identified in Fig. 2-42 at different RIs are calculated and shown in Figs. 2-43, 2-44, 2-45, and 2-46.

The shifts of the peak wavelengths with an initial valley wavelength of 1567.28 nm are shown in Fig. 2-43. The slope in Fig. 2-43 represents the sensitivity of the single-spiral sensor at these shifts. The linear fit of the valley shift has the shape of the equation

$y = Sx + I$, where the slope $S = 131.19 \pm 3.75$ nm/ RIU, and the intercept $I = 1392.11 \pm 5.12$ nm.

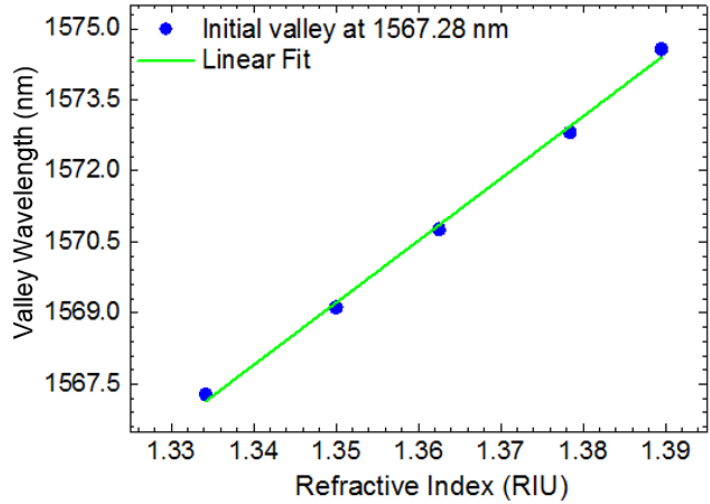


Figure 2-42 Shifts of the valley wavelengths with an initial value at 1567.28 nm in the transmission spectra of RI sensing by the single-spiral waveguide sensor

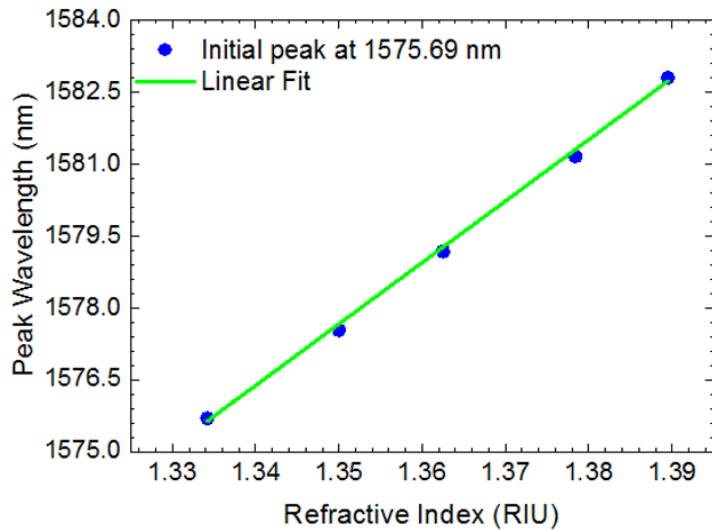


Figure 2-43 Shifts of the peak wavelengths with an initial value at 1575.69 nm in the transmission spectra of RI sensing by the single-spiral waveguide sensor

Figure 2-44 gives the shifts with an initial peak wavelength of 1575.69 nm. The sensitivity of these shifts is $S = 128.27 \pm 6.94$ nm/RIU as calculated by linear-fitting the data. It is observed that the sensitivities of the peak and valley shifts shown in Fig. 2-43 and Fig. 2-44 are mostly equal with slight difference. Slightly varied coupling condition in free space is the main cause of the sensitivity difference. This is due to with every infusion of the CaCl_2 solution, the coupling fibers from both sides of the sensor chip need to be adjusted. In Fig. 2-44, the linear fit of the valley shift follows the equation $y = Sx + I$, where S represents the slope, and $I = 1371.90 \pm 3.41$ nm is the intercept. Next, the shifts with an initial valley wavelength of 1583.71 nm are shown in Fig. 2-45. For these valley shifts, the RI sensitivity is $S = 130.12 \pm 5.95$ nm/RIU. The linear fit of the valley shift has the shape of the equation $y = Sx + I$, where S represents the slope, and $I = 1397.33 \pm 6.16$ nm is the intercept.

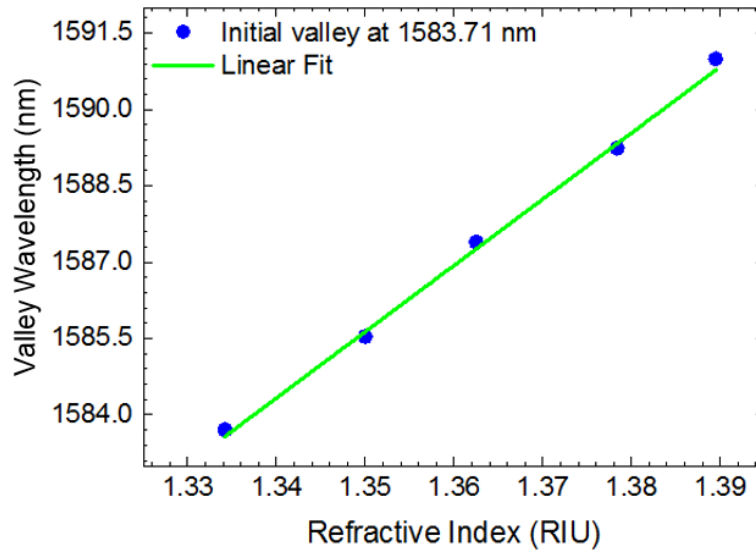


Figure 2-44 Shifts of the valley wavelengths with an initial value at 1583.71 nm in the transmission spectra of RI sensing by the single-spiral waveguide sensor

Valley wavelengths also shift from 1601.15 to 1608.54 nm in the transmission spectra of RI sensing (Fig. 2-42), which is described in Fig. 2-46. The sensitivity of the single-spiral sensor in these shifts is $S = 135.62 \pm 3.94$ nm/RIU as calculated from the equation $y = Sx + I$, where the intercept $I = 1420.04 \pm 5.37$ nm.

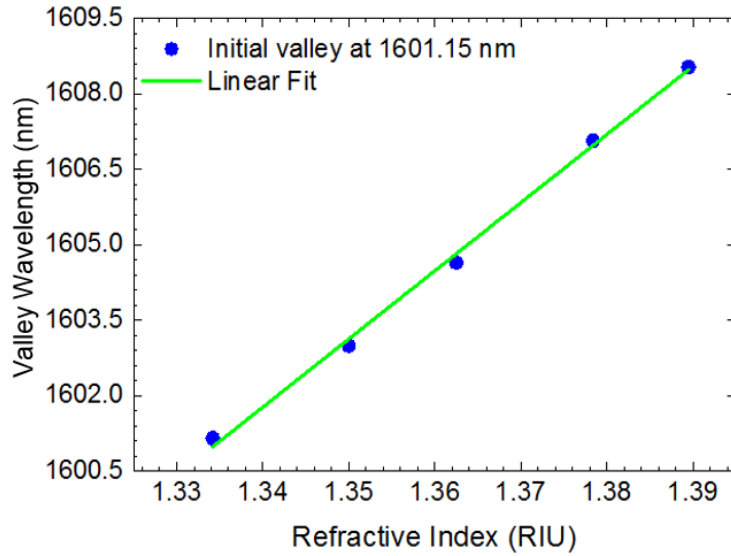


Figure 2-45 Shifts of the valley wavelengths with an initial value at 1601.15 nm in the transmission spectra of RI sensing by the single-spiral waveguide sensor

The double-spiral waveguide sensor is then infused with CaCl_2 solutions of different concentrations for RI sensing. Figure 2-47 shows the transmission spectra of the double-spiral waveguide sensor filled with CaCl_2 of five different RIs ($n = 1.3342, 1.3500, 1.3625, 1.3784, 1.3895$). The refractive index dependences of the peaks and valleys of the transmission spectra are shown in Figs. 2-48 and 2-49. A red shift is seen from the transmission spectra, which is caused by the increase of the effective refractive index as the solutions of higher refractive indices are infused into the microchannel.

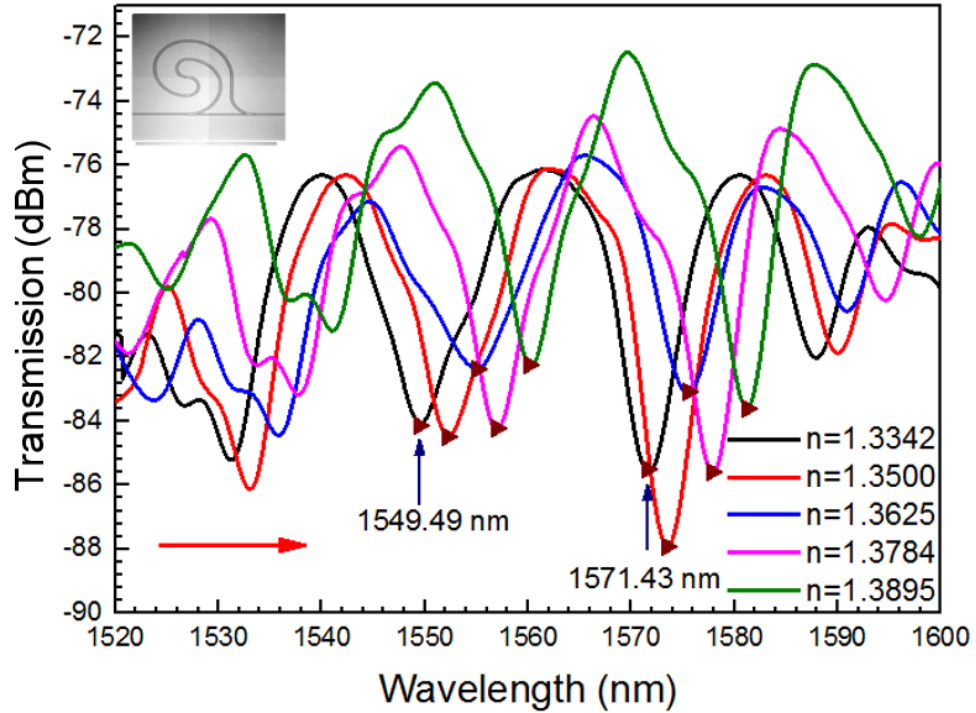


Figure 2-46 The RI dependence of the transmission spectra of the double-spiral waveguide sensor

In order to calibrate for further measurement of refractive indices of different liquids, valley wavelengths are identified from the transmission spectra (Fig. 2-47) and the shifts are calculated in Figs. 2-48 and 2-49 to obtain the RI sensitivities of the double-spiral waveguide sensor. The shifts for a valley with an initial wavelength of 1549.49 nm are first read from Fig. 2-47. The sensitivity of this group of valley wavelengths is 162.46 ± 5.4 nm/RIU, which is higher than the sensitivities achieved by the single-spiral waveguide sensor. The value of the sensitivity is obtained by the linear fit equation of the shift of the valley wavelengths starting from 1549.49 nm, and the intercept for the linear fit is $I = 1355.40 \pm 5.74$ nm. Next, from 1571.43 to 1580.83 nm, a shift of valley

wavelengths is obtained from the transmission spectra (Fig. 2-47). The sensitivity of this group of valley wavelengths is 161.45 ± 5.74 nm/RIU, which is the slope of the linear equation of the shift of valley wavelengths in Fig. 2-49. The intercept of the linear equation is 1346.50 ± 7.83 nm. It can be observed that the values of sensitivities have increased from single-spiral to double-spiral waveguide sensors.

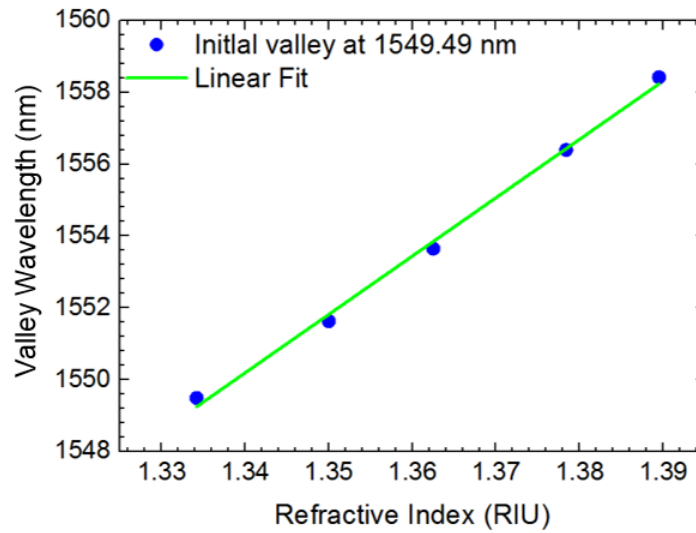


Figure 2-47 Shifts of the valley wavelengths with an initial value of 1549.49 nm in the transmission spectra of RI sensing by the double-spiral waveguide sensor

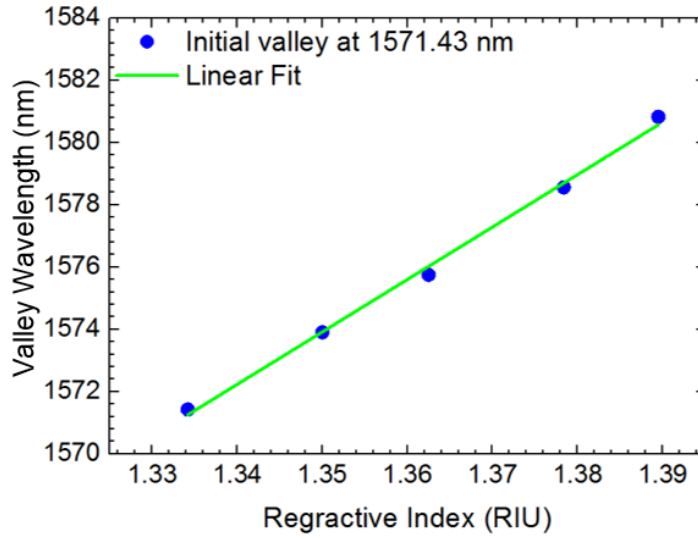


Figure 2-48 Shifts of the valley wavelengths with an initial value at 1571.43 nm in the transmission spectra of RI sensing by the double-spiral waveguide sensor

RI sensing is carried out with a triple-spiral waveguide sensor by infiltrating CaCl_2 of five different concentrations into the microchannel. Figure 2-50 shows the transmission spectra of the triple-spiral waveguide sensors at five RIs ($n= 1.3625, 1.3784, 1.3895, 1.4008, \text{ and } 1.4240$). The refractive index dependences of the peaks and valleys of these transmission spectra are shown in Figs. 2-51, 2-52, 2-53, and 2-54. A red shift is observed on the transmission spectra, which is caused by the increase of effective refractive index when increasing the refractive index of the solutions infused into the microchannel.

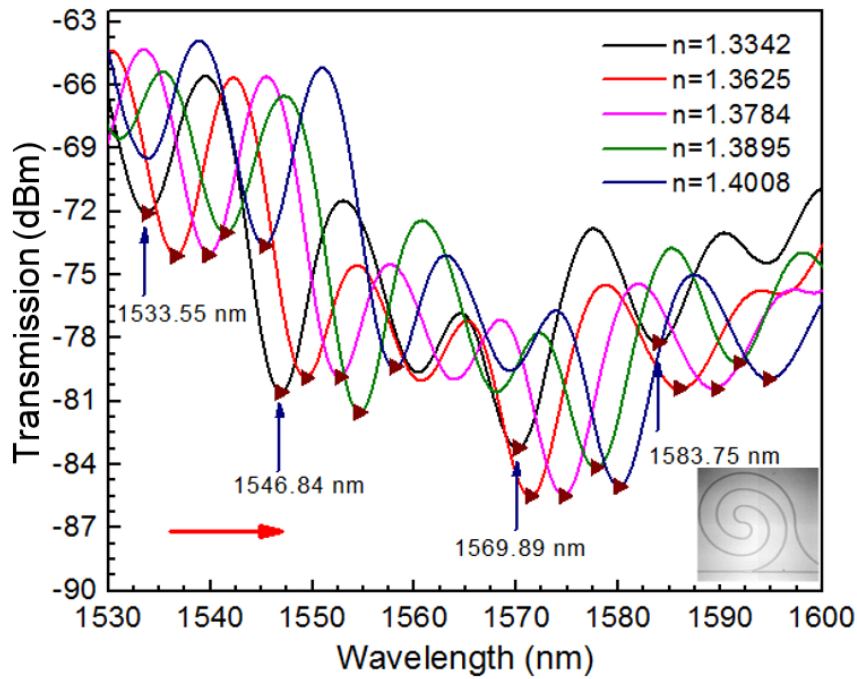


Figure 2-49 The RI dependence of the transmission spectra of the triple-spiral waveguide sensor

In order to calibrate for further measurement of the refractive indices of different liquids, four shifts of valleys are identified from the transmission spectra (Fig. 2-50) to obtain the RI sensitivities of the triple-spiral waveguide sensor. The valley wavelengths with an initial valley wavelength of 1533.55 nm are first read from Fig. 2-50. The sensitivity of this group of valley wavelengths is 188.78 ± 3.76 nm/RIU, which is higher than the sensitivities achieved by both the single-spiral and double-spiral waveguide sensors. The value of the sensitivity is obtained by the linear fit equation of the shift of the valley wavelengths starting from 1533.55 nm, and the intercept is $I = 1276.41 \pm 5.24$ nm. Next, the shifts with an initial valley wavelength at 1546.84 nm are identified from the transmission spectra (Fig. 2-50). The sensitivity of this group of valley wavelengths is

179.96±6.44 nm/ RIU, which is the slope of the linear equation of the shift of valley wavelengths in Fig. 2-52. The intercept of the linear equation is 1301.64±8.96 nm.

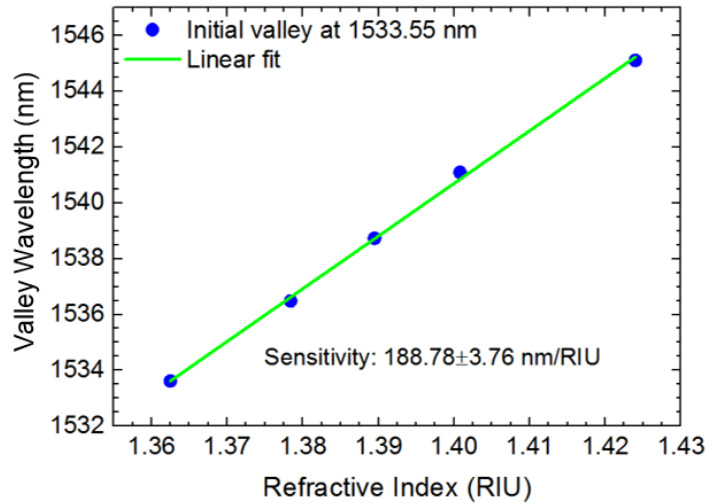


Figure 2-50 Shifts of the valley wavelengths with an initial value at 1533.55 nm in the transmission spectra of RI sensing by the triple-spiral waveguide sensor

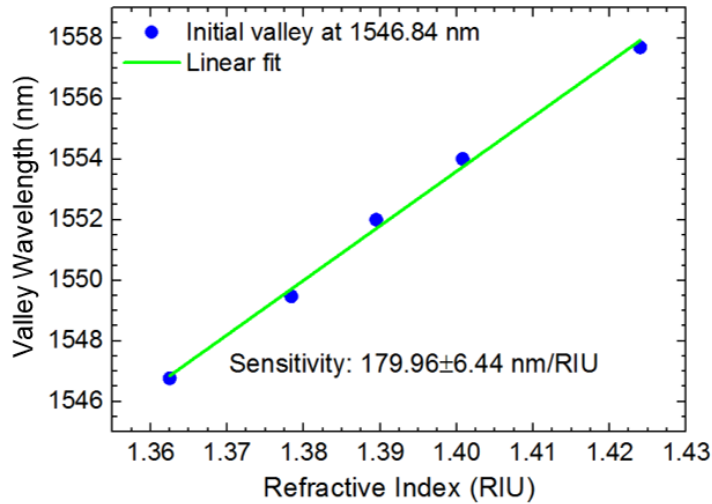


Figure 2-51 Shifts of the valley wavelengths with an initial value at 1546.84 nm in the transmission spectra of RI sensing by the triple-spiral waveguide sensor

From Fig. 2-50, two more groups of valley wavelengths shifting towards the longer wavelength are identified. The sensitivity for the shifts with an initial valley wavelength of 1569.89 nm is 167.97 ± 2.64 nm/RIU, while for the shifts with an initial valley wavelength of 1583.75 nm, the sensitivity is 180.75 ± 5.55 nm/RIU. This range of sensitivities achieved by the triple-spiral waveguide sensor is, thus far, the highest among the single-spiral, double-spiral and triple-spiral waveguide sensors. The values of sensitivities are obtained from the linear fit of the shift of the valley wavelengths which has the form $y = Sx + I$, where the intercepts for Figs. 2-53 and 2-54 are 1340.89 ± 3.67 nm and 1337.49 ± 7.72 nm, respectively.

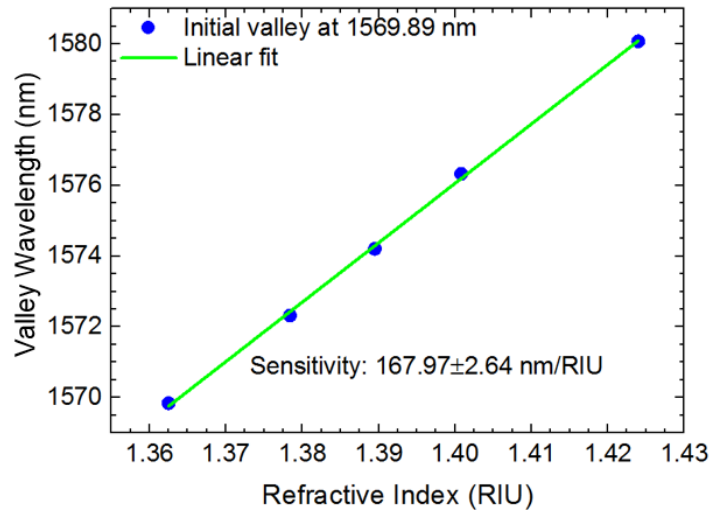


Figure 2-52 Shifts of the valley wavelengths with an initial value at 1569.89 nm in the transmission spectra of RI sensing by the triple-spiral waveguide sensor

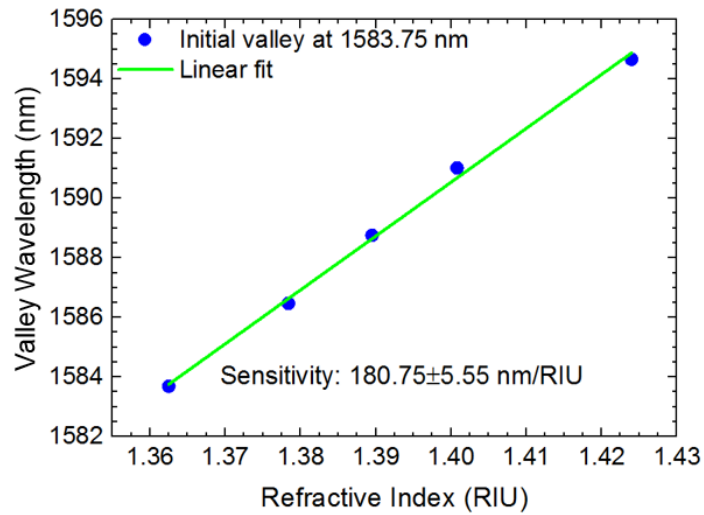


Figure 2-53 Shifts of the valley wavelengths with an initial value at 1583.75 nm in the transmission spectra of RI sensing by the triple-spiral waveguide sensor

Next, a quadruple-spiral waveguide sensor is infused with CaCl_2 of five different concentrations into the microchannel for RI sensing. Figure 2-55 describes the transmission spectra of the quadruple-spiral waveguide sensors at six RIs ($n = 1.3342$, 1.3500, 1.3625, 1.3784, 1.3895, and 1.4008). The refractive index dependences of the individual peaks and valleys of the transmission spectra are shown in Figs. 2-56, 2-57, 2-58, and 2-59. Similarly, a red shift is observed on the transmission spectra, which is caused by the increase of the effective refractive index when increasing the refractive indices of the solutions infused into the microchannel.

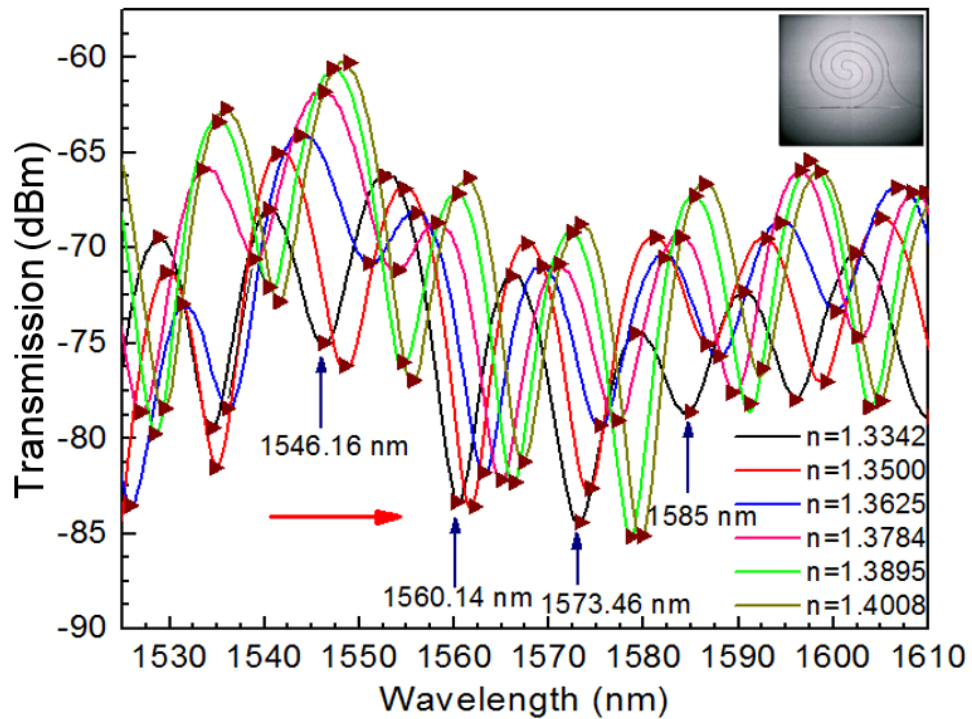


Figure 2-54 The RI dependence of the transmission spectra of the quadruple-spiral waveguide sensor

In order to calibrate for further measurement of the refractive indices of different liquids, the shifts of four valleys are identified from the transmission spectra in Fig. 2-55, and the shifts are calculated (Figs. 2-56, 2-57, 2-58, and 2-59) to obtain the RI sensitivities of the quadruple-spiral waveguide sensor. The shifts with an initial valley wavelength of 1546.16 nm are identified on Fig. 2-55. The sensitivity of these shifts is 146.57 ± 5.15 nm/RIU, which is lower than the sensitivities achieved by the triple-spiral waveguide sensor. A decrease in sensitivity is expected in quadruple-spiral waveguide sensors as the fabrication difficulty increases. Slight fluctuation in any steps in the

process of waveguide fabrication can influence the performance of the quadruple-spiral waveguide sensor (as explained in Section 2.5.2). The value of the sensitivity is obtained by the linear fit equation of the shift of the valley wavelengths, and the intercept is 1350.71 ± 7.05 nm. Next, from 1560.14 to 1567.44 nm, the shifts of valley wavelengths are identified on the transmission spectra (Fig. 2-55). The sensitivity of this group of valley wavelengths is 109.90 ± 1.98 nm/ RIU, which is the slope of the linear equation of the shift of valley wavelengths in Fig. 2-57. The intercept of the linear equation is 1413.39 ± 2.71 nm.

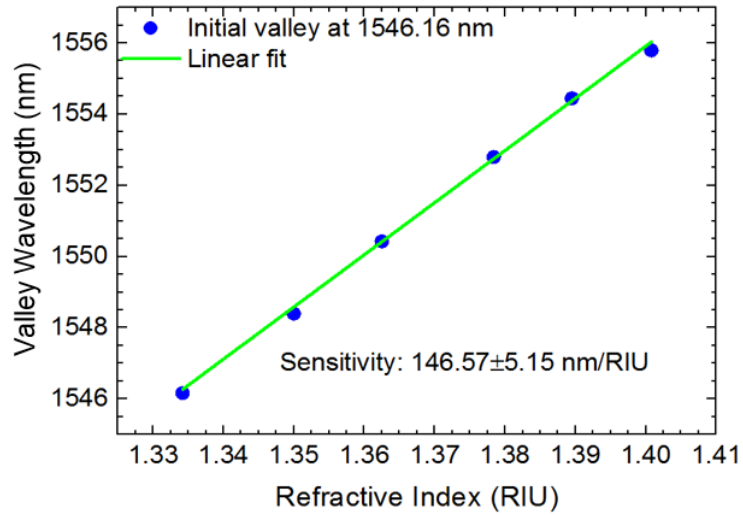


Figure 2-55 Shifts of the valley wavelengths with an initial value at 1546.16 nm in the transmission spectra of RI sensing by the quadruple-spiral waveguide sensor

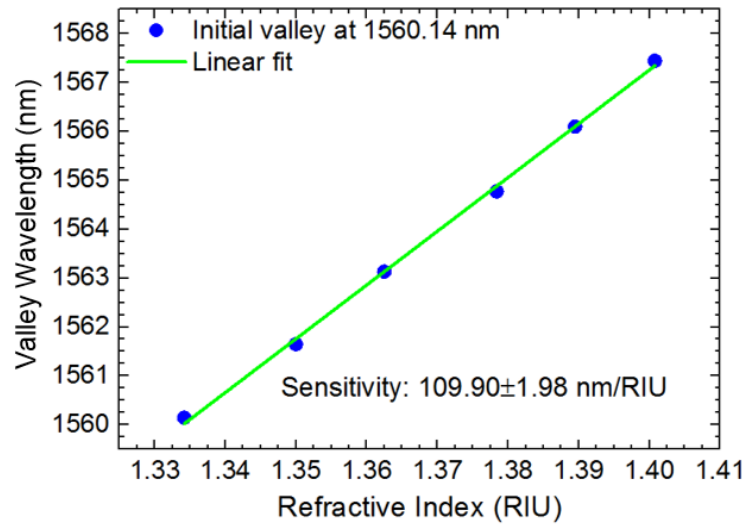


Figure 2-56 Shifts of the valley wavelengths with an initial value at 1560.14 nm in the transmission spectra of RI sensing by the quadruple-spiral waveguide sensor

From the transmission spectra in Fig. 2-55, two more groups of valley wavelengths shifting towards the longer wavelength are identified and the shifts of the valley wavelengths are shown in Figs. 2-58 and 2-59. The sensitivity for the shifts with the initial valley wavelength at 1573.46 nm is 88.35 ± 3.90 nm/RIU, while the sensitivity of the shifts with the initial valley wavelength at 1585.00 nm is 112.93 ± 2.08 nm/RIU. The values of sensitivities are obtained from the linear fit of the shift of the valley wavelengths which has the form $y = Sx + I$, where the intercepts for Figs. 2-58 and 2-59 are 1413.39 ± 2.71 nm and 1434.18 ± 2.84 nm, respectively. In conclusion, among single-spiral, double-spiral, triple-spiral, and quadruple-spiral waveguide sensors, the highest sensitivity is achieved by the triple-spiral waveguide sensor, with the sensitivities varying from 167 to 188 nm/RIU. The triple-spiral waveguide sensor is easy to fabricate with

good transmission spectra and steady interference pattern, which makes it a suitable candidate for further sensing experiments.

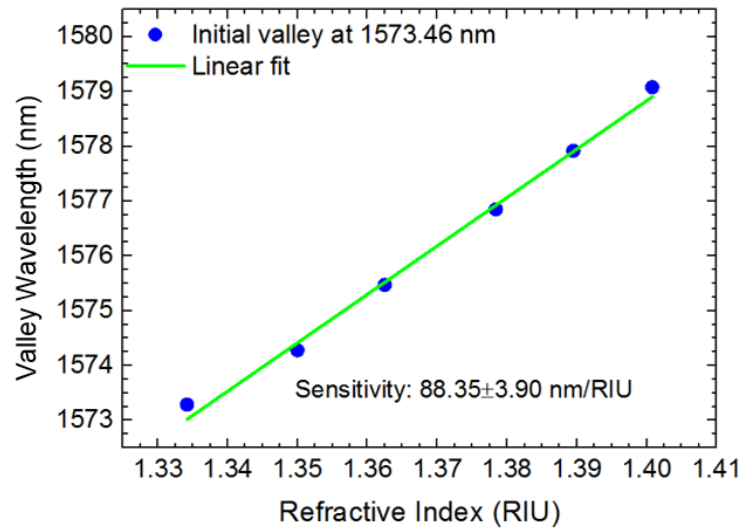


Figure 2-57 Shifts of the valley wavelengths with an initial value at 1573.46 nm in the transmission spectra of RI sensing by the quadruple-spiral waveguide sensor

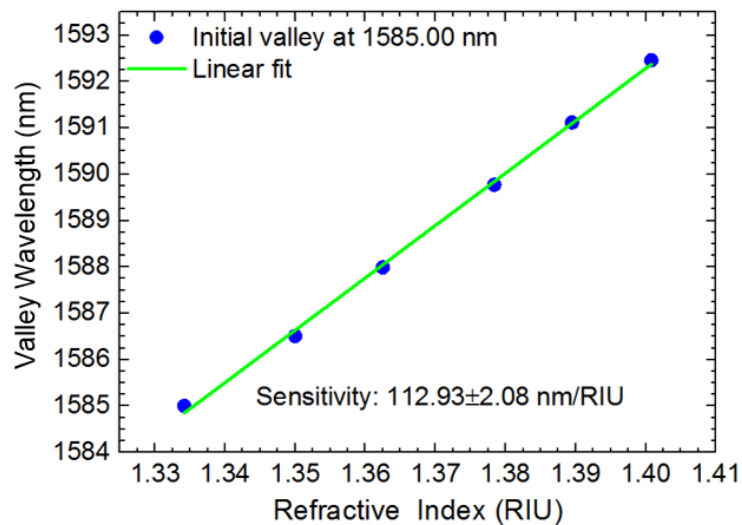


Figure 2-58 Shifts of the valley wavelengths with an initial value at 1585.00 nm in the transmission spectra of RI sensing by the quadruple-spiral waveguide sensor

2.5.4 Positive pressure sensing

Pressure sensors have been widely used in various fields, from medical applications [150], [151] to automotive [49] and aerospace devices [152]. In this study, adding positive pressure onto the sensor chips causes deformation of the microchannels, which is reflected in the shift of their transmission spectra. By calibrating the shifts in transmission spectra, one can identify the value of the added pressure on the sensor chips. The positive pressure sensing experiment is carried out by gradually stacking weights onto the spiral waveguide sensor chip and the microchannel (filled with distilled water), as shown in Figs. 2-60 and 2-61.

Transmission spectra of the four of the optofluidic waveguide sensors with increasing positive pressure are collected by the OSA (Ando AQ-6315). The sensitivity, which is the shift in the resonance wavelength of the transmission spectra with respect to the change of refractive index, is expressed as [146]:

$$S = \frac{D/\lambda}{\Delta P} = \frac{(L_1 - L_2)}{m \cdot \Delta P} \cdot \Delta n_{eff} \quad (2.6)$$

where the resonance wavelength shift expressed as:

$$D/\lambda = \frac{(L_1 - L_2)}{m} \Delta n_{eff} \quad (2.7)$$

and where ΔP is the variation of the added positive pressure, L_1 is the length of the sensing arm, L_2 is the length of the reference arm, and m is the order of the transmission mode. Δn_{eff} denotes the change of the effective refractive index of the waveguide, which is induced by the squeezing effect of liquid pressure [153] due to the increase in positive pressure. A positive pressure added onto the sensor chip causes a deformation of the

microchannel and the liquid inside the microchannel. As the liquid acts as the cladding of the sensor chip, pressure inflicted onto the sensor chip deforms the cladding and induces more propagation modes of the transmission light, consequently increasing the effective refractive index of the sensor.

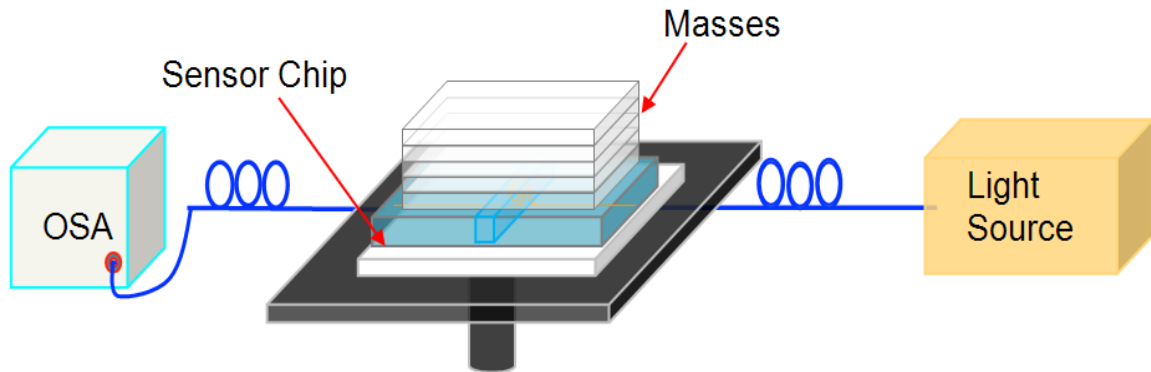


Figure 2-59 Experimental setup for positive pressure sensing



Figure 2-60 Microscopic image of the spiral sensor with water-filled microchannel

Microscopic slides (75×25 mm) are cut into four pieces to add mass onto the sensor chips. The positive pressure sensing is carried out with the single-spiral optofluidic sensor first. Figure 2-62 shows the transmission spectra of the single-spiral waveguide sensor under six positive pressures: 21.28, 42.55, 63.83, 85.11, 106.38, and 127.66 N/m². The positive pressure dependences of the individual peaks of the transmission spectra are shown in Figs. 2-63, 2-64, 2-65, and 2-66. A red shift is observed on the transmission spectra, which is caused by the increase of the effective refractive index of the sensing area. The weights added on the sensor chip increase the effective refractive index of the entire sensor chip structure given that larger numbers of propagation modes of the transmission light are excited.

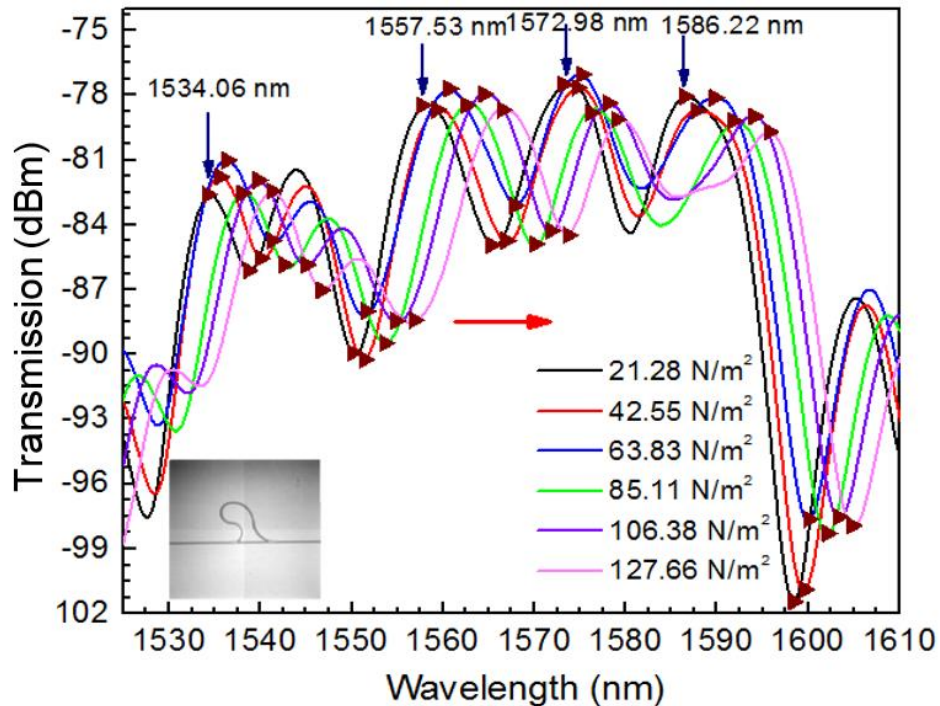


Figure 2-61 Positive pressure dependence of the transmission spectra of the single-spiral waveguide sensor

In order to calibrate for further measurement of changes in positive pressure, the shifts of four peaks are identified from the transmission spectra (Fig. 2-62) and the shifts of different positive pressures are presented in Figs. 2-63, 2-64, 2-65, and 2-66. The shifts of the peak wavelengths with an initial peak wavelength of 1534.06 nm are shown in Fig. 2-63. The sensitivity of the single-spiral sensor with the shift in peak wavelength starting from 1534.06 nm is 0.060 ± 0.003 nm/ (N/m²). The value of the sensitivity can be calculated from fitting the peak shift with $y = Sx + I$, where the intercept is 1532.42 ± 0.16 nm.

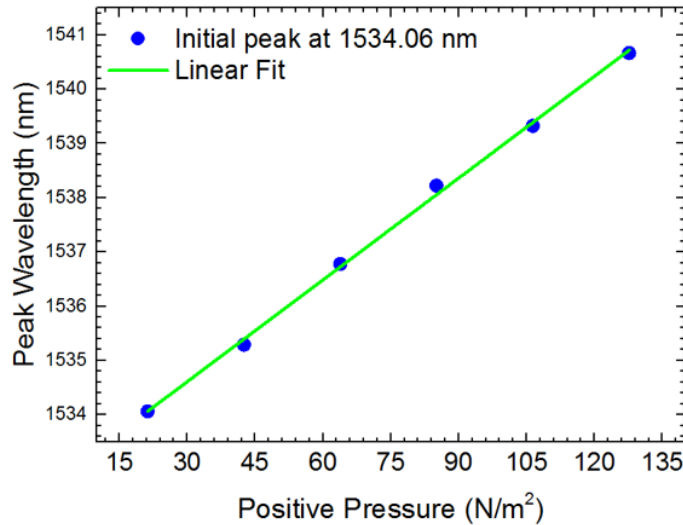


Figure 2-62 Shifts of the peak wavelengths with an initial value at 1534.06 nm in the transmission spectra of positive pressure sensing by the single-spiral waveguide sensor

Three more groups of peak wavelengths are identified from Fig. 2-62. The sensitivity of the shifts with the initial peak wavelengths at 1557.53 nm is 0.059 ± 0.002 nm/(N/m²), which is obtained by calculating the slope of the linear fit equation of the shift of the peak wavelengths as described in Fig. 2-64. The shifts of the peak wavelengths

with an initial peak wavelength of 1572.98 nm have a sensitivity of 0.056 ± 0.001 nm/(N/m²), which is obtained from the linear fit equation $y = Sx + I$ with the peak shifts, where $I = 1571.83 \pm 0.09$ nm. Within the range of 1586.22 to 1595.69 nm, a shift of peak wavelengths is identified, showing a sensitivity of 0.061 ± 0.004 nm/(N/m²). The values of sensitivities of single-spiral waveguide sensors varying from 0.056 to 0.061 nm/(N/m²).

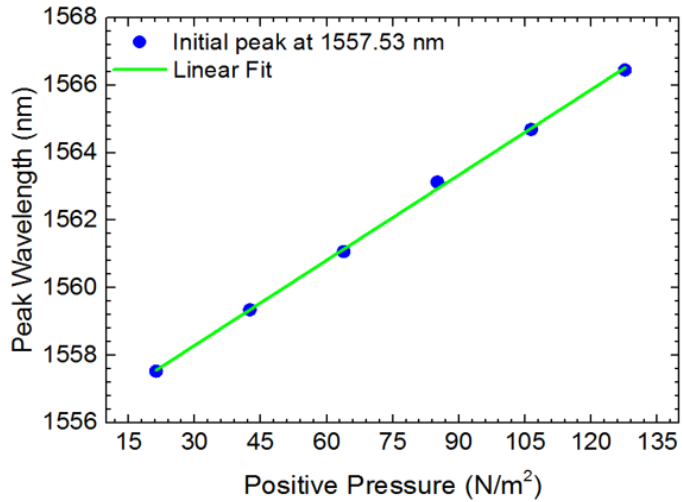


Figure 2-63 Shifts of the peak wavelengths with an initial value at 1557.53 nm in the transmission spectra of positive pressure sensing by the single-spiral waveguide sensor

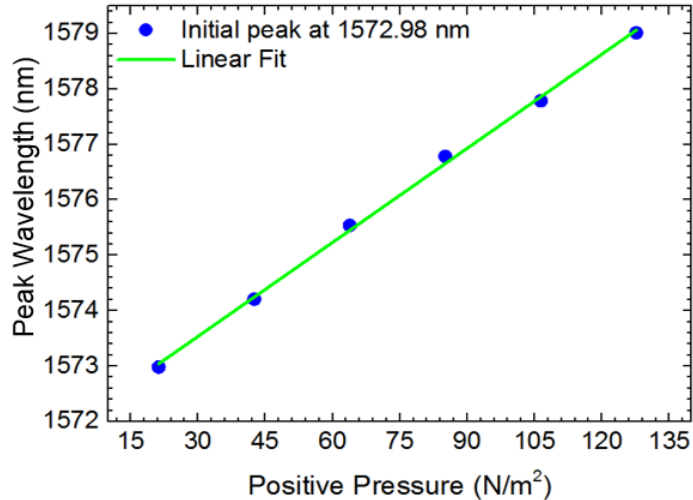


Figure 2-64 Shifts of the peak wavelengths with an initial value at 1572.98 nm in the transmission spectra of positive pressure sensing by the single-spiral waveguide sensor

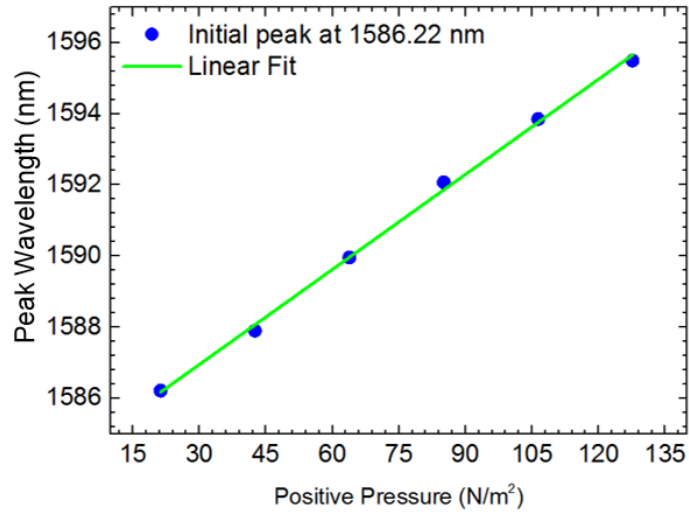


Figure 2-65 Shifts of the peak wavelengths with an initial value at 1586.22 nm in the transmission spectra of positive pressure sensing by the single-spiral waveguide sensor

Positive pressure sensing is then carried out by the double-spiral optofluidic sensor. By adding weights of 3.44, 3.65, 3.82 and 4.03 g onto the sensor chip, pressures of the values of 63.83, 85.11, 106.38, and 127.66 N/m² are applied on the sensor chip. The transmission spectra of the double-spiral sensor are obtained by OSA and the results are shown in Fig. 2-67. The positive pressure dependences of the individual peaks and valleys of the transmission spectra are described in Figs. 2-68, 2-69, and 2-70. A red shift is observed on the transmission spectra, which is caused by the increase of the effective refractive index of the sensing area generated by the added pressure on the sensor chip. For the purpose of calibration, shifts in valley wavelengths are identified from the transmission spectra (Fig. 2-67). The shifts with the initial valley wavelengths at 1529.23 nm is shown in Fig. 2-68. The sensitivity of this range of shift is 0.069 ± 0.001 nm/(N/m²), which is calculated by linear-fitting the equation $y = Sx + I$ with the valley shifts, where

$I = 1498.28 \pm 0.92$ nm is the intercept. It is observed that the sensitivity for positive pressure has increased, compared with the value of sensitivities of the single-spiral waveguide sensor.

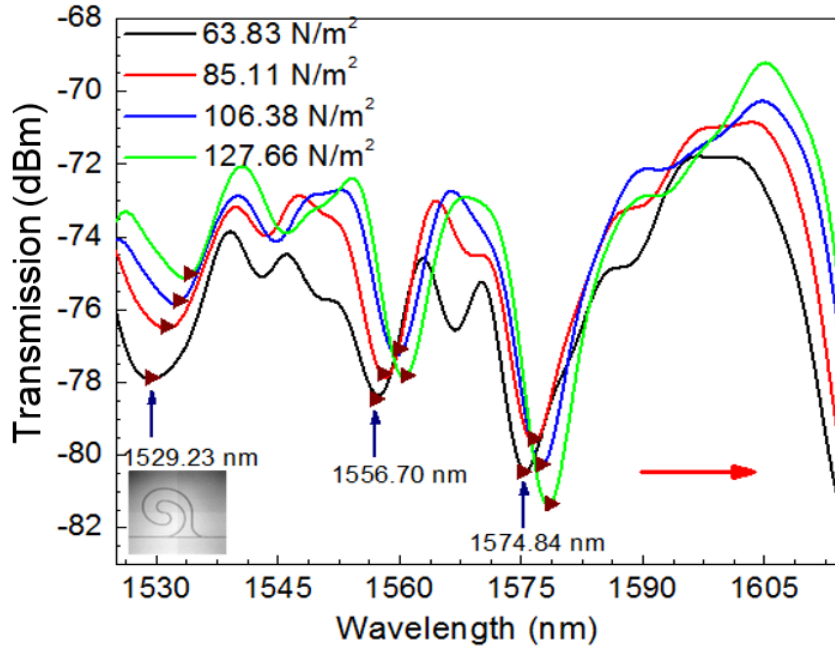


Figure 2-66 Positive pressure dependence of the transmission spectra of the double-spiral waveguide sensor

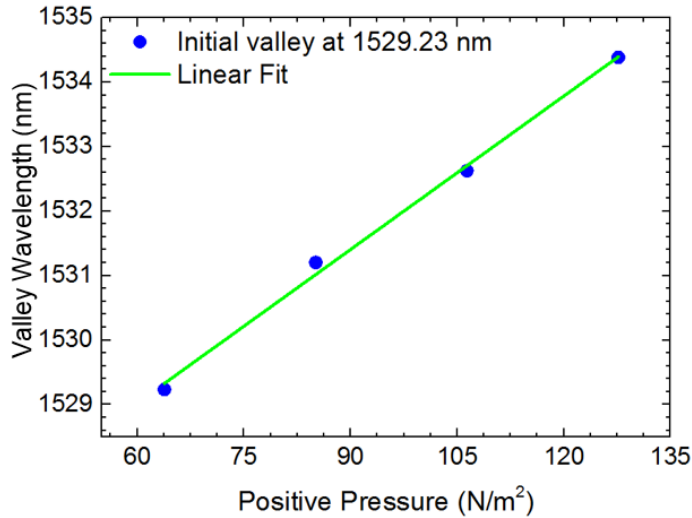


Figure 2-67 Shifts of the valley wavelengths with an initial value at 1529.23 nm in the transmission spectra of positive pressure sensing by the double-spiral waveguide sensor

Figures 2-69 and 2-70 describe wavelength shifts of two more valleys, which are from 1556.70 to 1561.00 nm, and from 1574.84 to 1579.18 nm, respectively. The sensitivity of the shifts with the initial valley wavelengths at 1556.70 nm is 0.071 ± 0.001 nm/(N/m²), while the shifts with the initial valley wavelengths at 1574.84 nm shows a sensitivity of 0.068 ± 0.003 nm/(N/m²), which are both read from the value of the slope of the linear fit of the valley shifts. A double-spiral waveguide sensor achieved sensitivities varying from 0.068 to 0.071 nm/(N/m²), which is higher than the sensitivities obtained by single-spiral waveguide sensors, which is 0.056 - 0.061 nm/(N/m²).

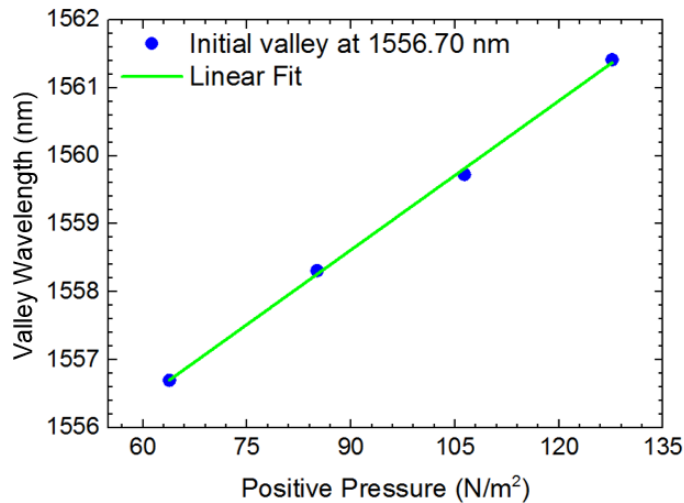


Figure 2-68 Shifts of the valley wavelengths with an initial value at 1556.70 nm in the transmission spectra of positive pressure sensing by the double-spiral waveguide sensor

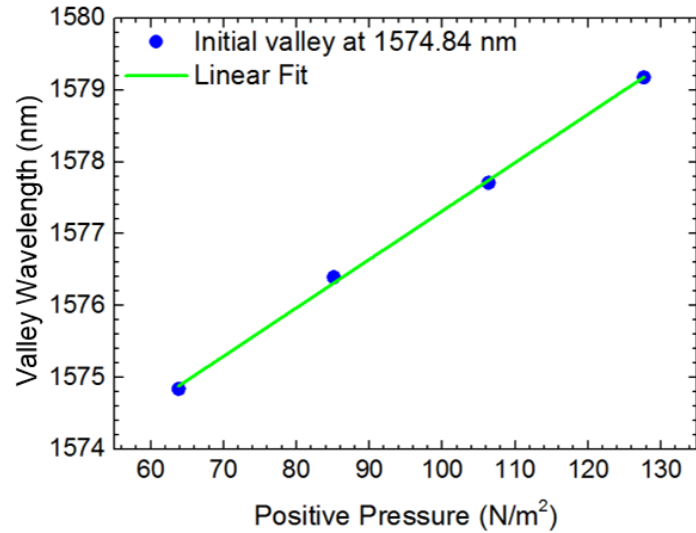


Figure 2-69 Shifts of the valley wavelengths with an initial value at 1574.84 nm in the transmission spectra of positive pressure sensing by the double-spiral waveguide sensor

Next, five positive pressures with values of 21.28, 42.55, 63.83, 85.11, and 106.38 N/m² are gradually applied on the triple-spiral sensor for positive pressure sensing. Figure 2-71 shows the transmission spectra of the triple-spiral waveguide sensor. The positive pressure dependences of the individual peaks of the transmission spectra are shown in Fig.2-72, 2-73, 2-74, 2-75, and 2-76. A red shift is observed on the transmission spectra, which is caused by the increase of the effective refractive index of the sensing area, a result of increasing pressure on the triple-spiral sensor chip.

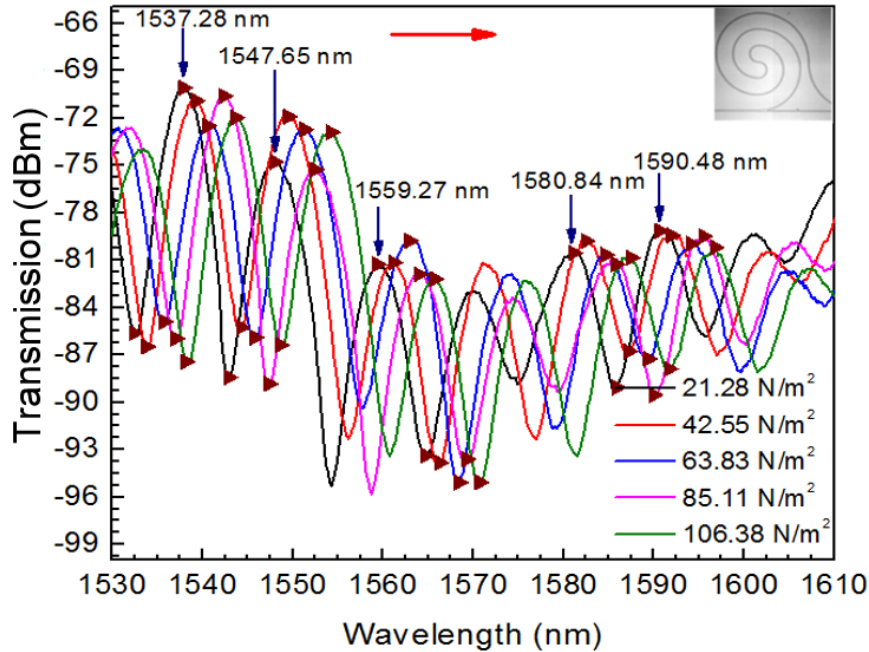


Figure 2-70 Positive pressure dependence of the transmission spectra of the triple-spiral waveguide sensor

Five groups of peak wavelengths are identified from the transmission spectra (Fig. 2-71) for calibration purpose. The shifts with an initial peak wavelength of 1537.28 nm is shown in Fig. 2-72, and has a sensitivity of 0.089 ± 0.003 nm/(N/m²). The sensitivity is calculated by linear fitting the equation $y = Sx + I$ with the peak shifts, where $I = 1535.76 \pm 0.01$ nm is the intercept. It is observed that 0.089 nm/(N/m²) is the highest sensitivity obtained so far and it is achieved by the triple-spiral waveguide sensor. Figures 2-73 and 2-74 describe two more shifts with initial peak wavelengths at 1547.65 nm and 1559.27 nm, respectively. The sensitivity of the shifts starting at 1547.65 nm is 0.081 ± 0.003 nm/ (N/m²), while the shifts starting at 1559.27 nm has a sensitivity of 0.077 ± 0.002 nm/ (N/m²); both sensitivities are read from the value of the slope of the

linear fit of the peak shifts. The linear fit equation has the form of $y = Sx + I$. The intercepts for the shifts of 1547.65 - 1554.58 nm is 1545.94 ± 0.14 nm, while for the shifts of 1559.27 - 1565.85 nm is 1557.78 ± 0.24 nm.

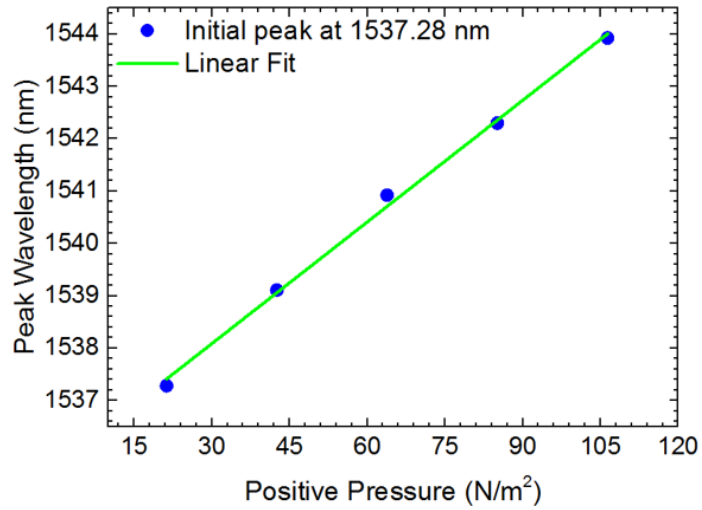


Figure 2-71 Shifts of the peak wavelengths with an initial value at 1537.28 nm in the transmission spectra of positive pressure sensing by the triple-spiral waveguide sensor

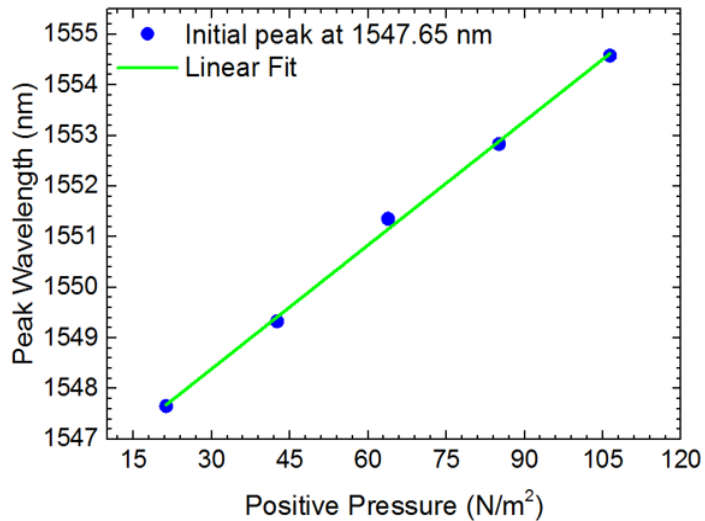


Figure 2-72 Shifts of the peak wavelengths with an initial value at 1547.65 nm in the transmission spectra of positive pressure sensing by the triple-spiral waveguide sensor

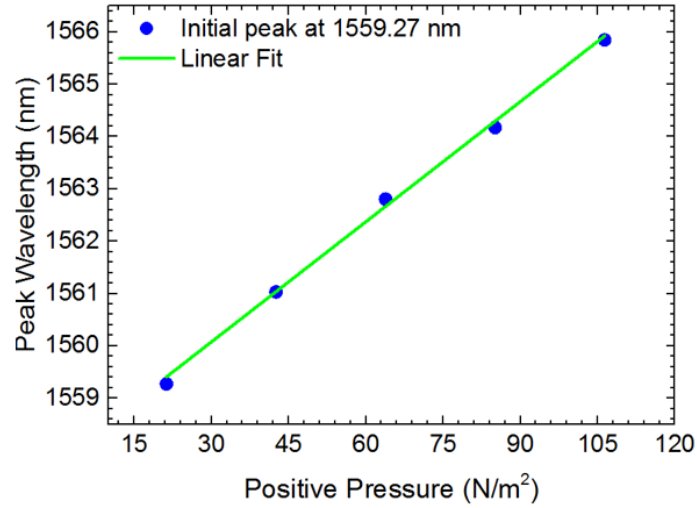


Figure 2-73 Shifts of the peak wavelengths with an initial value at 1559.27 nm in the transmission spectra of positive pressure sensing by the triple-spiral waveguide sensor

From the transmission spectra in Fig. 2-71, two more groups of peak wavelengths shifting towards the longer wavelength are identified and shown in Figs. 2-75 and 2-76. The sensitivity of the shifts with the initial valley wavelength at 1580.84 nm is 0.085 ± 0.04 nm/(N/m²), while the shifts with the initial valley wavelength at 1590.48 nm has a sensitivity of 0.080 ± 0.01 nm/(N/m²). The triple-spiral waveguide sensor obtains sensitivities varying from 0.077 and 0.089 nm/(N/m²), which is higher than the sensitivities obtained by the single-spiral waveguide sensor, which is 0.056 - 0.061 nm/(N/m²), and the sensitivity obtained by the double-spiral waveguide sensor, which is 0.068 to 0.071 nm/(N/m²).

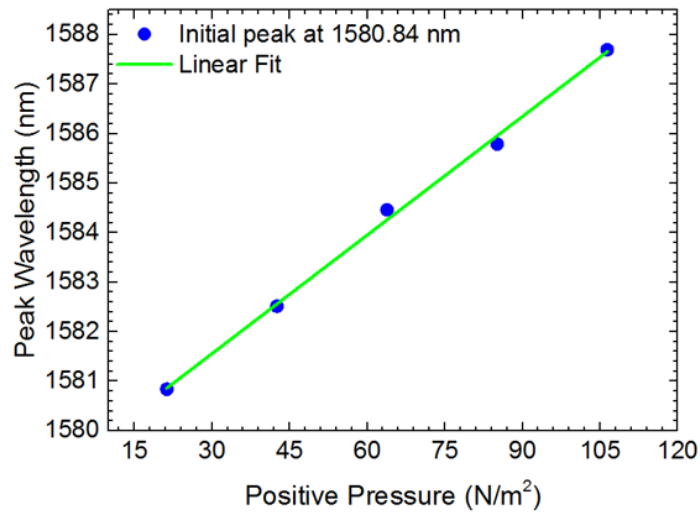


Figure 2-74 Shifts of the peak wavelengths with an initial value at 1580.84 nm in the transmission spectra of positive pressure sensing by the triple-spiral waveguide sensor

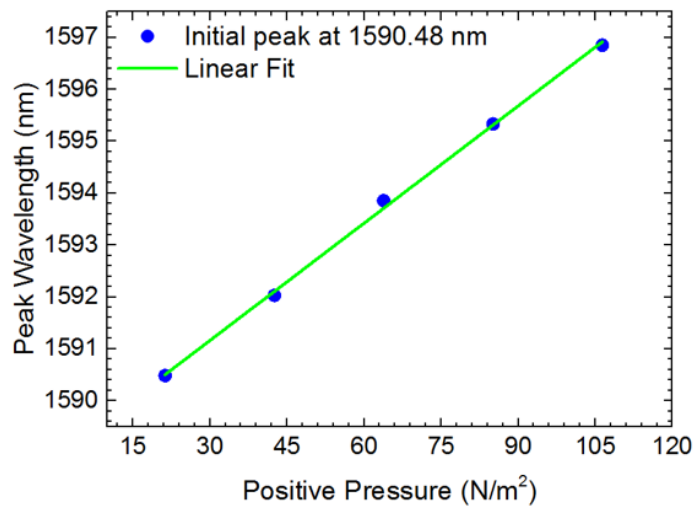


Figure 2-75 Shifts of the peak wavelengths with an initial value at 1590.48 nm in the transmission spectra of positive pressure sensing by the triple-spiral waveguide sensor

The quadruple-spiral waveguide sensor is carried out by stacking weights of 1.309, 2.431, 3.568, and 4.518 g on the sensor chip, which gives the chip five different pressures: 21.38, 42.55, 63.83, and 85.11 N/m². Figure 2-77 shows the transmission spectra of the

quadruple-spiral waveguide sensor with the five pressure values. The positive pressure dependences of the individual peaks and valleys of the transmission spectra are shown in Fig. 2-78, 2-79, and 2-80. A red shift is observed on the transmission spectra, which is caused by the increase of effective refractive index of the sensing area that results after increasing the pressure added on the triple-spiral sensor chip.

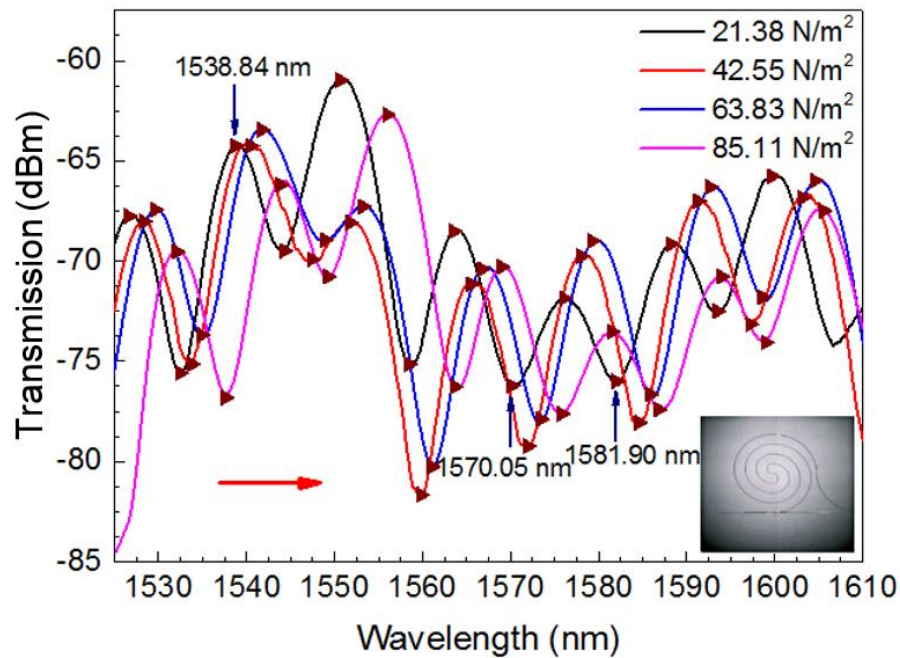


Figure 2-76 Positive pressure dependence of the transmission spectra of the quadruple-spiral waveguide sensor

In order to obtain the sensitivities of the quadruple-spiral waveguide sensor for calibration of further measurements of positive pressure, three shifts of peaks and valleys are identified and calculated from the transmission spectra in Fig. 2-77 and shown in Figs. 2-78, 2-79, and 2-80. The shifts with an initial peak wavelength at 1538.84 nm are first

read from Fig. 2-77, with a sensitivity of 0.060 ± 0.003 nm/ RIU, which is lower than the sensitivities obtained by the triple-spiral waveguide sensor.

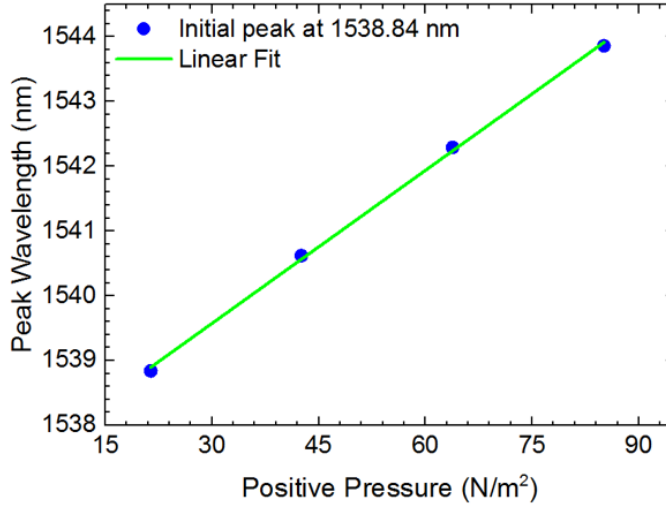


Figure 2-77 Shifts of the peak wavelengths with an initial value at 1538.84 nm in the transmission spectra of positive pressure sensing by the quadruple-spiral waveguide sensor

Figures 2-79 and 2-80 describe two more shifts of valley wavelengths with initial valley wavelengths at 1570.05 nm and 1581.90 nm, respectively. The sensitivity of the shifts starting at 1570.05 nm is 0.058 ± 0.002 nm/(N/m²), while the shifts starting at 1581.90 nm have a sensitivity of 0.056 ± 0.001 nm/(N/m²). Both sensitivity values are obtained from the value of the slope of the linear fit of the valley shifts. The linear fit equation has the form of $y = Sx + I$. The intercepts for the shifts from 1570.05 to 1575.49 nm is 1568.30 ± 0.10 nm, while for the shifts from 1581.90 to 1587.29 nm, the sensitivity is 1580.14 ± 0.18 nm. It can be observed on Figs. 2-78, 2-79, and 2-80 that the sensitivities of the quadruple-spiral waveguide sensor are varying from 0.058 to 0.060

nm/(N/m²). This means that the highest sensitivities are from 0.077 to 0.089 nm/(N/m²), which is obtained by the triple-spiral waveguide sensor.

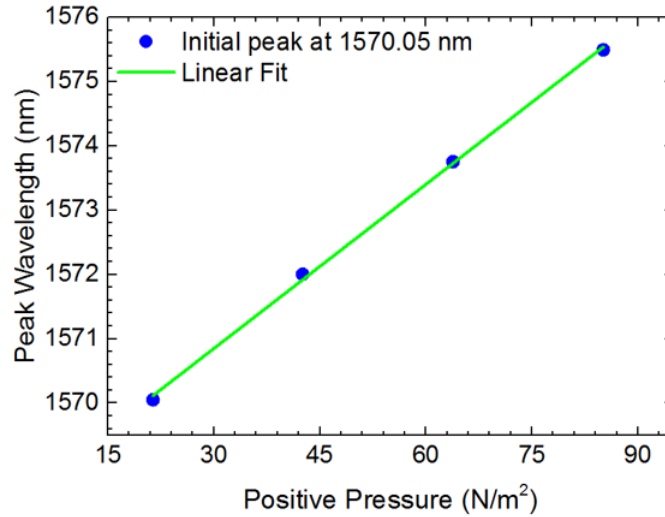


Figure 2-78 Shifts of the peak wavelengths with an initial value at 1570.05 nm in the transmission spectra of positive pressure sensing by the quadruple-spiral waveguide sensor

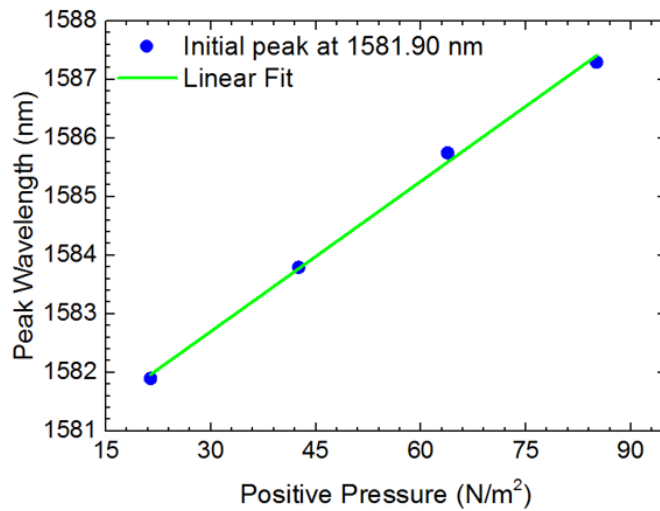


Figure 2-79 Shifts of the peak wavelengths with an initial value at 1581.90 nm in the transmission spectra of positive pressure sensing by the quadruple-spiral waveguide sensor

2.6 Comparison of the sensing performance of spiral waveguide sensors

Figures 2-81, 2-82 and 2-83 show the comparisons of the sensitivities of single-spiral, double-spiral, triple-spiral, and quadruple-spiral optofluidic waveguide sensors. Sensitivities of the four spiral waveguide sensors for temperature sensing are compared in Fig. 2-81, indicating that the highest sensitivities are achieved by the triple-spiral waveguide sensor. This is due to spiral waveguide sensor is designed based on MZI, of which the sensitivity is related to the change of the optical path difference, as illustrated in Eq. 2.3. However, the highest sensitivity is not achieved by the quadruple-spiral waveguide sensor, which has the longest optical path difference. This is due to the fact that a change in effective refractive index also influences the sensing performance of the spiral waveguide sensors. During the fabrication of the quadruple-spiral waveguide sensor, a much larger evenly coated area is required as the quadruple-spiral waveguide occupies an area of $180864 \mu\text{m}^2$, while the triple-spiral waveguide requires only $45216 \mu\text{m}^2$. Otherwise, the height of the spiral curves of the quadruple-spiral waveguide could be different if the SU-8-2 film is subtly and not evenly coated. Moreover, the motion stage takes a short reflection time while changing directions during fabrication. Due to the time that the motion stage needs to overcome its inertia, all the points on the waveguide that are fabricated while the motion stage is changing direction will have slightly greater exposure. As a result, the greater the change of direction, the less smooth the waveguide turns out to be. Furthermore, quadruple-spiral waveguide sensor has the highest transmission loss among all the four waveguide sensors. All the reasons stated above can cause irregular propagation modes of the transmission light, which affects the increase of

effective refractive index during the sensing experiments. There are much fewer irregular propagation modes in single-spiral, double-spiral and triple-spiral waveguide sensors, which make the optical path difference the dominant factor in the change in sensitivity. However, in the quadruple-spiral waveguide sensor, the irregular propagation modes become the dominant factor to influence the sensitivity, which result in the decrease in sensitivity compared to the triple-spiral waveguide sensor.

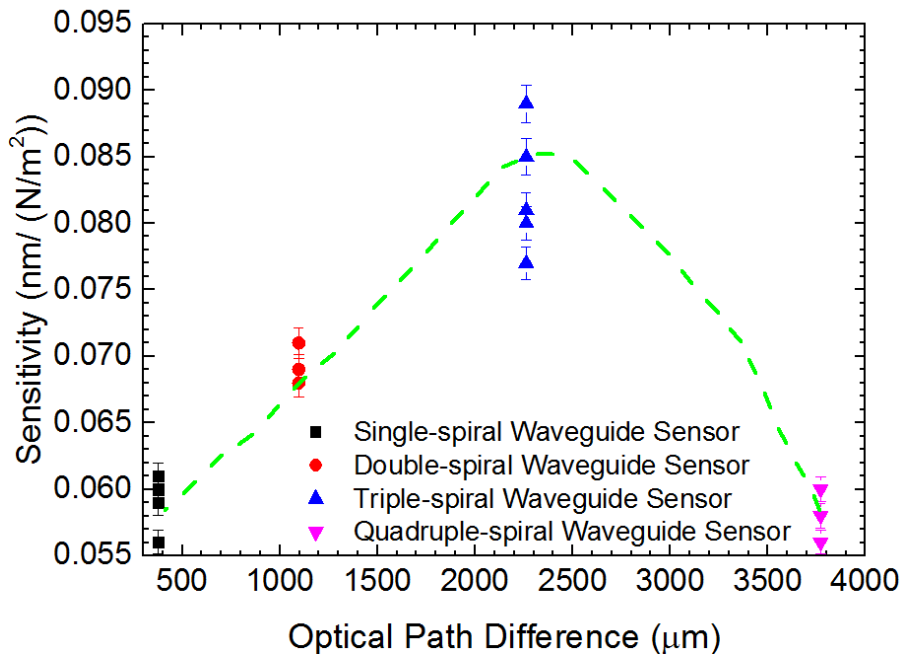


Figure 2-80 Comparison on temperature sensitivities of the four spiral waveguide sensors

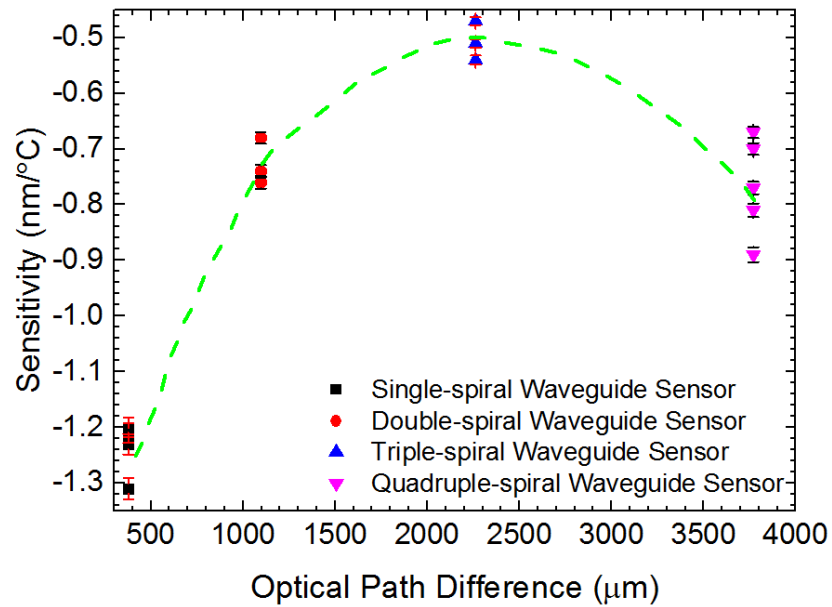


Figure 2-81 Comparison on RI sensitivities of the four spiral-shaped waveguide sensors

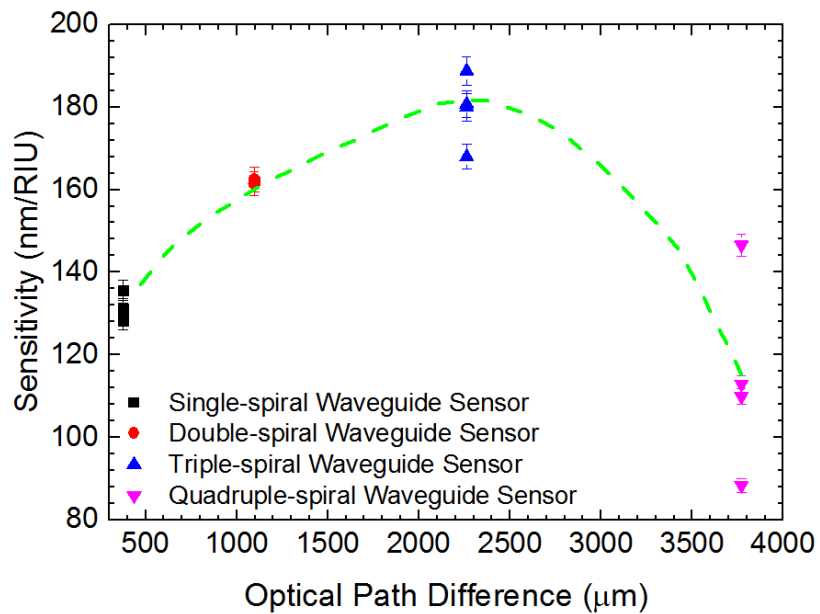


Figure 2-82 Comparison on positive pressure sensitivities of the four spiral waveguide sensors

2.7 Conclusion

In this chapter, spiral-shaped optofluidic waveguide sensors are investigated for their capability to sense changes of different environmental parameters (temperature, refractive index, and positive pressure). For all three sets of sensing experiments (temperature, refractive index, and positive pressure), the highest sensitivities are all achieved by the triple-spiral waveguide sensor. In addition, the triple-spiral waveguide sensor also has steady transmission spectra with good interference pattern, which makes it the most suitable candidate among the four for further sensing of positive pressure.

Chapter 3 Spiral Optofluidic Sensors for Bio-sensing Applications

In this chapter, the triple-spiral optofluidic waveguide sensor is applied to the study of the refractive indices among dairy and dairy-like products. In addition, the waveguide sensors are used to sense the saccharinity in sucrose solutions. The changes in optical properties of dairy products during the aging process are studied based on the shifts of their transmission spectra.

3.1 Refractive indices of cow milk products

Cow milk and related milk products have been essential elements in humans' diets for thousands of years [161]. Long regarded as an excellent source of proteins, vitamins, calcium and various minerals, cow milk is a part of important foods for millions of people [162]. The vast majority of the studies so far have focused on understanding the properties of milk and the interaction between milk and the human body [155–158]. However, the relationship between the composition and the physical/chemical properties of cow milk and related products has not been well understood. Optical technology can be a helpful tool to understand how the observed optical properties (such as RI) relate with the change in the composition of milk and related products. For any solution, refractive index is one of the most important parameters. Therefore, in this study, the refractive index of cow milk is characterized with the triple-spiral optofluidic waveguide sensor, as

it achieves the highest sensitivity among all four spiral waveguide sensors (Section 2.6). The cow milk samples were collected from grocery stores in St John's, NL and stored in the refrigerator throughout the entire testing process. Figure 3-1 shows some of the commercially available dairy products (in cans, in bottles and in carton containers) and dairy-like products found in grocery stores in St. John's.



Figure 3-1 A series of dairy and non-dairy products which are available in local stores in St. John's

Three commercially available brands of pasteurized milk are used as samples for testing in this study. Milk with different fat percentages (0, 0.5, 1, 2 and 3.25%) of Brand S and Brand C are tested with the triple-spiral waveguide sensor. Figure 3-2 shows the

peak shift of the transmission spectra of the five milk samples of Brand S. The refractive index of commercial milk is related with the large particles suspended in the milk body such as fat globules and casein-calcium phosphates [166]. Milk contains 87.5 % of water, while the rest of it is composed by fat, proteins, lactose, vitamins and minerals [166]. The light transmitted inside the milk refracts when encountering large molecules with different densities, such as fat globules. As observed in Fig. 3-2, a red shift occurs as the fat content in milk increases, which is caused by the slight increase in RIs of the tested milk samples. Figure 3-3 (a), (b), (c), (d), and (e) represent five peak shifts and (f) is a comparison on the shifts in the peak wavelengths of the five identified transmission peaks.

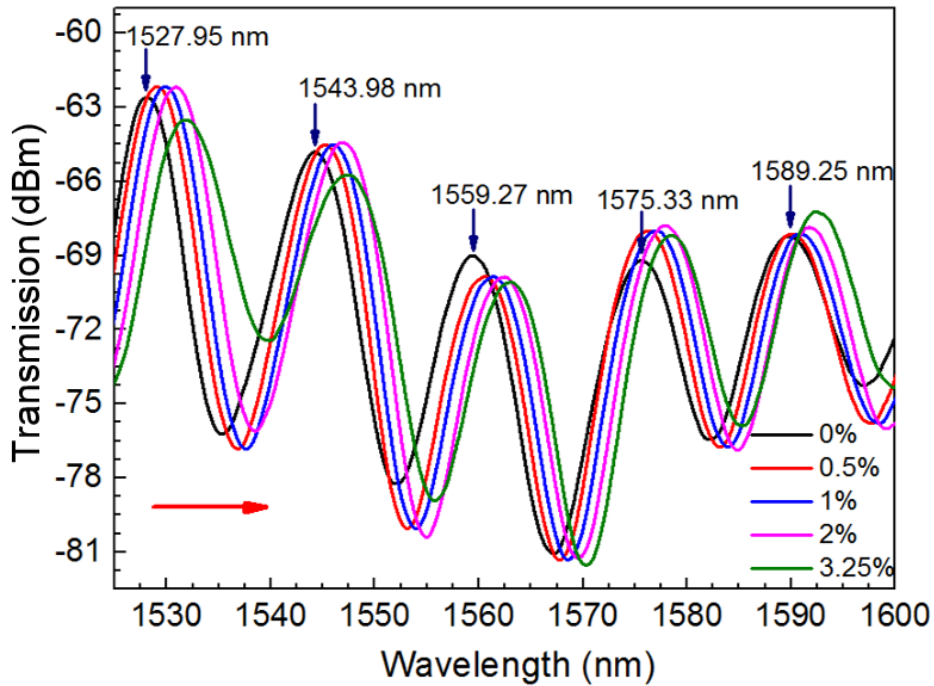


Figure 3-2 Transmission spectra of five milk samples of Brand S with different fat percentages indicated inside the figure.

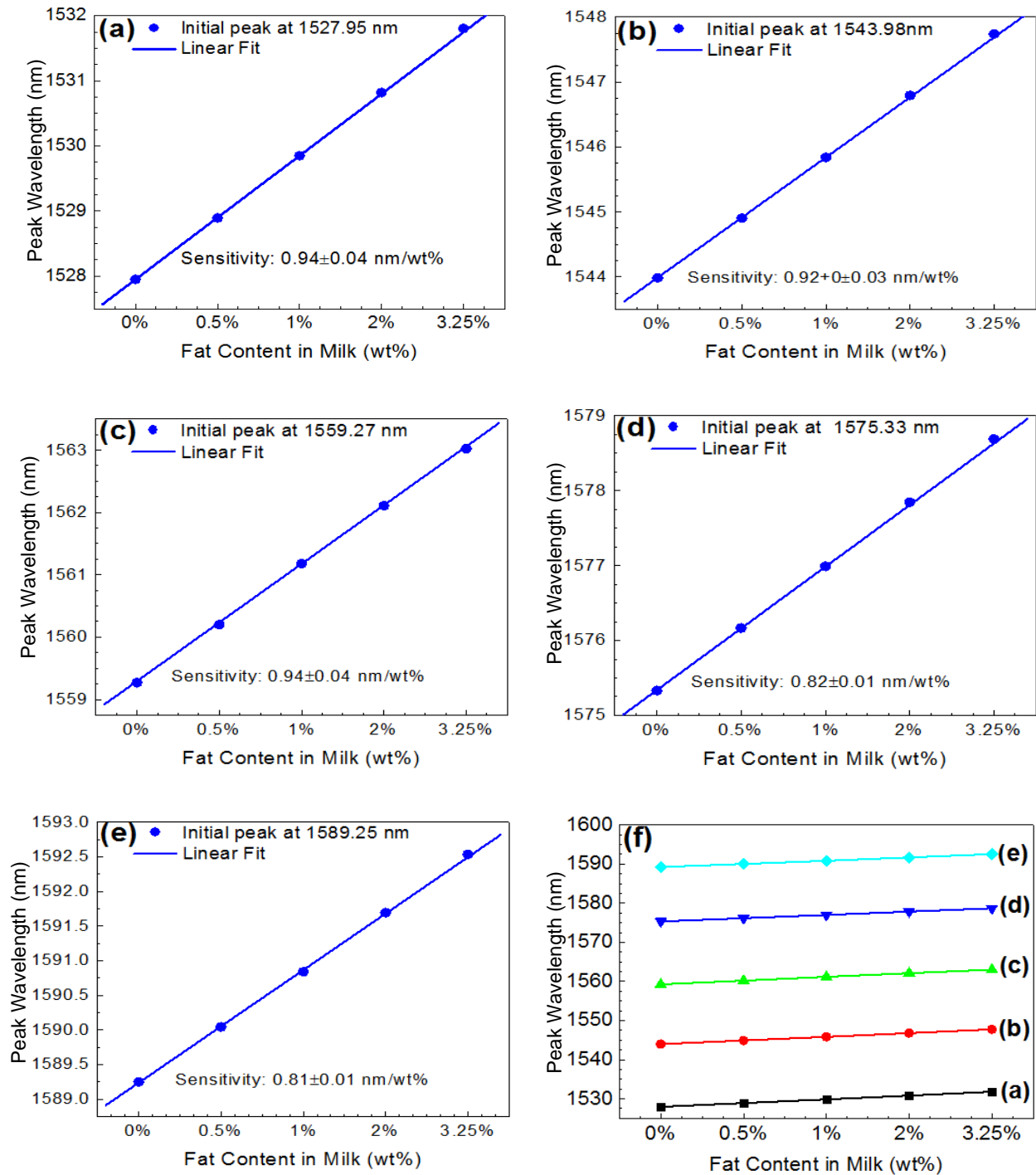


Figure 3-3 (a) – (e) shifts in the peak wavelengths of the triple-spiral waveguide sensor on testing five milk samples (0%, 0.5%, 1%, 2%, and 3.25%) of Brand S; (f) comparison on the results from these five milk samples.

The observed shifts in the peak wavelengths of RI sensing as shown on Fig. 3-3 can be fit with a linear equation:

$$y = Sx + I \quad (3.1)$$

where S is the slope which represents the sensitivity and I represents the intercept. The sensitivities of the RI of Brand S cow milk of the triple-spiral sensor is obtained by calculating the slope S of Eq. 3.1, as shown in Fig. 3-3. The uncertainty in the values of the refractive index originates from two sources as shown in the following equation:

$$x = \frac{y - I}{S} \quad (3.2)$$

The first possible source of uncertainty is from S (Slope), and the other is from I (Intercept). The uncertainty calculation follows the equation

$$\frac{\delta x}{x} = \frac{\delta(y - I)}{y - I} - \frac{\delta S}{S} \quad (3.3)$$

The results of the refractive index sensing are calculated and given in the following table:

Table 3-1 RI sensing of the milk samples from Brand S

Milk Fat Percentage	Refractive Index
0%	1.347±0.002
0.5%	1.352±0.003
1%	1.357±0.002
2%	1.362±0.002
3.25%	1.369±0.001

Figure 3-4 displays the peak shift of the transmission spectra of the five milk samples (0, 0.5, 1, 2 and 3.25%) of Brand C. As observed in Fig. 3-4, a shift in the transmission spectra towards longer wavelengths occurs with the increase of fat content in milk. The red shift is caused by the slight increase in refractive indices of the tested milk samples. Figure 3-5 (a), (b), (c), (d), and (e) represent five peak shifts, and (f) is a comparison of the shifts in the peak wavelengths of the five identified transmission peaks.

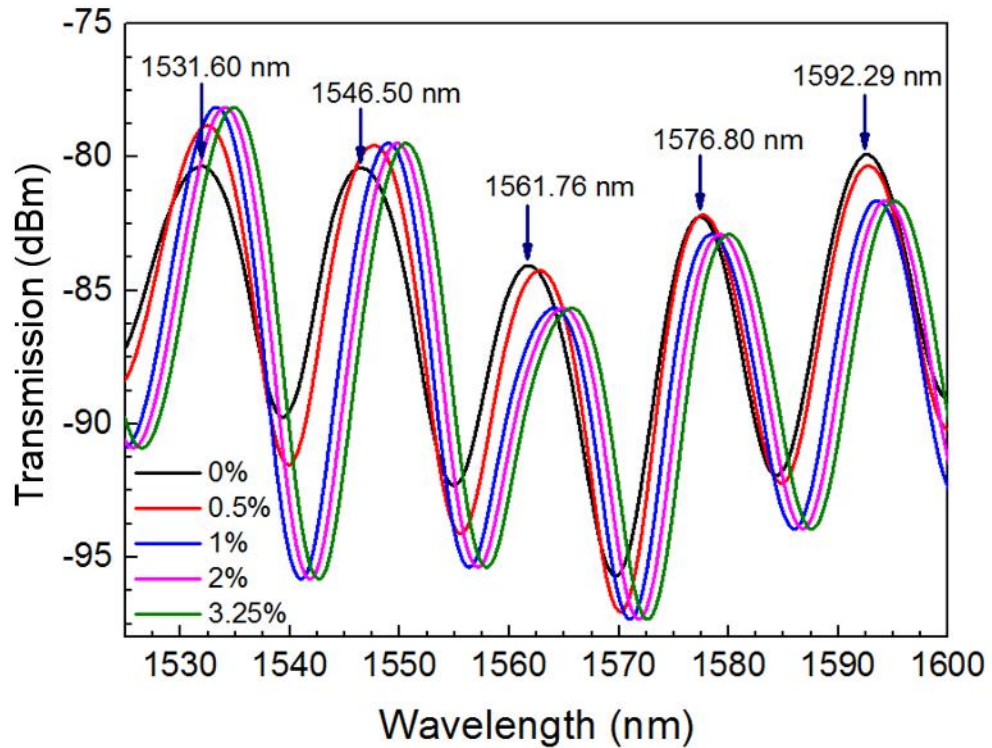


Figure 3-4 Transmission spectra of five milk samples of Brand C with different fat percentages indicated inside the figure.

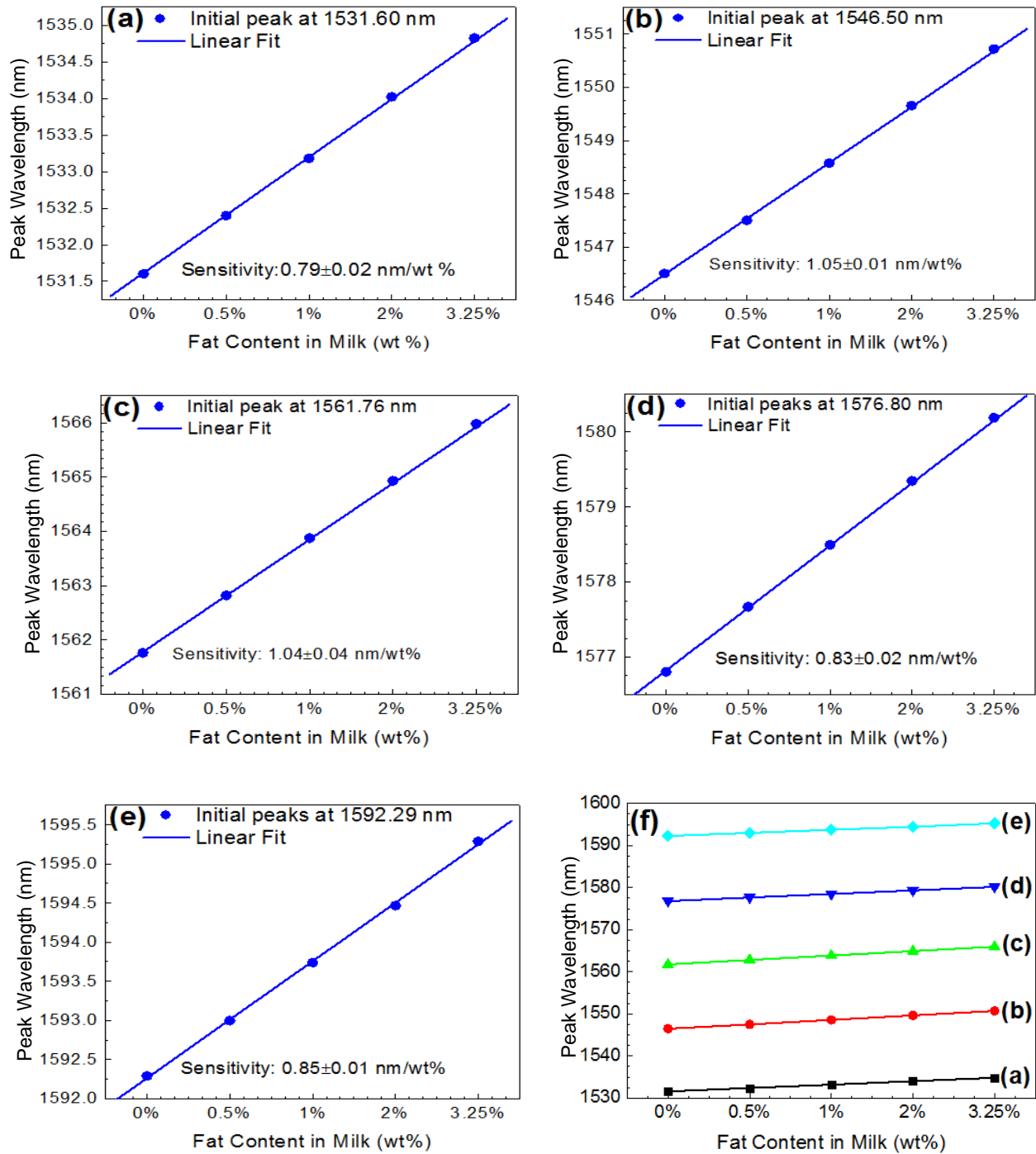


Figure 3-5 (a) – (e) shifts in the peak wavelengths of the triple-spiral waveguide sensor on testing five milk samples (0%, 0.5%, 1%, 2%, and 3.25%) of Brand C; (f) comparison on the results from these five milk samples.

The refractive index sensing result are calculated in the following table:

Table 3-2 RI sensing of the milk samples from Brand C

Milk Fat Percentage	Refractive Index
0%	1.362±0.001
0.5%	1.366±0.001
1%	1.371±0.003
2%	1.375±0.001
3.25%	1.379±0.001

To summarize, the triple-spiral waveguide sensor is infused with five samples of cow milk of different fat contents (0%, 0.5%, 1%, 2%, and 3.25%) from two brands (Brand S and Brand C). The range of refractive indices of the milk samples of the Brand S is 1.347 - 1.369, while the milk samples from Brand C ranges from 1.362 to 1.379. The results of the RI sensing show that the refractive index of cow milk increases with the increase of the percentage of fat globules. However, cow milk is a complex aqueous-based colloidal solution [166], whose physical properties, such as RI, do not only depend on milk's intrinsic composition factors, but also depend on extrinsic factors such as the raising condition of cows and the post-milking treatment [167]. There are differences in the RIs of cow milk samples shown in Figs. 3-2 and 3-4. In the experiments shown in the section 3.2, the transmission spectra of cow milk samples from the same brands (Brand S and Brand C) but from different batches are tested in comparison with other milk-like samples. There is no significant difference in transmission spectra of the milk sample

from the same brand but different batches. However, the samples of cow milk are obtained from two different producers, which may support different conditions in which milk cows are raised and may perform different protocols for the treatment of milk before sending it to the market. It is understandable, that the ranges of refractive indices of the cow milk samples from two different producers may vary slightly.

3.2. Refractive indices of milk and milk-like products

The quality of milk and milk-like products can be assessed by investigating their physical properties, such as refractive index. Therefore, milk-like products, including original unsweetened coconut milk, original unsweetened almond milk and 1:1 blend of almond milk and coconut milk, along with 1% organic milk, 2% lactose free Milk, and fresh raw milk are tested with the triple-spiral waveguide sensor and the sensing results are compared with each other.

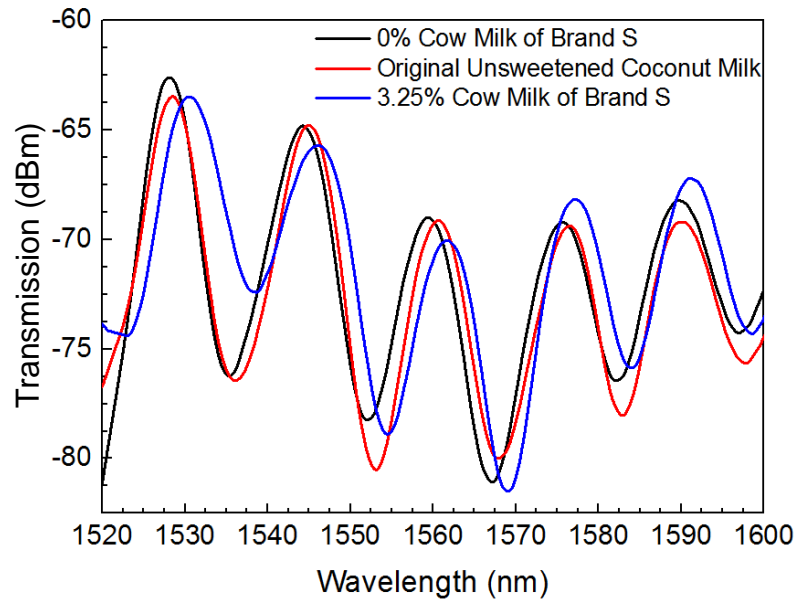


Figure 3-6 Transmission spectra of the original unsweetened coconut milk compared with that of the 0% and 3.25% milk of Brand S

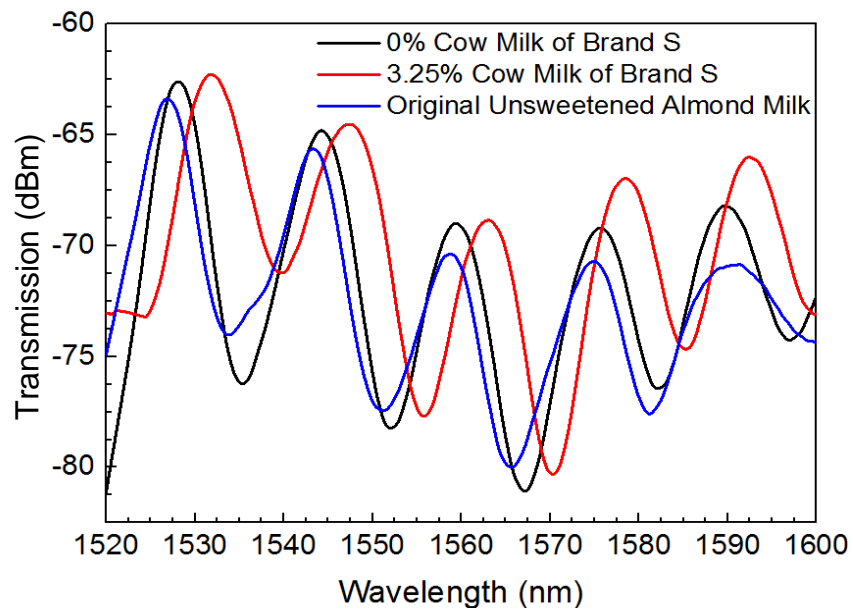


Figure 3-7 Transmission spectra of the original unsweetened almond milk compared with that of the 0% and 3.25% milk of Brand S

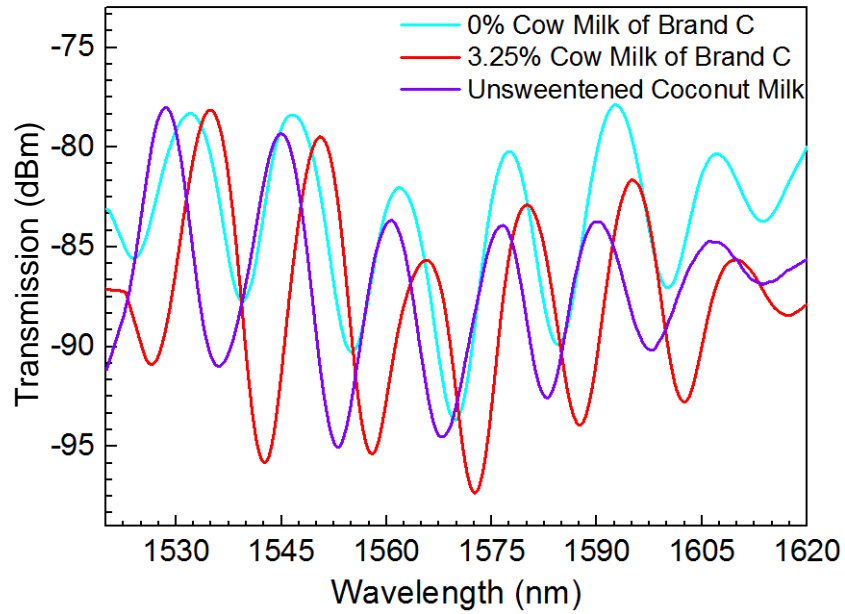


Figure 3-8 Transmission spectra of the original unsweetened coconut milk compared with that of the 0% and 3.25% milk of Brand C

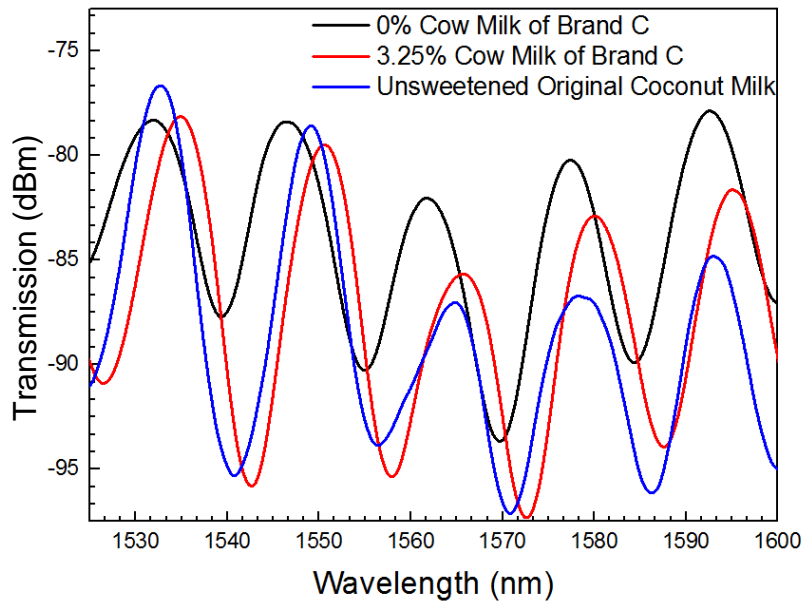


Figure 3-9 Transmission spectra of the original unsweetened almond milk compared with that of the 0% and 3.25% milk of Brand C

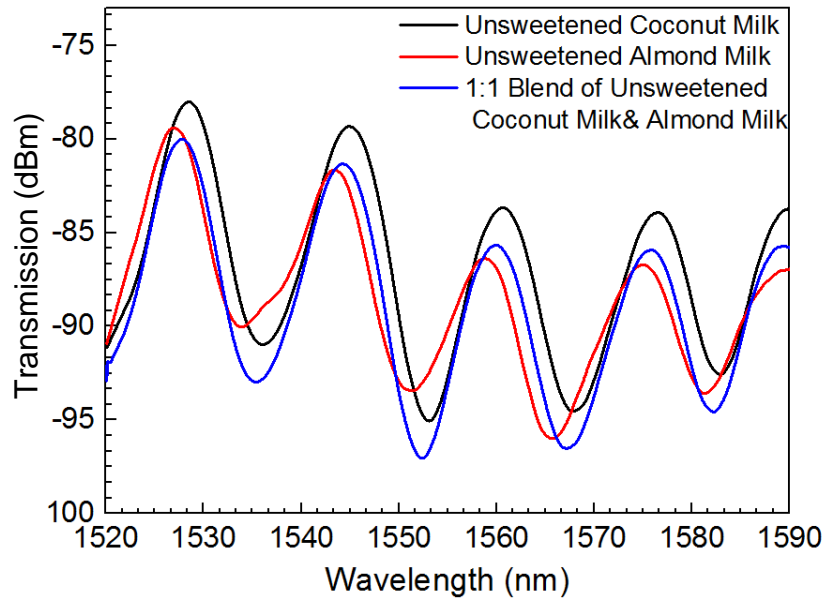


Figure 3-10 Transmission spectra of the original unsweetened almond and coconut 1:1 blend compared with that of the unsweetened coconut milk and unsweetened almond milk

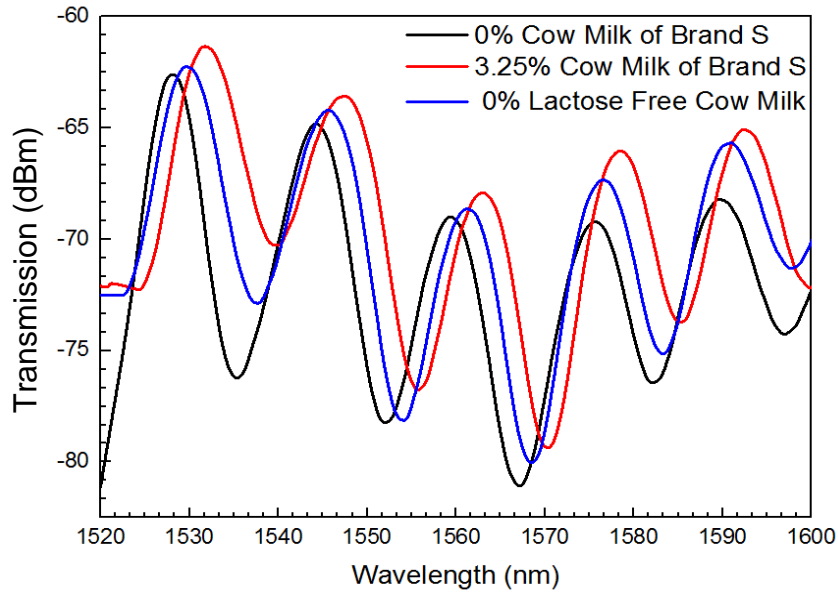


Figure 3-11 Transmission spectra of Brand L lactose free milk compared with that of the 0% and 3.25% milk of Brand S

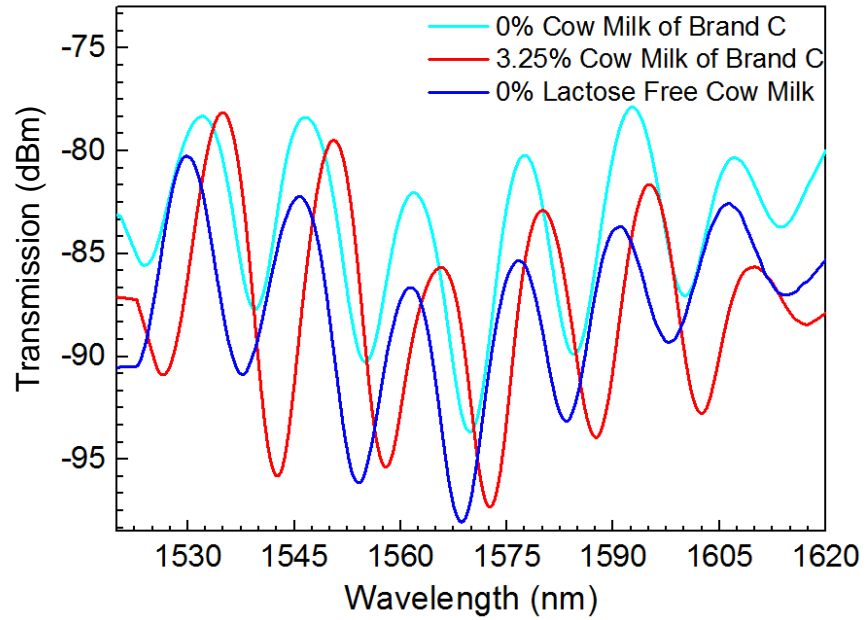


Figure 3-12 Transmission spectra of Brand L lactose free milk compared with that of the 0% and 3.25% milk of Brand C

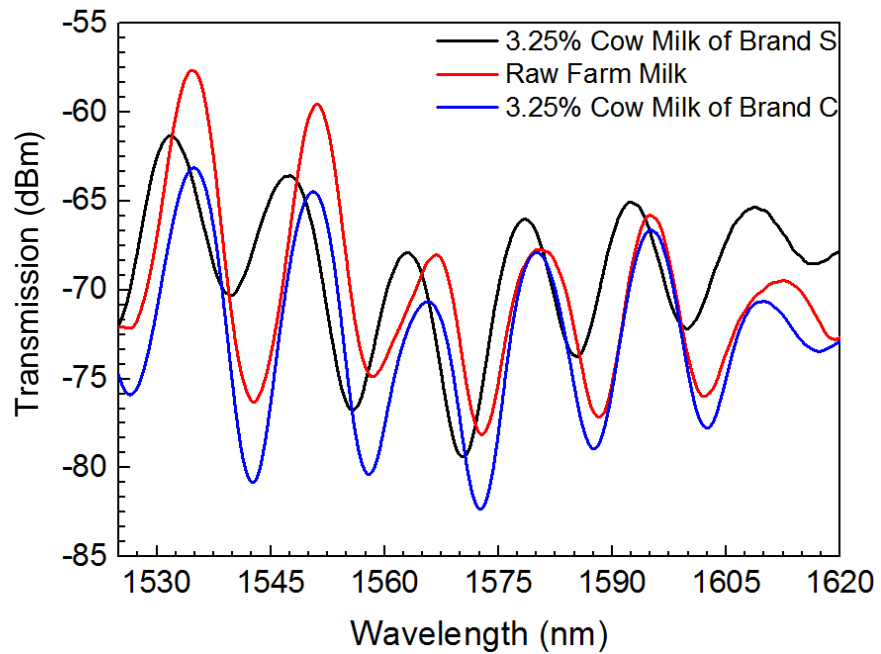


Figure 3-13 Transmission spectra of raw farm milk compared with that of the 3.25% milk of Brand S and Brand C

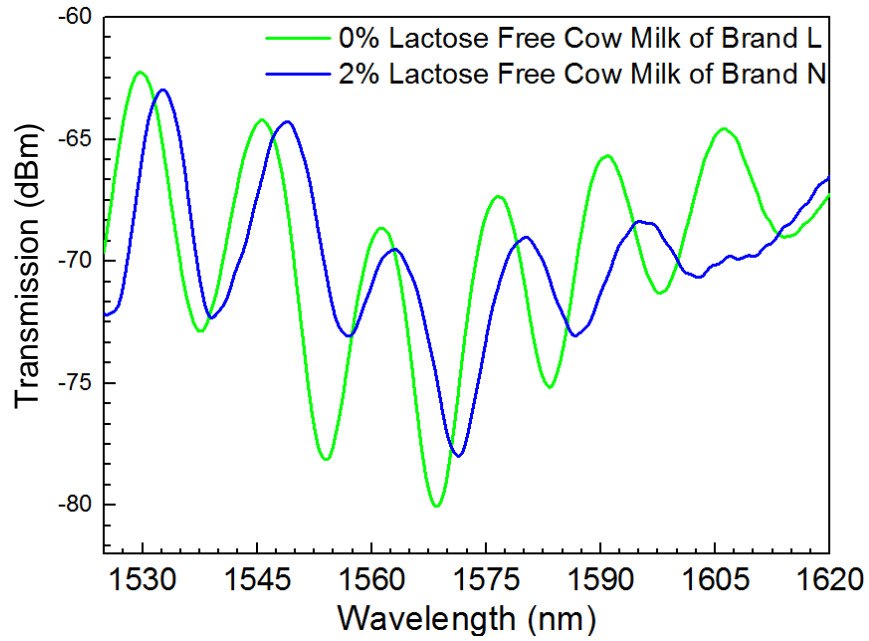


Figure 3-14 Transmission spectra of the 0% lactose free milk from Brand L compared with that of the 2% lactose free milk from Brand N

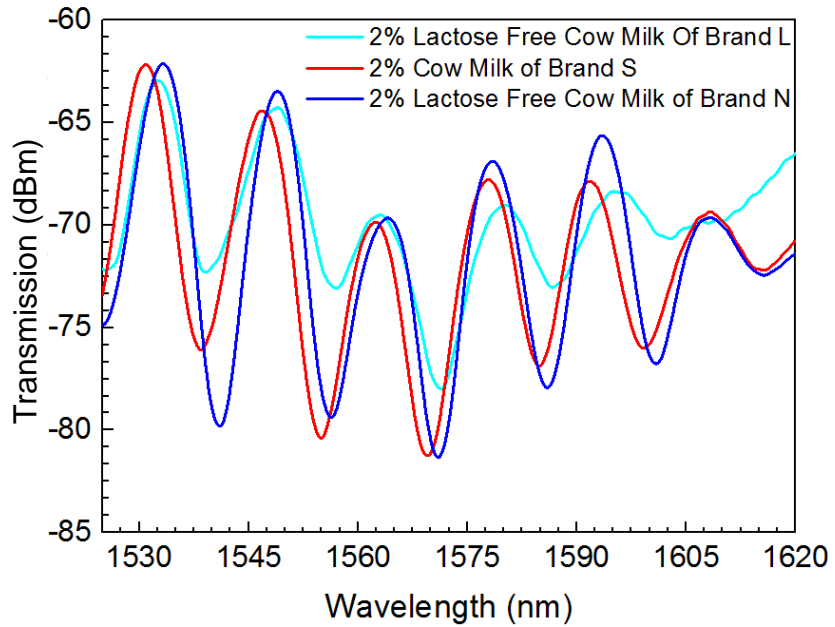


Figure 3-15 Transmission spectra of the 2% lactose free milk from Brand L and N compared with that of the 2% milk from Brand S

Table 3-3 RI sensing of the milk and milk-like products

Milk and Milk-like Products	Refractive Index (RIU)
Almond Milk	1.349±0.004
Coconut Milk	1.357±0.007
1:1 Blend of Almond Milk& Coconut Milk	1.354±0.008
Brand L Fat Free Lactose Free Cow Milk	1.360±0.008
Brand N 1% Organic Cow Milk	1.363±0.003
Brand N 2% Lactose Free Cow Milk	1.371±0.004
Raw Cow Milk	1.381±0.003

It can be seen from the first two rows in Table 3-3 that the RI of unsweetened coconut milk is 1.357, which is larger than that of unsweetened almond milk. As the main large particle contained in both almond milk and coconut milk, 8 oz. (1 cup) of coconut milk contains 5g of fat, the same amount of almond milk contains only 3g of fat (for a detailed list of nutrition facts for both, see [168]). The 1:1 blend of almond and coconut milk has a RI value of 1.354, which is in between the refractive indices of almond and coconut milk. The RI of 2% lactose free cow milk of Brand N is 1.371, which is higher than that of its fat free counterpart.

Organic milk is available in most local grocery stores and the price is nearly triple the price of non-organic milks. In contrast to non-organic milk, organic milk is produced by cows that are fed with pesticide-free grain and grass [169]. In order to find out the

difference in the optical properties between non-organic milk and organic milk, Brand N 1% organic milk is tested with the triple-spiral optofluidic sensor chip and the sensing result is shown in Fig. 3-16. The transmission spectrum of the Brand N organic cow milk is compared with the Brand S 1% non-organic cow milk and the Brand C 1% non-organic cow milk. As shown in Table 3-3, the RI of organic milk is 1.363 which is close to the RIs of its non-organic counterparts. The refractive index of a solution depends on the refractive index of the solvent and the particles in the solution. The small refractive index difference between organic and non-organic milk indicates that there is not a significant difference in their compositions at the microscopic level. Next, canned skim evaporated milk is tested with the triple-spiral waveguide sensor. The transmission spectrum of the canned skim evaporated milk is compared with 0% and 3.25% milk samples from both Brand S and Brand C, as shown in Fig. 3-18.

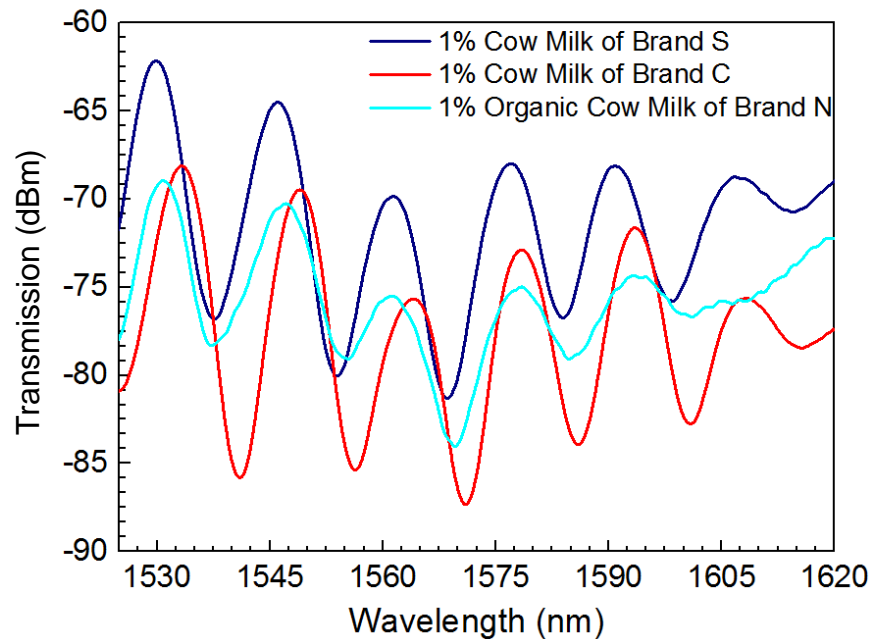


Figure 3-16 Transmission spectra of the 1% organic cow milk of Brand N and its non-organic counterparts by a triple-spiral waveguide sensor

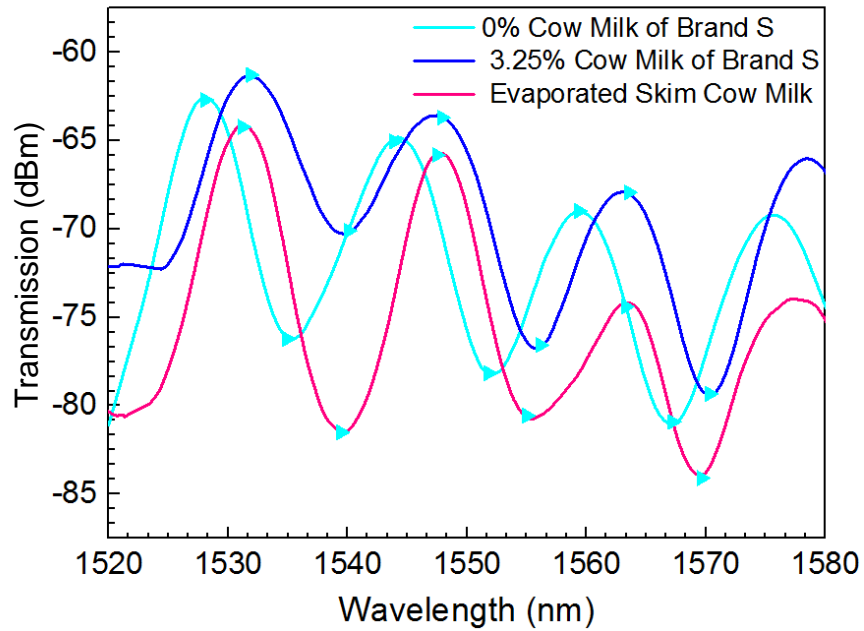


Figure 3-17 Transmission spectra of the evaporated skim cow milk compared with the 0% and 3.25% cow milk from Brand S by a triple-spiral waveguide sensor

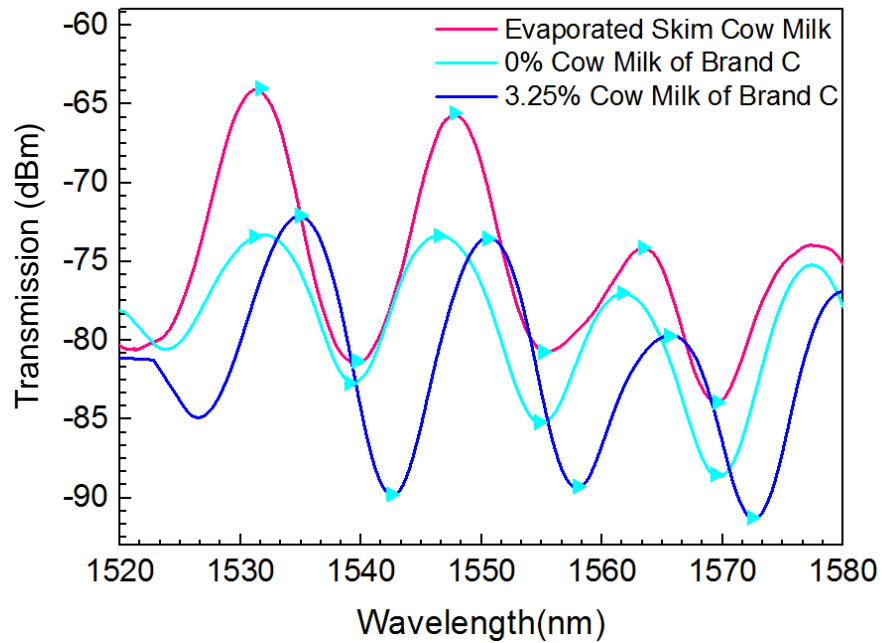


Figure 3-18 Transmission spectra of the evaporated skim cow milk compared with the 0% and 3.25% cow milk from Brand C by a triple-spiral waveguide sensor

3.3 Aging process of milk at room temperature

The 3.25% milk of Brand S and raw farm milk are both used to test whether being left in room temperature influences the refractive index of the milk. The milk samples are left in room temperature (around 22.8°C) for two nights. The samples are then tested with the triple-spiral waveguide sensor at three stages: the time the products are immediately removed from the fridge, 24 hours after being left in room temperature and 48 hours after being left in room temperature. The results are shown in Fig. 3-19.

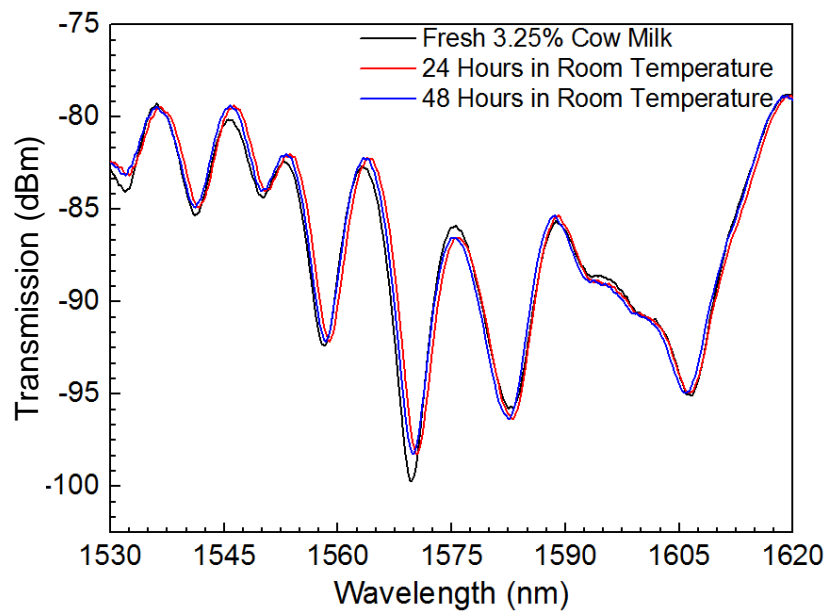


Figure 3-19 Transmission spectra of aging 3.25% homogenized cow milk kept at room temperature

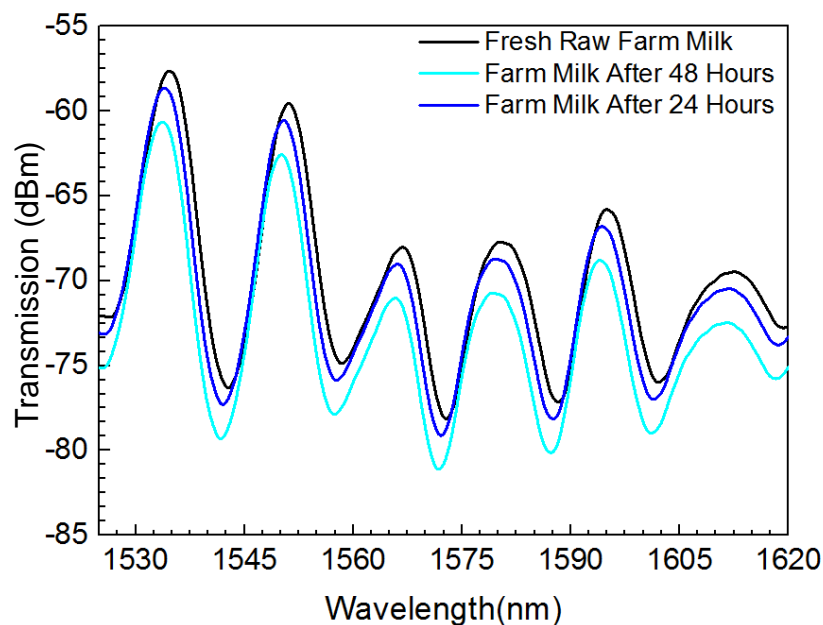


Figure 3-20 Transmission spectra of aging raw farm milk kept at room temperature

The 3.25% milk goes through the homogenization process before being distributed to the market, which means the fat globules are broken down into smaller molecules. After homogenization, smaller-sized fat globules will suspend in the milk fluid and will not easily float up to the surface of milk. On the contrary, the original fat globules in the raw milk will gradually reach the surface of milk and form a layer of milk fat. This can be a cause of the refractive index change observed in the transmission spectra of raw farm milk in Fig. 3-20. Figure 3-21 gives the difference in the change in refractive index in the aging processes of the homogenized milk and the raw farm milk.

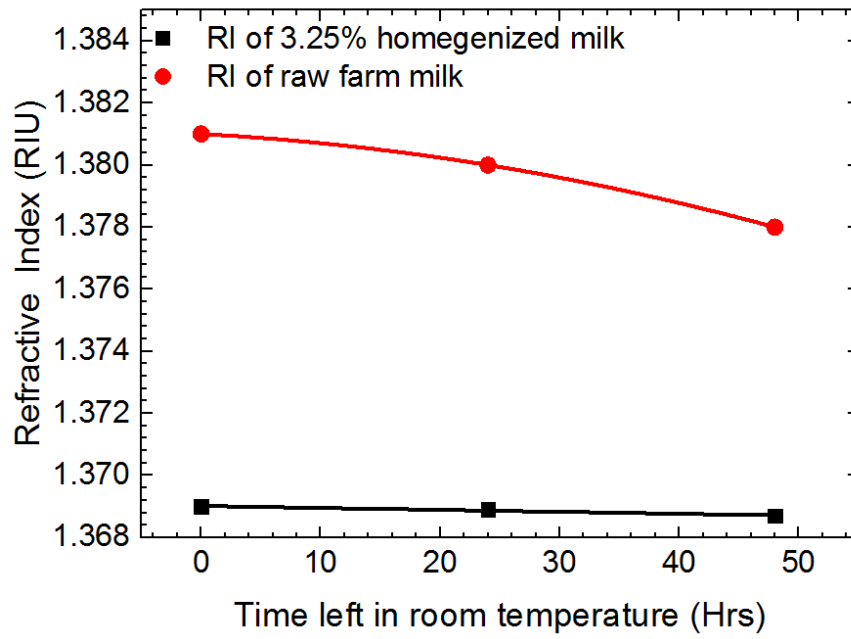


Figure 3-21 Changes in refractive indices of both the raw farm milk and the homogenized milk during aging process

3.4. Refractive indices of sucrose solution

The refractive index of a fluidic solution changes with the varying concentration of sucrose in the solution. This change is due to an increase in the density of the particles in the solution, which changes the atomic interactions in the solvent. In this study, sucrose solutions with different concentrations (1, 6, 12, 18, and 24 wt%) are tested with the spiral-shaped waveguide optofluidic sensors. Coupled light passing through a spiral-shaped waveguide sensor filled with sucrose solution is shown in Fig. 3-22.

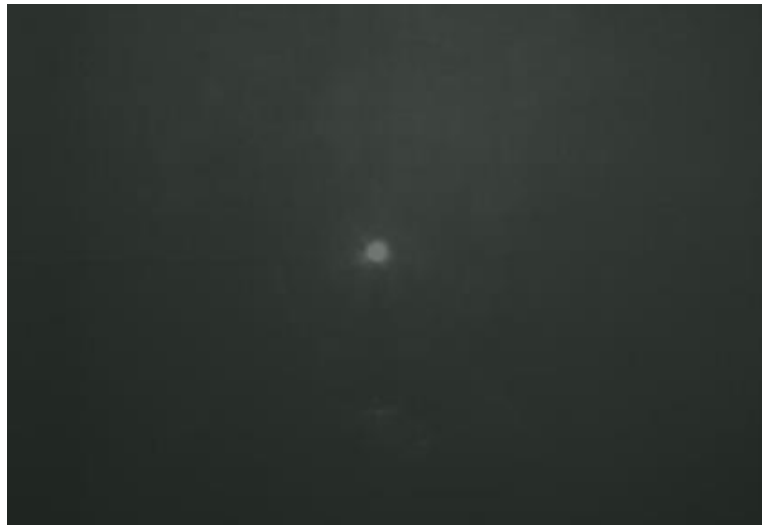


Figure 3-22 Coupled light transmitted by the single-spiral waveguide sensor passing through sucrose solution

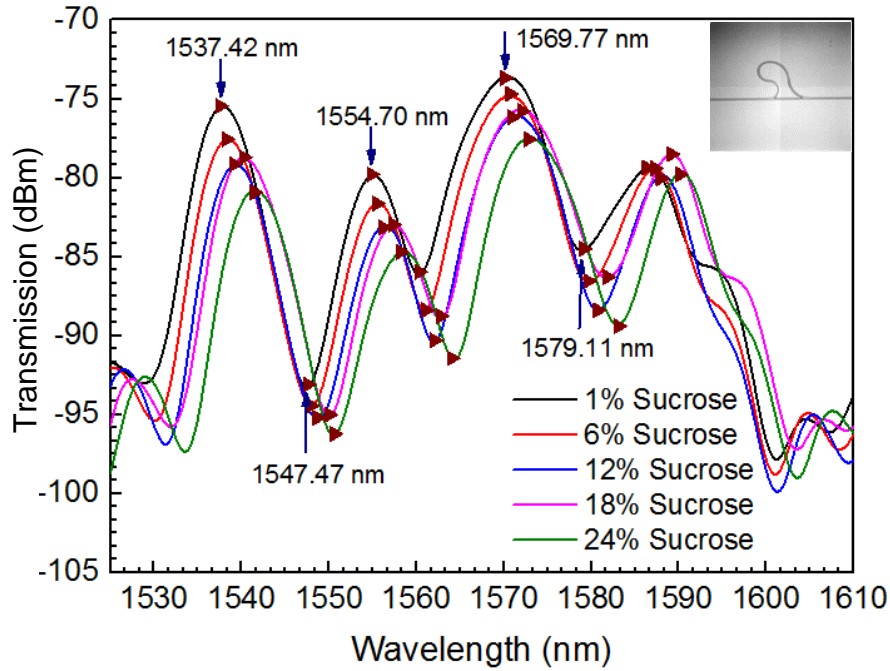


Figure 3-23 Shifts in transmission spectra of the single-spiral waveguide sensor with sucrose solutions of different concentrations

Figure 3-23 shows the transmission spectra of the sucrose solutions with varied concentrations, tested by the single-spiral waveguide sensor. A red shift is observed on the transmission spectra, which is caused by the increase of effective refractive index – a result of the RI increase of the infused sucrose solution inside the microchannel. The concentration sensing results are shown in Table 3-4. Figure 3-24 (a), (b), (c), (d), and (e) represent wavelength shifts of five identified peaks and valleys and (f) is a comparison of the wavelength shifts of these extrema.

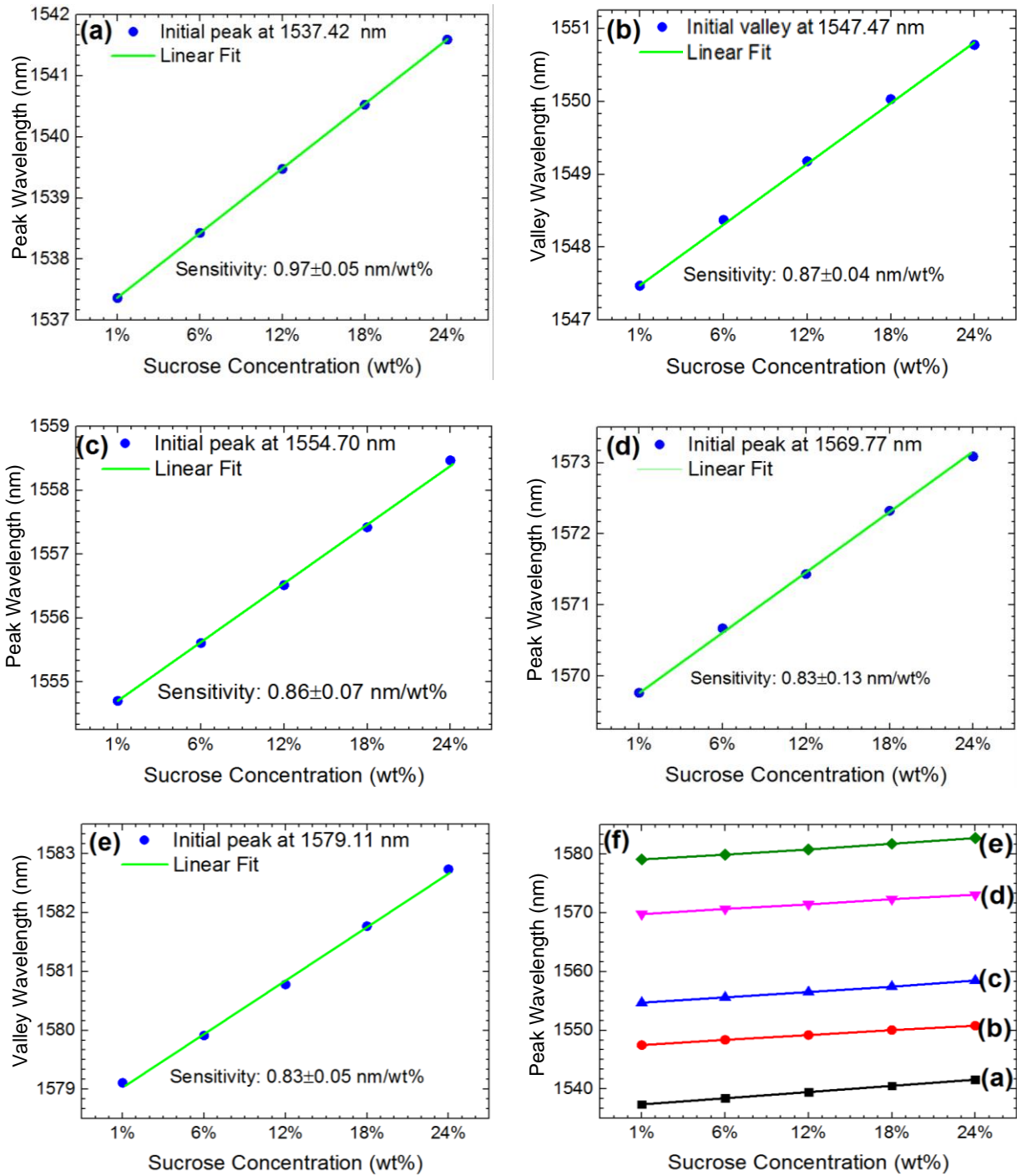


Figure 3-24 (a) – (e) Resonance peak shifts, and (f) comparison of peak shifts of single-spiral waveguide sensor for sucrose concentration sensing

Table 3-4 RI of sucrose concentration sensing with single-spiral optofluidic waveguide sensor

Sucrose Concentration	Refractive Index (RIU)
1%	1.332±0.001
6%	1.340±0.003
12%	1.351±0.001
18%	1.362±0.002
24%	1.372±0.002

Figure 3-25 shows the transmission spectra of the sucrose solutions of different concentrations tested by the double-spiral waveguide sensor. The infusion of sucrose solutions of higher refractive indices into the microchannel has led to a red shift in the transmission spectra. This is due to the fact that an increase in the RI of the sucrose solution has caused an increase in the effective refractive index of the sensor chip. Peak wavelengths are identified from the transmission spectra and the peak shifts are calculated and shown in Fig. 3-26. The identification of refractive indices of the sucrose solutions offers a calibration for the measurements in the future.

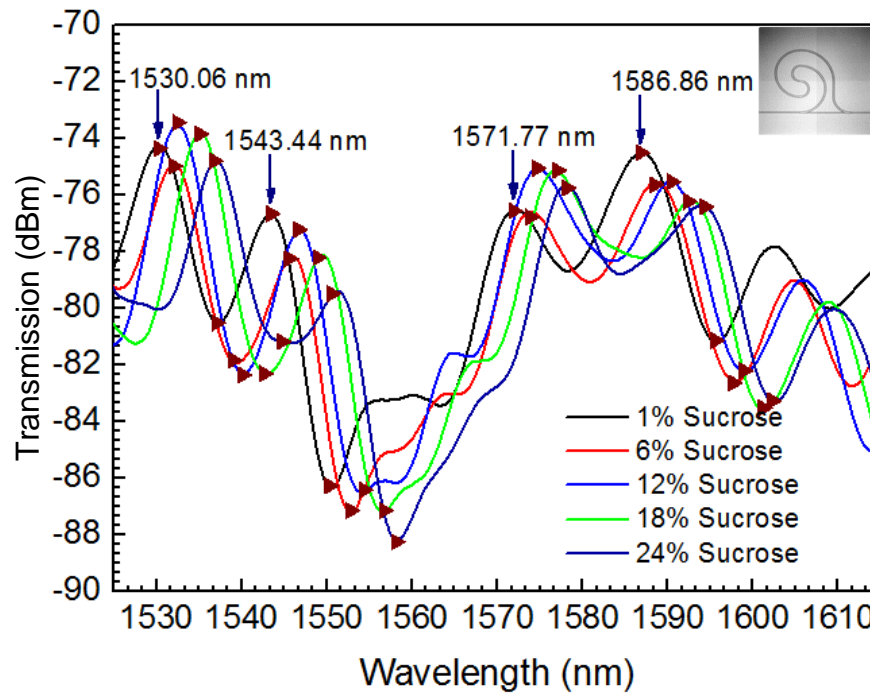


Figure 3-25 Shifts in transmission spectra of the double-spiral waveguide sensor with sucrose solutions of different concentrations

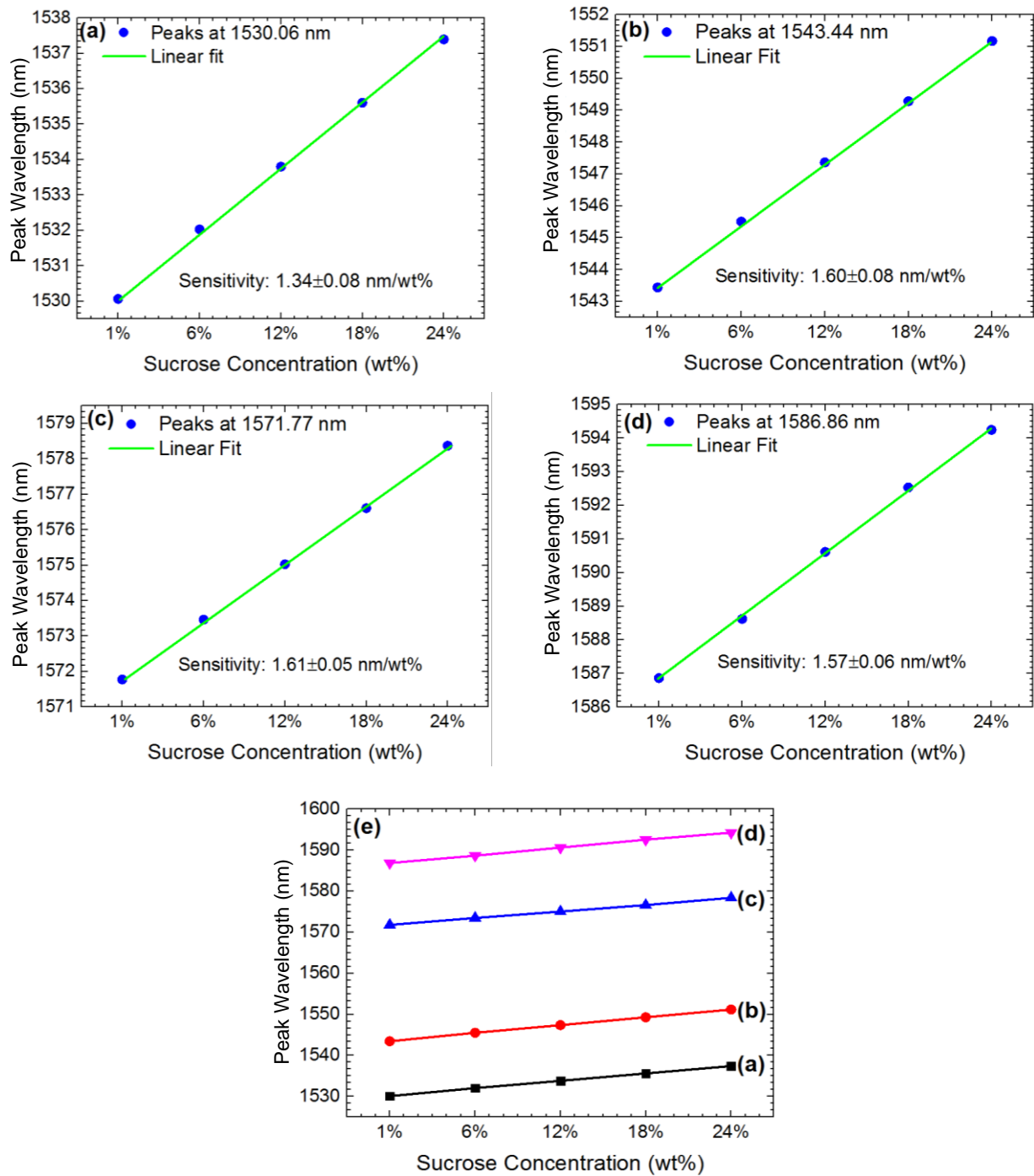


Figure 3-26 (a) – (d) resonance peak shifts, and (e) comparison of peak shifts of double-spiral waveguide sensor for sucrose concentration sensing

Table 3-5 demonstrates the results of refractive index sensing, which is shown in Fig. 3-25. With the calibration of the refractive index of sucrose solutions, the concentration of a sucrose solution can be identified by checking the locations of the peak shifts in the transmission spectra (Fig. 3-25). Figures 3-26, (a), (b), (c), and (d) represent four peak shifts and (e) is a comparison of the four located peak shifts.

Table 3-5 RI of sucrose concentration sensing with double-spiral optofluidic waveguide sensor

Sucrose Concentration	Refractive Index (RIU)
1%	1.330±0.001
6%	1.341±0.001
12%	1.354±0.002
18%	1.361±0.001
24%	1.371±0.003

Sucrose solutions of five concentrations (1%, 6%, 12%, 18%, and 24%, respectively) are then injected into the microchannel of the triple-spiral waveguide sensor. Figure 3-26 shows the transmission spectra collected by the OSA. With the increase of the RI of the injected sucrose solution, a red shift is seen on the transmission spectra, as expected. The results of the concentration sensing are shown in Table 3-6. Figure 3-27 (a), (b), (c), and (d) represent four identified shifts of valley wavelengths and (e) is a comparison of the four valleys.

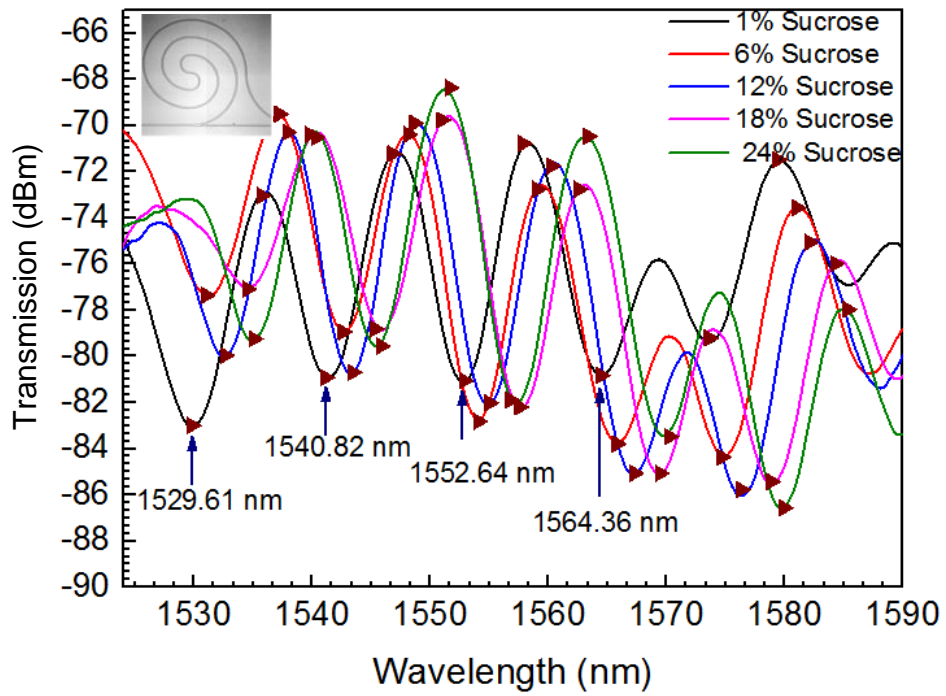


Figure 3-27 Shifts in transmission spectra of the triple-spiral waveguide sensor with sucrose solutions of different concentrations

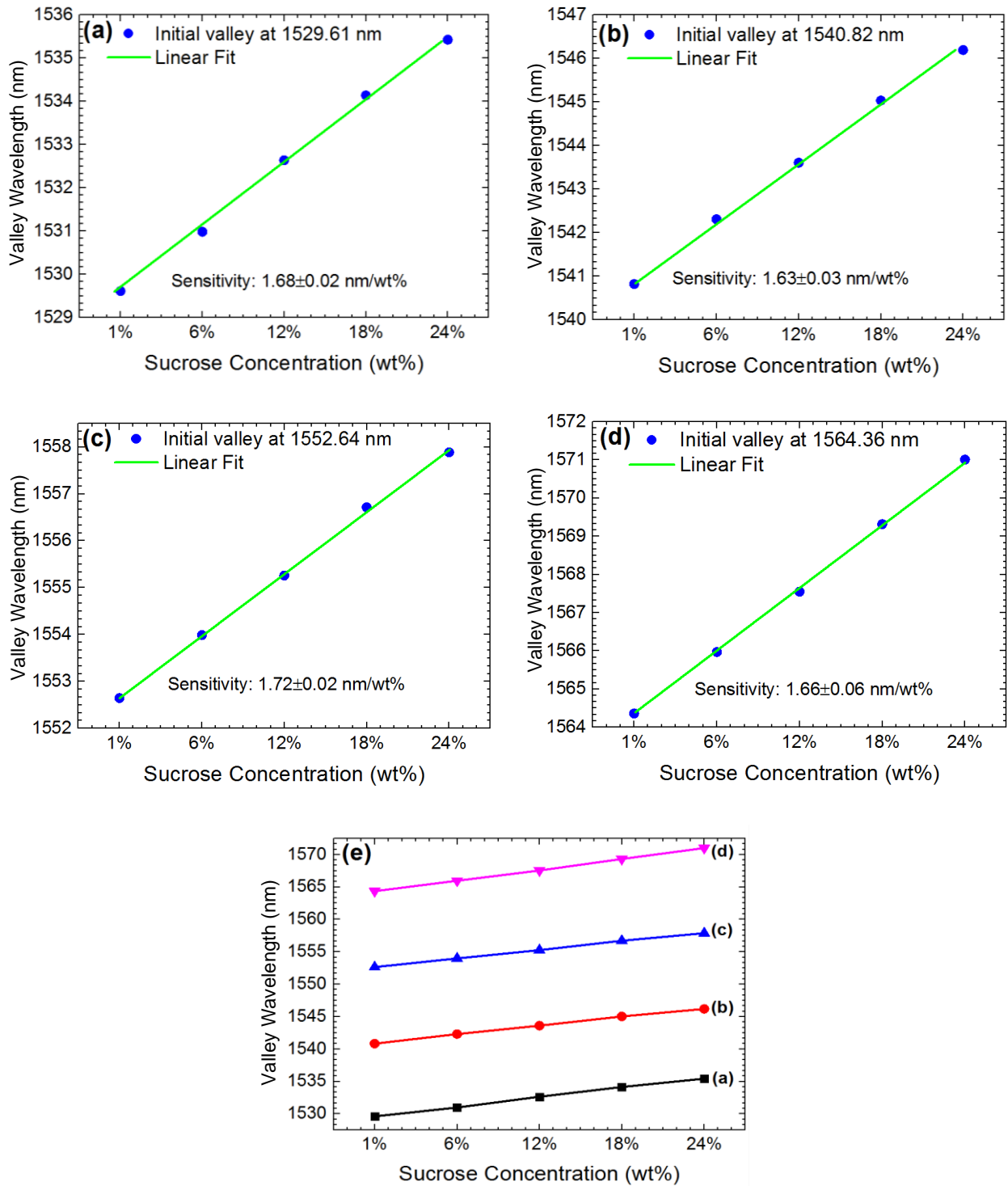


Figure 3-28 (a) – (d) Resonance peak shifts, and (e) comparison of peak shifts of triple-spiral waveguide sensor for sucrose concentration sensing

Table 3-6 RI of sucrose concentration sensing with triple-spiral optofluidic waveguide sensor

Sucrose Concentration	Refractive Index (RIU)
1%	1.332±0.002
6%	1.340±0.002
12%	1.354±0.001
18%	1.361±0.002
24%	1.371±0.001

The quadruple-spiral waveguide sensor is then used to measure the RIs of the sucrose solutions of five concentrations: 1%, 6%, 12%, 18%, and 24%, respectively. Figure 3-28 shows the shifts in the transmission spectra of the triple-spiral waveguide sensor when shifting from 1% to 24% sucrose solutions. Similarly, a red shift is seen on the transmission spectra. The concentration sensing results are shown in Table 3-7 and the peaks are identified and shown in Fig. 3-29(a), (b), (c), (d), and (e). Figure 3-29(f) lists a comparison of the shifts of the four identified peak groups.

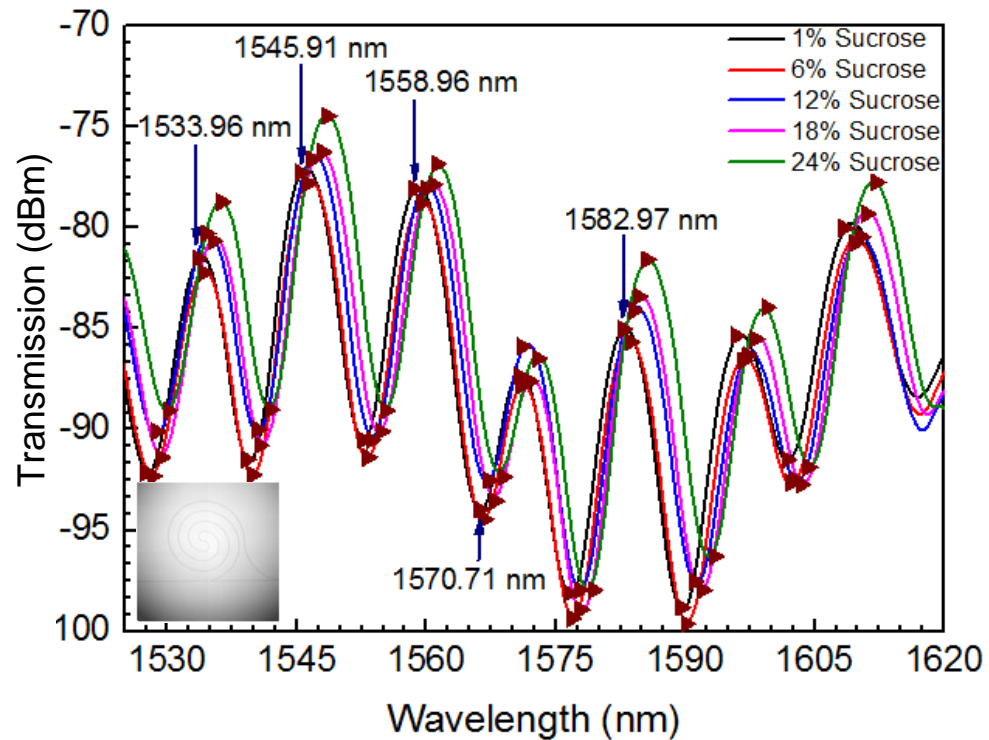


Figure 3-29 Shifts in transmission spectra of the quadruple-spiral waveguide sensor with sucrose solutions of different concentrations

Table 3-7 RI of sucrose concentration sensing with quadruple-spiral optofluidic waveguide sensor

Sucrose Concentration	Refractive Index (RIU)
1%	1.331±0.001
6%	1.341±0.003
12%	1.354±0.002
18%	1.359±0.001
24%	1.369±0.004

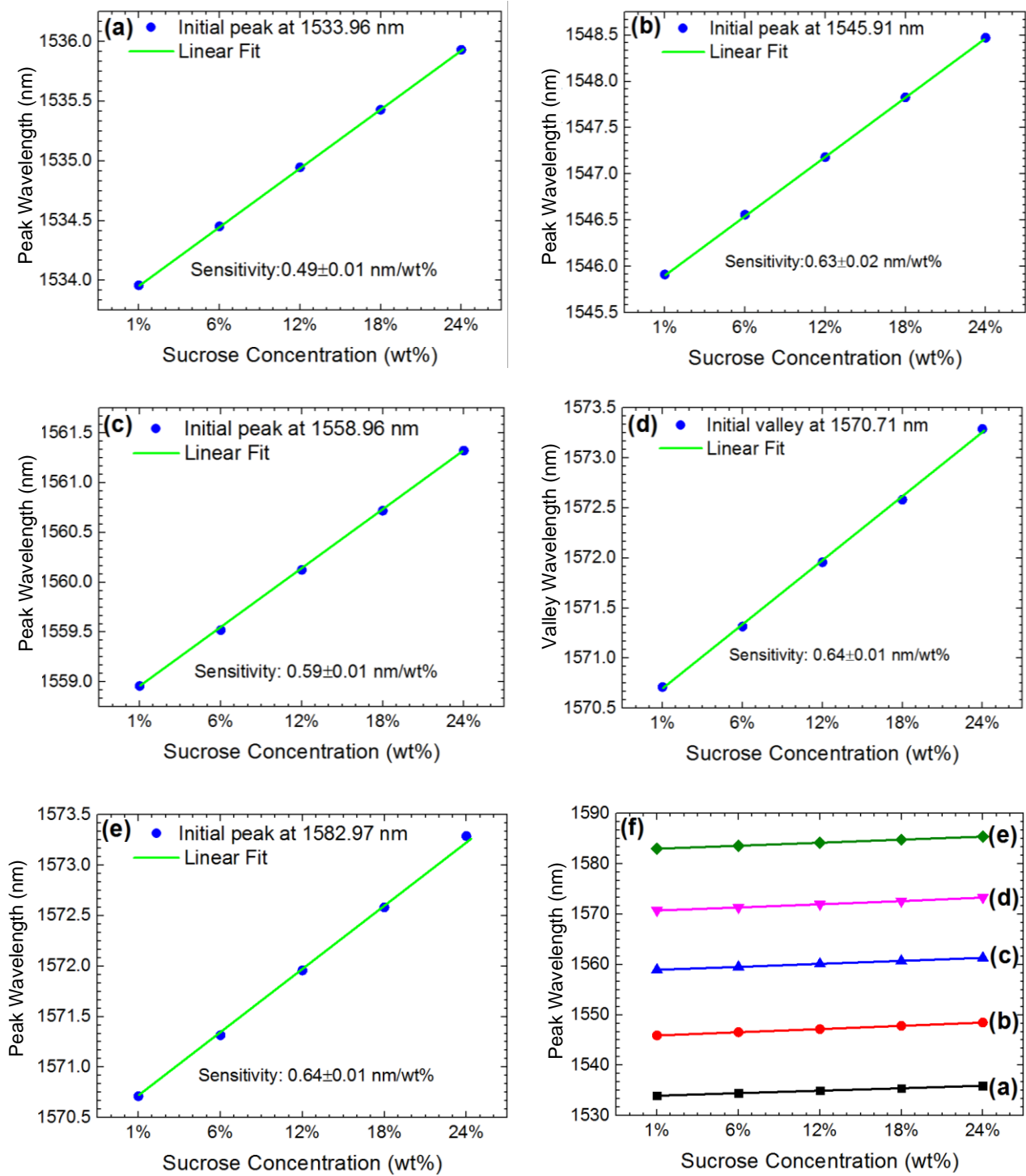


Figure 3-30 (a) – (e) Resonance peak shifts, and (f) comparison of peak shifts of quadruple-spiral waveguide sensor for sucrose concentration sensing

Table 3-8 Refractive indices of sucrose solutions [156]

Sucrose Concentration	Refractive Index (RIU)
1%	1.3344
6%	1.3418
12%	1.3509
18%	1.3606
24%	1.3706

Monitoring the saccharinity of sucrose solution plays an important role in terms of evaluating food quality and bacteria cultivation. In this section, the refractive indices of sucrose solutions with different concentrations are calibrated for further use of sucrose concentration sensing. The sucrose solutions are tested with single, double, triple, and quadruple-spiral optofluidic waveguide sensors, respectively. The sensing results from these four waveguide sensors all agree with the RI values given by “the Handbook of Physics and Chemistry, 97th Edition” [149], which are listed in Table 3-8. The highest sensitivities are still achieved by the triple-spiral waveguide sensor, which range from 1.63 to 1.72 nm/wt%.

3.5 Conclusion

The triple-spiral optofluidic waveguide sensor is used as the sensing tool in this chapter due to its steady performance and high sensitivity. The investigation on the role of fat content in changes in the refractive index of cow milk is first carried out with the triple-

spiral waveguide sensor. Results demonstrate that the RI of cow milk increased with the increase of the percentage of fat content. This is due to more scattering components such as fat globules in milk that cause more refraction of the transmitting light. Table 3-9 lists the main compositions of cow milk with different fat contents. Fat globules and protein are the large particles that determine the refractive index of milk. The technology to reduce fat does not influence the content of protein in milk as can be seen in Table 3-9. Vitamins, minerals, sodium, and cholesterol are either too small in size or too little in content to have an influence on the RI of milk [170].

Table 3-9 Main compositions in cow milk (per 100 g) [171]

Fat percentage \ Compositions	0%	0.5%	1%	2%	3.25%
Fat	0 g	0.2g	3 g	5 g	8 g
Protein	9 g	9g	9 g	9 g	9 g
Carbohydrate	12 g	12g	12 g	12 g	12 g
Cholesterol	5 mg	5 mg	10 mg	20 mg	24 mg
Sodium	103 mg	103 mg	127 mg	127 mg	127mg

A small difference is seen in the refractive index of milk with the same fat content from different producers. This is due to each producer having their own cow-raising and milk processing protocols. Optical properties of milk-like products such as almond milk and coconut milk are investigated next. The test results reveal that the RI of almond milk is lower than that of coconut milk, which is expected as for the same amount of the two

products, coconut milk contains higher percentage of fat than almond milk. Evaporated skim milk is also tested and is seen a higher RI than regular skim milk, as evaporated milk is much more condensed. The aging process of cow milk is then explored, and results show that raw milk has a bigger change in its refractive index than its homogenized counterpart. The last sample of milk that is tested is organic milk, whose RI is compared with the RIs of non-organic milk products. There are not significant differences observed. The experiment results of the comparisons among Brand S/Brand C cow milk, raw farm milk/homogenized milk, and organic/non-organic milk show that the refractive indices of cow milk and milk-like samples are more easily affected by more on post-milking treatment than on the raising conditions of cows. In the end, the refractive indices of sucrose solutions of different concentrations (1, 6, 12, 18, and 24 wt%) are investigated in this study. These are calibrated with the single, double, triple, and quadruple-spiral waveguide sensors, respectively.

Chapter 4 Conclusions

The aim of this thesis is to investigate the use of two photon absorption process in the fabrication in photoresist SU-8-2 with femtosecond laser, and furthermore to explore the possibility of fs laser microfabrication in achieving integrated optofluidic devices. In this study, the effectiveness of femtosecond laser microfabrication in realizing complicated shape with high resolution has been demonstrated. Compact spiral waveguides of different specifications are fabricated by femtosecond laser two photon absorption technique with high accuracy.

This thesis research performs femtosecond laser microfabrication of spiral optofluidic device in SU-8-2 and their sensing applications. The spiral optofluidic sensors are of good integrability, functionality, and high sensitivity (-0.47 ± 0.02 nm/°C for temperature sensing, 188.78 ± 3.76 nm/RIU for refractive index sensing, 0.089 ± 0.03 nm/(N/m²) for positive pressure sensing, and 1.66 ± 0.06 nm/wt% for sensing the saccharinity of sucrose solutions). This study also initiates the utilization of optofluidics to understand the optical properties of cow milk as well as non-dairy biomaterials, and to investigate the dynamics of optical properties of milk during its aging process. This is an important step to the future work of assessing the quality of beverages based on their refractive indices. Furthermore, the spiral optofluidic waveguide sensors can be applied in analytical chemistry, fluids, and biomaterial science and engineering.

4.1 Temperature sensing

Temperature sensing is based on the fact that there will be a change in the effective refractive index of the sensing device due to temperature changes. By monitoring the shift of the interference patterns of the device, the wavelengths of the peaks and valleys can be calibrated from the transmission spectra and used for quantitative sensing of an unknown temperature. In this study, temperature sensing experiments are conducted with four spiral waveguide sensors and the interference patterns are recorded by the optical spectrum analyzer. The wavelengths of peaks and valleys of the interference patterns in the transmission spectra are identified as calibrations.

All the tested sensor chips exhibit steady interference patterns following modifications in temperature. The linear fit of the peak shift diagrams is calculated to obtain sensitivity values. The highest sensitivity achieved is -0.47 ± 0.02 nm/°C with the triple-spiral optofluidic waveguide sensor. The blue shift is due to the negative thermo-optic coefficient of the waveguide material (SU-8-2). This shows that the spiral waveguide sensor achieved in this study is capable of thermo-optofluidic sensing.

4.2 Refractive index and concentration sensing

Refractive index sensing and concentration sensing are two parameters related to each other due to the fact that the molar concentration of any solution is essentially related to the refractive index of that solution. In this study, the calibration of refractive index sensing was carried out prior to the sensing of concentration of fluid solutions. The

refractive index sensing experiments are implemented with the four spiral waveguide sensors and the interference patterns are recorded by the optical spectrum analyzer. The refractive indices of CaCl_2 solutions with different concentration can be found in the Handbook of Chemistry and Physics [156]. The wavelengths of peaks and valleys of the interference patterns in the transmission spectra with different RIs of the CaCl_2 solutions are identified. All the sensor chips exhibit good performance in reusability, and clear interference patterns are observed following manipulation of the RI. From the sensitivity derived from the linear fit of the shifts in the peak wavelengths, the highest sensitivity achieved is 188.78 ± 3.76 nm/RIU, which is obtained by the triple-spiral optofluidic waveguide sensor.

Based on the calibration of RI sensing results, experiments on liquid concentration sensing were conducted on samples of sucrose solutions with different sucrose concentrations (wt%). A steady red shift of the transmission spectrum is observed, which forms the basis of concentration sensing. The experimental results of sucrose solution concentration sensing were then compared with the recorded value in “The Handbook of Chemistry and Physics” [156], in which a satisfactory agreement has been found.

4.3 Positive pressure sensing

The ability to sense small change in positive pressure added onto the sensor chip again indicates that high sensitivity can be achieved with effective refractive index sensing. The effective refractive index is not only related to the waveguide material and the

wavelength of the incident light, but it also depends on the deformation of the waveguide device and subsequent propagation modes. As the positive pressure on the sensor chip increases, a steady red shift of the transmission spectrum is observed, proving that the spiral waveguide sensor is capable of positive pressure sensing. The highest sensitivity achieved is $0.089 \pm 0.003 \text{ nm/ (N/m}^2\text{)}$ using the triple-spiral waveguide sensor.

4.4 Spiral optofluidic sensor for bio-sensing applications

In the last part of this study, biological sensing of milk and non-dairy biomaterials was carried out. The purpose of this experiment is to understand the intrinsic and extrinsic factors influencing the optical properties of milk and non-dairy products. The influence of the percentage of fat globules in cow milk is studied and an increase in refractive index is seen as the percentage of fat in milk becomes higher (0%, 0.5%, 1%, 2%, and 3.25%). The optical properties of non-dairy milk-like products such as almond milk are investigated with the triple-spiral waveguide sensor next, followed by the study of the aging process of milk at room temperature and the ways in which the refractive index of milk changes. Chapter 3 shows that the designed spiral optofluidic sensor used for biological analysis fully satisfies the objective of this thesis.

4.5 Future research

Potential future research of optofluidic spiral waveguide devices may include the

fabrication of a ‘slot spiral waveguide’. A slot-waveguide structure has been previously fabricated with silicon [140, 141]. The silicon slot-waveguide contains two bus waveguides and a gap in between them with a width of around 200 nm. It is observed that if the width of the gap is small enough (several hundred nanometers), an incident light is able to travel through the gap [142]. An optofluidic slot-waveguide can be fabricated with fs laser. The fs laser exposure can be used on a SU-8-2 thin film to fabricate two bus waveguides in close proximity to each other. However, the requirement on the motion accuracy of the motion stage is very high. In order to create two bus waveguides which are several hundreds of nanometers away from each other, the step resolution of the motion stage should be well below 200 nm. The accuracy of the motion stage in our lab is around 500 nm, which does not allow this experiment to happen. Another experiment that could not be done due to the time limit is to use the spiral SU-8-2 waveguide as an optofluidic optical switch. Interference patterns could be taken into consideration prior to the design of the optofluidic light-switch device.

Bibliography

- [1] C. Monat, P. Domachuk, and B. J. Eggleton, “Integrated optofluidics: A new river of light,” *Nat. Photonics*, vol. 1, no. 2, pp. 106–114, 2007.
- [2] K. S. Riken, “Femtosecond laser processing for biochip applications,” *Pacific Rim Conf. Lasers Electro-Optics, CLEO - Tech. Dig.*, pp. 0–1, 2013.
- [3] N. T. Nguyen, “Micro-optofluidic Lenses: A review,” *Biomicrofluidics*, vol. 4, no. 3, pp. 1–15, 2010.
- [4] C. Cha and J. Oh, “An optofluidic mechanical system for elasticity measurement of thin biological tissues,” *Biotechnol. Lett.*, vol. 35, no. 5, pp. 825–830, 2013.
- [5] J. Wan, F. L. Xue, L. X. Wu, Y. J. Fu, J. Hu, W. Zhang, and F. R. Hu, “Extensible chip of optofluidic variable optical attenuator,” *Opt. Express*, vol. 24, no. 9, p. 9683-9692, 2016.
- [6] S. H. Cho, J. Godin, and Y. H. Lo, “Optofluidic waveguides in Teflon AF-coated PDMS microfluidic channels,” *IEEE Photonics Technol. Lett.*, vol. 21, no. 15, pp. 1057–1059, 2009.
- [7] M. Elitaş, M. Yüce, and H. Budak, “Microfabricated tools for quantitative plant biology,” *Analyst*, vol. 142, no. 6, pp. 835–848, 2017.
- [8] D. Ozcelik, J. Parks, T. Wall, M. Scott, H. Cai, J. Parks, R. Hawkins, and H. Schmidt, “Optofluidic wavelength division multiplexing for single-virus detection,” *Proc. Natl. Acad. Sci.*, vol. 112, no. 42, pp. 12933–12937, 2015.
- [9] D. Brennan, J. Justice, B. Corbett, T. McCarthy, and P. Galvin, “Emerging

- optofluidic technologies for point-of-care genetic analysis systems: A review,” *Anal. Bioanal. Chem.*, vol. 395, no. 3, pp. 621–636, 2009.
- [10] P. J. Kitson, M. H. Rosnes, V. Sans, V. Dragone, and L. Cronin, “Configurable 3D-Printed millifluidic and microfluidic ‘lab on a chip’ reactionware devices,” *Lab Chip*, vol. 12, no. 18, pp. 3267–3271, 2012.
- [11] V. Srinivasan, V. K. Pamula, and R. B. Fair, “An integrated digital microfluidic lab-on-a-chip for clinical diagnostics on human physiological fluids,” *Lab Chip*, vol. 4, no. 4, pp. 310–315, 2004.
- [12] S. Balslev, A. Jorgensen, B. Bilenberg, K. Mogensen, D. Snakenborg, O. Geschke, J. Kutter, A. Kristensen, “Lab-on-a-chip with integrated optical transducers,” *Lab Chip*, vol. 6, no. 2, pp. 213–217, 2006.
- [13] L. Li, R. Chen, Q. Liao, X. Zhu, G. Wang, and D. Wang, “High surface area optofluidic microreactor for redox mediated photocatalytic water splitting,” *Int. J. Hydrogen Energy*, vol. 39, no. 33, pp. 19270–19276, 2014.
- [14] L. Li, R. Chen, X. Zhu, H. Wang, Q. Liao, D. Wang, “Optofluidic microreactors with TiO₂-coated fiberglass,” *ACS Appl. Mater. Interfaces*, vol. 5, no. 23, pp. 12548–12553, 2013.
- [15] T. Ohori, S. Shoji, K. Miura, and A. Yotsumoto, “Partly disposable three-way microvalve for a medical micro total analysis system (μ TAS),” *Sensors Actuators A Phys.*, vol. 64, no. 1, pp. 57–62, 1998.
- [16] O. T. Guenat, D. Ghiglione, W. E. Morf, and N. F. de Rooij, “Partial electroosmotic pumping in complex capillary systems. Part 2: Fabrication and application of a micro total analysis system (μ TAS) suited for continuous

- volumetric nanotitrations,” *Sensors Actuators, B Chem.*, vol. 72, no. 3, pp. 273–282, 2001.
- [17] L. Hu, J. Ye, H. Tan, A. Ge, L. Tang, X. Feng, W. Du, and B. Liu, “Quantitative analysis of *Caenorhabditis elegans* chemotaxis using a microfluidic device,” *Anal. Chim. Acta*, vol. 887, pp. 155–162, 2015.
- [18] R. A. Escalona-Villalpando, R. C. Reid, R. D. Milton, L. G. Arriaga, S. D. Minter, and J. Ledesma-García, “Improving the performance of lactate/oxygen biofuel cells using a microfluidic design,” *J. Power Sources*, vol. 342, pp. 546–552, 2017.
- [19] X. Hu, L. Lu, C. Fang, B. Duan, and Z. Zhu, “Determination of Apparent Amylose Content in Rice by Using Paper-Based Microfluidic Chips,” *J. Agric. Food Chem.*, vol. 63, no. 44, pp. 9863–9868, 2015.
- [20] R. Blue, A. Duduś, and D. Uttamchandani, “A Review of Single-Mode Fiber Optofluidics,” *IEEE J. Sel. Top. Quantum Electron.*, vol. 22, no. 2, p. 9100112, 2016.
- [21] D. Psaltis, A. E. Vasdekis, and J.-W. Choi, “Optofluidics of plants,” *APL Photonics*, vol. 1, no. 2, p. 20901, 2016.
- [22] Y. Deng, M. N. Idso, D. D. Galvan, and Q. Yu, “Optofluidic microsystem with quasi-3 dimensional gold plasmonic nanostructure arrays for online sensitive and reproducible SERS detection,” *Anal. Chim. Acta*, vol. 863, no. 1, pp. 41–48, 2015.
- [23] D. Zhang, “Oopto-microfluidic devices with femtosecond laser microfabrication,” PhD Thesis, Memorial University of Newfoundland, 2016.
- [24] A. Schaap, Y. Bellouard, and T. Rohrlack, “Optofluidic lab-on-a-chip for rapid

- algae population screening,” *Biomed. Opt. Express*, vol. 2, no. 3, pp. 658–64, 2011.
- [25] X. Cheng, R. Chen, X. Zhu, Q. Liao, X. He, S. Li, and L. Li, “Optofluidic membrane microreactor for photocatalytic reduction of CO₂,” *Int. J. Hydrogen Energy*, vol. 41, no. 4, pp. 2457–2465, 2016.
- [26] G. Persichetti, I. A. Grimaldi, G. Testa, and R. Bernini, “Multifunctional optofluidic lab-on-chip platform for Raman and fluorescence spectroscopic microfluidic analysis,” *Lab Chip*, vol. 17, no. 15, pp. 2631–2639, 2017.
- [27] K. Campbell and A. Groisman, “A microfluidic 2×2 optical switch,” *Appl. Phys. Lett.*, vol. 85, no. 25, pp. 6119–6121, 2004.
- [28] E. Weber and M. J. Vellekoop, “Optofluidic micro-sensors for the determination of liquid concentrations,” *Lab Chip*, vol. 12, no. 19, pp. 3754–3759, 2012.
- [29] X. Tang, S. Liang, and R. Li, “Design for controllable optofluidic beam splitter,” *Photonics Nanostructures - Fundam. Appl.*, vol. 18, pp. 23–30, 2016.
- [30] A. Yamaguchi, T. Fukuoka, R. Takahashi, R. Hara, and Y. Utsumi, “Dielectrophoresis-enabled surface enhanced Raman scattering on gold-decorated polystyrene microparticle in micro-optofluidic devices for high-sensitive detection,” *Sensors Actuators, B Chem.*, vol. 230, pp. 94–100, 2016.
- [31] F. Pujol-Vila, P. Gomez, N. Santamaria, B. Antunez, N. Vignes, M. Diaz-Gozalet, C. Jimenez-Jorquera, I. Mas, J. Sachistan, and X. Munoz-berbel, “Portable and miniaturized optofluidic analysis system with ambient light correction for fast in situ determination of environmental pollution,” *Sensors Actuators, B.*, vol. 222, no.1, pp. 55–62, 2016.

- [32] M. Nagai, K. Kato, and T. Shibata, “Underwater motion of hydrogel microstructure by optofluidic lithography studied with gap control and object holding platform,” *Microelectron. Eng.*, vol. 164, pp. 108–114, 2016.
- [33] Y. Yang, A. Liu, L. Chin, X. Zhang, D. Tsai, C. Lin, C. Lu, G.P. Wang, and N. Zheludev, “Optofluidic waveguide as a transformation optics device for lightwave bending and manipulation,” *Nat. Commun.*, vol. 3, p. 651, 2012.
- [34] P. Lin, S. Kwok, H. Lin, V. Singh, L. Kimerling, G. Whitesides, D. Tan, and A. Agrawal, “Mid-Infrared Opto-Nanofluidic Slot-Waveguide for Label-Free On-Chip Chemical Sensing.” *Nano Lett.*, vol. 14, no. 1, pp 231–238, 2014.
- [35] G. Persichetti, G. Gesta, and R. Bernini, “High sensitivity UV fluorescence spectroscopy based on an optofluidic jet waveguide.” *Opt. Express*, vol. 21, no. 20, pp. 24219–30, 2013.
- [36] A. K. Goyal and S. Pal, “Design and simulation of high sensitive photonic crystal waveguide sensor,” *Opt. - Int. J. Light Electron Opt.*, vol. 126, no. 2, pp. 240–243, 2015.
- [37] A. Yildirim, F. E. Ozturk, and M. Bayindir, “Smelling in chemically complex environments: An optofluidic bragg fiber array for differentiation of methanol adulterated beverages,” *Anal. Chem.*, vol. 85, no. 13, pp. 6384–6391, 2013.
- [38] B. Guo, C. Lei, T. Ito, Y. Jiang, Y. Ozeki, and K. Goda, “High-throughput optofluidic profiling of *Euglena gracilis* with morphological and chemical specificity,” vol. 40, no. 20, p. 100260, 2016.
- [39] X. Zhang, L. Liu, and L. Xu, “Ultralow sensing limit in optofluidic micro-bottle resonator biosensor by self-referenced differential-mode detection scheme,” *Appl.*

- Phys. Lett.*, vol. 104, no. 3, p. 033703, 2014.
- [40] R. D. Nerenz and A. M. Gronowski, “Improved Performance of Point-of-Care and Over-the-Counter Qualitative Human Chorionic Gonadotropin Measurement Devices,” *Clin. Chem.*, vol. 60, no. 12, pp. 1576–1578, 2014.
- [41] T. Gomes, D. N. Juurlink, B. R. Shah, J. M. Paterson, and M. M. Mamdani, “Blood glucose test strips: Options to reduce usage,” *Cmaj*, vol. 182, no. 1, pp. 35–38, 2010.
- [42] X. Fan and I. M. White, “Optofluidic Microsystems for Chemical and Biological Analysis,” *Nat. Photonics*, vol. 5, no. 10, pp. 591–597, 2011.
- [43] Y. Zhao, X. Li, L. Cai, and Y. Yang, “Refractive index sensing based on photonic crystal fiber interferometer structure with up-tapered joints,” *Sensors Actuators B Chem.*, vol. 221, pp. 406–410, 2015.
- [44] S. Ertman, P. Lesiak, and T. R. Wolinski, “Optofluidic Photonic Crystal Fiber-Based Sensors,” *J. Light. Technol.*, vol. 35, no. 16, pp. 3399–3405, 2016.
- [45] T.-W. Lu and P.-T. Lee, “Ultra-high sensitivity optical stress sensor based on double-layered photonic crystal microcavity,” *Opt. Express*, vol. 17, no. 3, p. 1518–1526, 2009.
- [46] S. Yan and F. Xu, “A review on optical microfibers in fluidic applications,” *J. Micromechanics Microengineering*, vol. 27, no. 9, p. 93001, 2017.
- [47] R.-M. Ma, R. F. Oulton, V. J. Sorger, G. Bartal, and X. Zhang, “Room-temperature sub-diffraction-limited plasmon laser by total internal reflection,” *Nat Mater*, vol. 10, no. 2, pp. 110–113, 2011.
- [48] C. Song, N.-T. Nguyen, A. K. Asundi, and S.-H. Tan, “Tunable micro-optofluidic

- prism based on liquid-core liquid-cladding configuration,” *Opt. Lett.*, vol. 35, no. 3, pp. 327–329, 2010.
- [49] V. Korampally, M. Hossain, M. Yun, K. Gangopadhyay, and L. Polo-parada, “A novel air/nanoporous dielectric clad optofluidic waveguide system for sensor applications,” *12th International Conference on Miniaturized Systems for Chemistry and Life Sciences - The Proceedings of MicroTAS 2008 Conference*, pp. 284–286, 2008.
- [50] G. Testa, G. Persichetti, and R. Bernini, “Optofluidic approaches for enhanced microsensor performances,” *Sensors (Switzerland)*, vol. 15, no. 1, pp. 465–484, 2015.
- [51] K. S. Lee, K. Lee, S. Kim, B. Ha, J. Jung, H. Sung, and S. Kim, “Dynamic manipulation of particles via transformative optofluidic waveguides,” *Sci. Rep.*, vol. 5, p. 15170, 2015.
- [52] J. Choi, K. S. Lee, J. H. Jung, H. J. Sung, and S. S. Kim, “Integrated real-time optofluidic SERS via a liquid-core/liquid-cladding waveguide,” *RSC Adv.*, vol. 5, no. 2, pp. 922–927, 2015.
- [53] W. Song and D. Psaltis, “Pneumatically tunable optofluidic 2×2 switch for reconfigurable optical circuit,” *Lab Chip*, vol. 11, no. 14, p. 2397–2402, 2011.
- [54] S. Pleasants, “Optofluidics: On-chip router,” *Nat Phot.*, vol. 8, no. 2, p. 85, 2014.
- [55] J.-H. Kim and H.-H. Park, “Total internal reflection optical switch using the reverse breakdown of a pn junction in silicon,” *Opt. Lett.*, vol. 40, no. 21, pp. 4859–4862, 2015.
- [56] B. Yalizay, Y. Morova, K. Dincer, Y. Ozbakir, A. Jonas, C. Erkey, A. Kiraz, S.

- Akturk, “Versatile liquid-core optofluidic waveguides fabricated in hydrophobic silica aerogels by femtosecond-laser ablation,” *Opt. Mater.*, vol. 47, no. Supplement C, pp. 478–483, 2015.
- [57] F. Du, “Development of an Optofluidic Platform Based on Total Internal Reflection- Application of Dissolved Oxygen Sensing for Water Monitoring,” Masters Thesis, McMaster University, 2015.
- [58] S. Tripura Sundari, R. Ramaseshan, F. Jose, S. Dash, and A. K. Tyagi, “TiN Harsha 57 Investigation of temperature dependent dielectric constant of a sputtered TiN thin film by spectroscopic ellipsometry,” *J. Appl. Phys. J. Appl. Phys. Appl. Phys. Lett. Appl. Phys. Lett.*, vol. 115, no. 10, pp. 101901–51110, 2014.
- [59] R. L. Aggarwal and T. Y. Fan, “Thermal diffusivity, specific heat, thermal conductivity, coefficient of thermal expansion, and refractive-index change with temperature in AgGaSe₂,” *Appl. Opt.*, vol. 44, no. 13, pp. 2673–2677, 2005.
- [60] T. S. Leite, P. E. D. Augusto, and M. Cristianini, “Using High Pressure Homogenization (HPH) to Change the Physical Properties of Cashew Apple Juice,” *Food Biophys.*, vol. 10, no. 2, pp. 169–180, 2015.
- [61] D. L. Johnsen, Z. Zhang, H. Emamipour, Z. Yan, and M. J. Rood, “Effect of isobutane adsorption on the electrical resistivity of activated carbon fiber cloth with select physical and chemical properties,” *Carbon N. Y.*, vol. 76, no. Supplement C, pp. 435–445, 2014.
- [62] Y. Shen, T. Nakayama, M. Arai, O. Yanagisawa, and M. Izumi, “Magnetic phase transition and physical properties of spinel-type nickel manganese oxide,” *J. Phys. Chem. Solids*, vol. 63, no. 6, pp. 947–950, 2002.

- [63] N. Almqvist, R. Bhatia, G. Primbs, N. Desai, S. Banerjee, and R. Lal, “Elasticity and Adhesion Force Mapping Reveals Real-Time Clustering of Growth Factor Receptors and Associated Changes in Local Cellular Rheological Properties,” *Biophys. J.*, vol. 86, no. 3, pp. 1753–1762, 2004.
- [64] D. Psaltis, S. R. Quake, and C. Yang, “Developing optofluidic technology through the fusion of microfluidics and optics,” *Nature*, vol. 442, no. 7101, pp. 381–386, 2006.
- [65] K.-P. S. Dancil, D. P. Greiner, and M. J. Sailor, “A Porous Silicon Optical Biosensor: Detection of Reversible Binding of IgG to a Protein A-Modified Surface,” *J. Am. Chem. Soc.*, vol. 121, no. 34, pp. 7925–7930, 1999.
- [66] J. Wan, F. Xue, B. Chen, H. Cao, M. Du, and F. Hu, “Optofluidic Chip of a Single-Mode Fiber Variable Optical Attenuator,” *IEEE Photonics J.*, vol. 9, no. 2, pp. 1–8, 2017.
- [67] Q. Chen, A. Jian, Z. Li, and X. Zhang, “Optofluidic tunable lenses using laser-induced thermal gradient,” *Lab Chip*, vol. 16, no. 1, pp. 104–111, 2016.
- [68] F. He, Y. Liao, J. Song, L. Qiao, Y. Cheng, K. Sugioka, “Femtosecond laser fabrication of monolithically integrated microfluidic sensors in glass,” *Sensors*, vol. 14, no. 10, pp. 19402–19440, 2014.
- [69] V. Gerginov, C. E. Tanner, S. a Diddams, A. Bartels, and L. Hollberg, “High-resolution spectroscopy with a femtosecond laser frequency comb,” *Opt. Lett.*, vol. 30, no. 13, pp. 1734–1736, 2005.
- [70] C.-W. Cheng and C.-Y. Lin, “High precision patterning of ITO using femtosecond laser annealing process,” *Appl. Surf. Sci.*, vol. 314, pp. 215–220, 2014.

- [71] V. Maselli, J. R. Grenier, S. Ho, and P. R. Herman, “Femtosecond laser written optofluidic sensor: Bragg grating waveguide evanescent probing of microfluidic channel,” *Opt. Express*, vol. 17, no. 14, pp. 11719–11729, 2009.
- [72] F. Bragheri, L. Ferrara, N. Bellini, K. Vishnubhatla, P. Minizioni, R. Ramponi, R. Osellame, and I. Cristian, “Optofluidic chip for single cell trapping and stretching fabricated by a femtosecond laser,” *J. Biophotonics*, vol. 3, no. 4, pp. 234–243, 2010.
- [73] D. Wu, J. Xu, L.-G. Niu, S.-Z. Wu, K. Midorikawa, and K. Sugioka, “In-channel integration of designable microoptical devices using flat scaffold-supported femtosecond-laser microfabrication for coupling-free optofluidic cell counting,” *Light Sci. Appl.*, vol. 4, no. 1, pp. 228, 2015.
- [74] D. Zhang, L. Men, and Q. Chen, “Microfabrication and applications of opto-microfluidic sensors,” *Sensors*, vol. 11, no. 5, pp. 5360–5382, 2011.
- [75] P. Lu and Q. Chen, “Femtosecond laser microfabricated fiber Mach-Zehnder interferometer for sensing applications,” *Opt. Lett.*, vol. 36, no. 2, pp. 268–270, 2011.
- [76] J. Serbin, A. Egbert, A. Ostendorf, B. N. Chichkov, R. Houbertz, G. Domann, J. Schulz, C. Cronauer, L. Fröhlich, and M. Popall, “Femtosecond laser-induced two-photon polymerization of inorganic organic hybrid materials for applications in photonics,” *Opt. Lett.*, vol. 28, no. 5, pp. 301–303, 2003.
- [77] H. Kumagai, K. Midorikawa, K. Toyoda, S. Nakamura, T. Okamoto, and M. Obara, “Ablation of polymer films by a femtosecond high-peak-power Ti:sapphire laser at 798 nm,” *Appl. Phys. Lett.*, vol. 65, no. 14, pp. 1850–1852, 1994.

- [78] H. Altug, D. Englund, and J. Vuckovic, “Ultrafast photonic crystal nanocavity laser,” *Nat Phys*, vol. 2, no. 7, pp. 484–488, 2006.
- [79] R. R. Gattass and E. Mazur, “Femtosecond laser micromachining in transparent materials,” *Nat Phot.*, vol. 2, no. 4, pp. 219–225, 2008.
- [80] H. B. Sun and S. Kawata, “Two-photon photopolymerization and 3D lithographic microfabrication,” *Adv. Polym. Sci.*, vol. 170, pp. 169–273, 2004.
- [81] S. Maruo, O. Nakamura, and S. Kawata, “Three-dimensional microfabrication with two-photon-absorbed photopolymerization,” *Opt. Lett.*, vol. 22, no. 2, pp. 132–134, 1997.
- [82] J. L. Bredas, C. Adant, P. Tackx, A. Persoons, and B. M. Pierce, “Third-Order Nonlinear Optical Response in Organic Materials: Theoretical and Experimental Aspects,” *Chem. Rev.*, vol. 94, no. 1, pp. 243–278, 1994.
- [83] A. M. Larson, “Multiphoton microscopy,” *Nat. Photonics*, vol. 5, no. 1, pp. 1–17, 2010.
- [84] S. Juodkazis, M. Watanabe, M. Miwa, S. Matsuo, H. Misawa, and J. Nishii, “Microfabrication in Silica,” *Opt. Lett.*, vol. 26, no. 5, pp. 277–279, 2001.
- [85] S. Backus, C. G. Durfee, M. M. Murnane, and H. C. Kapteyn, “High power ultrafast lasers,” *Rev. Sci. Instrum.*, vol. 69, no. 3, pp. 1207–1223, 1998.
- [86] J. Bonse, K.-W. Brzezinka, and A. J. Meixner, “Modifying single-crystalline silicon by femtosecond laser pulses: an analysis by micro Raman spectroscopy, scanning laser microscopy and atomic force microscopy,” *Appl. Surf. Sci.*, vol. 221, no. 1, pp. 215–230, 2004.
- [87] K. König, P. T. C. So, W. W. Mantulin, and E. Gratton, “Cellular response to near-

- infrared femtosecond laser pulses in two-photon microscopes,” *Opt. Lett.*, vol. 22, no. 2, pp. 135–136, 1997.
- [88] C.-Y. Dong, K. Koenig, and P. So, “Characterizing point spread functions of two-photon fluorescence microscopy in turbid medium,” *J. Biomed. Opt.*, vol. 8, no. 3, p. 450, 2003.
- [89] A. Jechow, M. Seefeldt, H. Kurzke, A. Heuer, and R. Menzel, “Enhanced two-photon absorption using true thermal light,” *Nat. Photonics*, vol. 7, no. 12, pp. 973–976, 2013.
- [90] U. Keller, “Ultrafast solid-state lasers,” *Springer*, vol. 46, pp. 33–167, 2007.
- [91] K. Venkatakrishnan, S. Jariwala, and B. Tan, “Maskless fabrication of nano-fluidic channels by two-photon absorption (TPA) polymerization of SU-8 on glass substrate,” *Opt. Express*, vol. 17, no. 4, pp. 2756–2762, 2009.
- [92] M. Alaraby Salem and A. Brown, “Two-photon absorption of fluorescent protein chromophores incorporating non-canonical amino acids: TD-DFT screening and classical dynamics,” *Phys. Chem. Chem. Phys.*, vol. 17, no. 38, pp. 25563–25571, 2015.
- [93] R. Homma, B. Baker, L. Jin, O. Garaschuk, A. Konnerth, L. Cohen, C. Bleau, M. Canepari, M. Djurisic, and D. Zecevic, “Wide-field and two-photon imaging of brain activity with voltage- and calcium-sensitive dyes,” *Methods Mol. Biol.*, vol. 489, pp. 43–79, 2009.
- [94] J. Torgersen, A. Ovsianikov, V. Mironov, N. Pucher, X. Qin, Z. Li, K. Cicha, T. Machacek, R. Liska, V. Jantsch, and J. Stampfl, “Photo-sensitive hydrogels for three-dimensional laser microfabrication in the presence of whole organisms,” *J.*

- Biomed. Opt.*, vol. 17, no. 10, p. 105008, 2012.
- [95] V. C. Pinto, P. J. Sousa, V. F. Cardoso, and G. Minas, “Optimized SU-8 processing for low-cost microstructures fabrication without cleanroom facilities,” *Micromachines*, vol. 5, no. 3, pp. 738–755, 2014.
- [96] P. Eravuchira, “Lithographic micro- and nanostructuring of SU-8 for biotechnological applications,” PhD Thesis, Rovira University, 2015.
- [97] A. L. Bogdanov, “SU-8 negative photoresist for optical mask manufacturing,” *Proc. SPIE*, vol. 3999, no. Cd, pp. 1215–1225, 2000.
- [98] H. Lorenz, M. Despont, N. Fahrni, J. Brugger, P. Vettiger, and P. Renaud, “High-aspect-ratio, ultrathick, negative-tone near-UV photoresist and its applications for MEMS,” *Sensors Actuators A Phys.*, vol. 64, no. 1, pp. 33–39, 1998.
- [99] C.-M. Lim, S. Kim, Y. Hwang, J. Choi, K. Ban, S. Cho, J. Jung, E. Kang, H. Lim, H. Kim, S. Moon, “Positive and negative tone double patterning lithography for 50nm flash memory,” *SPEI 31th international symposium on advanced lithography*, vol. 6154, pp. 615410–615418, 2006.
- [100] C. Lv, H. Xia, W. Guan, Y. Sun, Z. Tian, T. Jiang, Y. Wang, Y. Zhang, Q. Chen, K. Ariga, Y. Yu, and H. Sun, “Integrated optofluidic-microfluidic twin channels: toward diverse application of lab-on-a-chip systems,” *Sci. Rep.*, vol. 6, no. 1, p. 19801, 2016.
- [101] D. C. Duffy, J. C. McDonald, O. J. A. Schueller, and G. M. Whitesides, “Rapid prototyping of microfluidic systems in poly(dimethylsiloxane),” *Anal. Chem.*, vol. 70, no. 23, pp. 4974–4984, 1998.
- [102] R. F. Shepherd, P. Panda, Z. Bao, K. Sandhage, T. Hatton, J. Lewis, and P. Doyle,

- “Stop-flow lithography of colloidal, glass, and silicon microcomponents,” *Adv. Mater.*, vol. 20, no. 24, pp. 4734–4739, 2008.
- [103] S. Tang and G. Whitesides, “Basic microfluidic and soft lithographic techniques,” *Optofluidics Fundam. Devices, Appl.*, pp. 7–32, 2010.
- [104] M. Matteucci, M. Triches, G. Nava, A. Kristensen, M. Pollard, K. Berg, and R. Taboryski, “Fiber-based, injection-molded optofluidic systems: Improvements in assembly and applications,” *Micromachines*, vol. 6, no. 12, pp. 1971–1983, 2015.
- [105] G. M. Whitesides, E. Ostuni, X. Jiang, and D. E. Ingber, “Soft Lithography in Biology,” *Annu. Rev. Biomed. Eng.*, vol. 3, pp. 335–73, 2001.
- [106] A. Mata, A. J. Fleischman, and S. Roy, “Characterization of Polydimethylsiloxane (PDMS) Properties for Biomedical Micro/Nanosystems,” *Biomed. Microdevices*, vol. 7, no. 4, pp. 281–293, 2005.
- [107] A. Fallis, “Etch Rates for Micromachining Processing,” *J. Chem. Inf. Model.*, vol. 53, no. 9, pp. 1689–1699, 2013.
- [108] M. A. Green, “Self-consistent optical parameters of intrinsic silicon at 300 K including temperature coefficients,” *Sol. Energy Mater. Sol. Cells*, vol. 92, no. 11, pp. 1305–1310, 2008.
- [109] SCHOTT Technical Glass Solutions GmbH Instruction Handbook, *Scott AG*, pp. 1–32, 2009.
- [110] J.-Y. Jin, S. Yoo, J.-S. Bae, and Y.-K. Kim, “Deep wet etching of borosilicate glass and fused silica with dehydrated AZ4330 and a Cr/Au mask,” *J. Micromechanics Microengineering*, vol. 24, no. 1, p. 15003, 2014.
- [111] R. Martinez-Duarte, “SU-8 photolithography as a toolbox for carbon MEMS,”

- Micromachines*, vol. 5, no. 3, pp. 766–782, 2014.
- [112] K. M. Davis, K. Miura, N. Sugimoto, and K. Hirao, “Writing waveguides in glass with a femtosecond laser,” *Opt. Lett.*, vol. 21, no. 21, pp. 1729–1731, 1996.
- [113] S. M. Eaton, H. Zhang, L. Ng, J. Li, W. Chen, S. Ho, and P. Herman “Transition from thermal diffusion to heat accumulation in high repetition rate femtosecond laser writing of buried optical waveguides,” *Opt. Express*, vol. 16, no. 13, pp. 9443–9458, 2008.
- [114] A. Y. Vorobyev and C. Guo, “Enhanced absorptance of gold following multipulse femtosecond laser ablation,” *Phys. Rev. B*, vol. 72, no. 19, p. 195422, 2005.
- [115] K. Miura, J. Qiu, H. Inouye, T. Mitsuyu, and K. Hirao, “Photowritten optical waveguides in various glasses with ultrashort pulse laser,” *Appl. Phys. Lett.*, vol. 71, no. 23, pp. 3329–3331, 1997.
- [116] K. C. Vishnubhatla, J. Clark, G. Lanzani, R. Ramponi, R. Osellame, and T. Virgili, “Ultrafast optofluidic gain switch based on conjugated polymer in femtosecond laser fabricated microchannels,” *Appl. Phys. Lett.*, vol. 94, no. 4, p. 41123, 2009.
- [117] Y. Bellouard, A. Said, M. Dugan, and P. Bado, “Fabrication of high-aspect ratio, micro-fluidic channels and tunnels using femtosecond laser pulses and chemical etching,” *Opt. Express*, vol. 12, no. 10, pp. 2120–2129, 2004.
- [118] Y. Cheng, K. Sugioka, K. Midorikawa, M. Masuda, K. Toyoda, M. Kawachi, and K. Shihoyoma, “Control of the cross-sectional shape of a hollow microchannel embedded in photostructurable glass by use of a femtosecond laser,” *Opt. Lett.*, vol. 28, no. 1, pp. 55–57, 2003.
- [119] C. B. Schaffer, A. Brodeur and E. Mazur, “Laser-induced breakdown and damage

- in bulk transparent materials induced by tightly focused femtosecond laser pulses,” *Meas. Sci. Technol.*, vol. 12, no. 11, pp. 1784-1794, 2001.
- [120] C. B. Schaffer, A. Brodeur, J. F. García, and E. Mazur, “Micromachining bulk glass by use of femtosecond laser pulses with nanojoule energy,” *Opt. Lett.*, vol. 26, no. 2, pp. 93–95, 2001.
- [121] M. Kim, D. J. Hwang, H. Jeon, K. Hiromatsu, and C. P. Grigoropoulos, “Single cell detection using a glass-based optofluidic device fabricated by femtosecond laser pulses,” *Lab Chip*, vol. 9, no. 2, pp. 311–318, 2009.
- [122] F. Bragheri, P. Minzioni, R. Martinez Vazquez, N. Bellini, P. Paiè, C. Mondello, R. Ramponi, I. Cristianib, and R. Osellame, “Optofluidic integrated cell sorter fabricated by femtosecond lasers,” *Lab Chip*, vol. 12, no. 19, pp. 3779–3784, 2012.
- [123] J. Kruger, K. Singh, A. O’Neill, C. Jackson, A. Morrison, and P. O’Brien, “Development of a microfluidic device for fluorescence activated cell sorting,” *J. Micromechanics Microengineering*, vol. 12, no. 4, p. 486, 2002.
- [124] Y. Liao, J. Song, E. Li, Y. Luo, Y. Shen, D. Chen, Y. Cheng, Z. Xu, K. Sugioka, and K. Midorikawa, “Rapid prototyping of three-dimensional microfluidic mixers in glass by femtosecond laser direct writing,” *Lab Chip*, vol. 12, no. 4, pp. 746–749, 2012.
- [125] Y. Hanada, K. Sugioka, and K. Midorikawa, “Highly sensitive optofluidic chips for biochemical liquid assay fabricated by 3D femtosecond laser micromachining followed by polymer coating,” *Lab Chip*, vol. 12, no. 19, pp. 3688-3693, 2012.
- [126] X. M. Liu, Y. Chung, A. Lin, W. Zhao, K. Q. Lu, Y. S. Wang, and T. Y. Zhang,

- “Tunable and switchable multi-wavelength erbium-doped fiber laser with highly nonlinear photonic crystal fiber and polarization controllers,” *Laser Phys. Lett.*, vol. 5, no. 12, p. 904, 2008.
- [127] K. K. Chow, C. Shu, C. Lin, and A. Bjarklev, “Polarization-insensitive widely tunable wavelength converter based on four-wave mixing in a dispersion-flattened nonlinear photonic Crystal fiber,” *IEEE Photonics Technol. Lett.*, vol. 17, no. 3, pp. 624–626, 2005.
- [128] P. A. Andersen, T. Tokle, Y. Geng, C. Peucheret, and P. Jeppesen, “Wavelength conversion of a 40-Gb/s RZ-DPSK signal using four-wave mixing in a dispersion-flattened highly nonlinear photonic crystal fiber,” *IEEE Photonics Technol. Lett.*, vol. 17, no. 9, pp. 1908–1910, 2005.
- [129] L. Fu and M. Gu, “Double-clad photonic crystal fiber coupler for compact nonlinear optical microscopy imaging,” *Opt. Lett.*, vol. 31, no. 10, pp. 1471–1473, 2006.
- [130] K. Saitoh and M. Koshiba, “Highly nonlinear dispersion-flattened photonic crystal fibers for supercontinuum generation in a telecommunication window,” *Opt. Express*, vol. 12, no. 10, pp. 2027–2032, 2004.
- [131] J. M. Dudley and J. R. Taylor, “Ten years of nonlinear optics in photonic crystal fibre,” *Nat. Photonics*, vol. 3, pp. 85-90, 2009.
- [132] F. Poli, A. Cucinotta, S. Selleri, and A. H. Bouk, “Tailoring of flattened dispersion in highly nonlinear photonic crystal fibers,” *IEEE Photonics Technol. Lett.*, vol. 16, no. 4, pp. 1065–1067, 2004.
- [133] S. M. A. Razzak and Y. Namihira, “Proposal for Highly Nonlinear Dispersion-

- Flattened Octagonal Photonic Crystal Fibers,” *IEEE Photonics Technol. Lett.*, vol. 20, no. 4, pp. 249–251, 2008.
- [134] M. Vieweg, T. Gissibl, S. Pricking, B. T. Kuhlmeier, D. C. Wu, B. J. Eggleton, and H. Giessen, “Ultrafast nonlinear optofluidics in selectively liquid-filled photonic crystal fibers,” *Opt. Express*, vol. 18, no. 24, pp. 25232–25240, 2010.
- [135] S. A. Ranamukhaarachchi, C. Padeste, M. Dübner, U. O. Häfeli, B. Stoeber, and V. J. Cadarso, “Integrated hollow microneedle-optofluidic biosensor for therapeutic drug monitoring in sub-nanoliter volumes,” *Sci. Rep.*, vol. 6, pp. 1–10, 2016.
- [136] H. Zhu, I. White, J. Suter, P. Dale, and X. Fan, “Analysis of biomolecule detection with optofluidic ring resonator sensors,” *Opt. Express*, vol. 15, no. 15, pp. 9139–9146, 2007.
- [137] A. A. Yanik, M. Huang, O. Kamohara, A. Artar, T. Geisbert, J. Connor and H. Altu, “An optofluidic nanoplasmonic biosensor for direct detection of live viruses from biological media,” *Nano Lett.*, vol. 10, no. 12, pp. 4962–4969, 2010.
- [138] H. Li, Y. Guo, Y. Sun, K. Reddy, and X. Fan, “Analysis of single nanoparticle detection by using 3-dimensionally confined optofluidic ring resonators,” *2010 Asia Commun. Photonics Conf. Exhib. ACP 2010*, vol. 18, no. 24, pp. 324–325, 2010.
- [139] A. R. Clapp, I. L. Medintz, J. M. Mauro, B. R. Fisher, M. G. Bawendi, and H. Mattoussi, “Fluorescence Resonance Energy Transfer Between Quantum Dot Donors and Dye-Labeled Protein Acceptors,” *J. Am. Chem. Soc.*, vol. 126, no. 1, pp. 301–310, 2004.
- [140] F. A. Kuypers, R. A. Lewis, M. Hua, M. Schott, D. Discher, J. Ernest, and B. H.

- Lubin, "Detection of Altered Membrane Phospholipid Asymmetry in Subpopulations of Human Red Blood Cells Using Fluorescently Labeled Annexin V," *Blood*, vol. 87, no. 3, pp. 1179–1187, 1996.
- [141] X. Wu, H. Liu, J. Liu, K. Haley, J. Treadway, J. Larson, N. Ge, F. Peale, M. Bruchez, "Immunofluorescent labeling of cancer marker Her2 and other cellular targets with semiconductor quantum dots," *Nat. Biotechnol.*, vol. 21, no. 1, pp. 41–46, 2003.
- [142] A. Syahir, K. Usui, K. Tomizaki, K. Kajikawa, and H. Mihara, "Label and Label-Free Detection Techniques for Protein Microarrays," *Microarrays*, vol. 4, no. 2, pp. 228–244, 2015.
- [143] H. Li and X. Fan, "Characterization of sensing capability of optofluidic ring resonator biosensors," *Appl. Phys. Lett.*, vol. 97, no. 1, 2010.
- [144] J. D. Williams, "Study on the postbaking process and the effects on UV lithography of high aspect ratio SU-8 microstructures," *J. Micro/Nanolithography, MEMS, MOEMS*, vol. 3, no. 4, p. 563, 2004.
- [145] T. Kozawa, "Nanochemistry of chemically amplified resists for extreme ultraviolet lithography", *SPEI Newsroom*, p. 004273, 2012.
- [146] R. P. Conditions, "Features of KMPR 1000 Series," pp. 3–4, 2015.
- [147] Microchem, "Negative Tone Photoresist Formulations 2– 25," [http // www. Microchem. com/products/pdf/SU8—2-25](http://www.microchem.com/products/pdf/SU8-2-25), pp. 1–4, 2002.
- [148] Microchem, "SU-8 2000 Permanent Epoxy Negative Photoresist," *Process. Guidel.*, 2015.

- [149] D. Ozcelik, H. Cai, K. Leake, R. Hawkins, and H. Schmidt, "Optofluidic bioanalysis: fundamentals and applications.," *Nano. Photon.*, vol. 6, pp. 647-661 2017.
- [150] D. Rabus, "Optofluidic systems technology," *Walter de Gruyter GmbH & Co KG*, vol. 5, pp. 166–183, 2014.
- [151] A. Hawkins and H. Schmidt, "Handbook of Optofluidics," *CRC Press*, vol. 7, pp 7-1-7, 2010.
- [152] P. Lu, L. Men, K. Sooley, and Q. Chen, "Tapered fiber Mach-Zehnder interferometer for simultaneous measurement of refractive index and temperature," *Appl. Phys. Lett.*, vol. 94, no. 13, pp. 1–3, 2009.
- [153] D. Yuan, Y. Dong, Y. Liu, and T. Li, "Mach–Zehnder interferometer biochemical sensor based on silicon–on–insulator rib waveguide with large cross section", vol. 15, no. 9. p. 21500–21517, 2015.
- [154] S. K. Sia and G. M. Whitesides, "Microfluidic devices fabricated in Poly(dimethylsiloxane) for biological studies," *Electrophoresis*, vol. 24, no. 21, pp. 3563–3576, 2003.
- [155] D. Yuan, Y. Dong, Y. Liu, and T. Li, "Mach-Zehnder interferometer biochemical sensor based on silicon-on-insulator rib waveguide with large cross section," *Sensors (Switzerland)*, vol. 15, no. 9, pp. 21500–21517, 2015.
- [156] J. Romble, "CRC Handbook of chemistry and physics, 98th edition" *CRC press*, 2017.
- [157] W. Song and D. Psaltis, "Optofluidic membrane interferometer: An imaging method for measuring microfluidic pressure and flow rate simultaneously on a

- chip,” *Biomicrofluidics*, vol. 5, no. 4, pp. 44110–44111, 2011.
- [158] W. Song and D. Psaltis, “Optofluidic pressure sensor based on interferometric imaging,” *Opt. Lett.*, vol. 35, no. 21, pp. 3604–3606, 2010.
- [159] N. T. Nguyen, S. Lassemono, F. A. Chollet, and C. Yang, “Interfacial tension measurement with an optofluidic sensor,” *IEEE Sens. J.*, vol. 7, no. 5, pp. 692–697, 2007.
- [160] S. Michel, F. Lemarquis, and M. Lequime, “Determination of thermal and elastic coefficients of optical thin-film materials,” *Adv. Opt. Thin Film. II*, vol. 7101, pp. 1–11, 2008.
- [161] B. J. K. Davis, C. X. Li, and K. E. Nachman, “A Literature Review of the Risks and Benefits of Consuming Raw and Pasteurized Cow’s Milk,” *Johns Hopkins Cent. a Livable Futur.*, pp. 1–36, 2014.
- [162] C. Greenhill, “Nutrition: drinking cow’s milk alters vitamin D and iron stores in young children.,” *Nat. Rev. Endocrinol.*, vol. 9, no. 3, p. 126, 2013.
- [163] Y. Vandenplas and K. Plaskie, “Optimizing nutrition in cow’s milk-sensitive enteropathy,” *Monatsschrift Kinderheilkd.*, vol. 151, no. 1, pp. 34–38, 2003.
- [164] C. Wilson, “Finding weight loss strategies that work in primary care.,” *Nat. Rev. Endocrinol.*, vol. 9, no. 3, p. 126, 2013.
- [165] O. Sadeghi, F. Aboufazeli, H. R. Lotfi Zadeh Zhad, M. Karimi, and E. Najafi, “Determination of Pb(II) Ions Using Novel Ion-Imprinted Polymer Magnetic Nanoparticles: Investigation of the Relation Between Pb(II) Ions in Cow’s Milk and Their Nutrition,” *Food Anal. Methods*, vol. 6, no. 3, pp. 753–760, 2013.
- [166] G. Bylund, “Dairy Processing Handbook,” *Tetra Pak*, pp. 1–442, 1995.

Bibliography

- [167] R. Aschaffenburg, “336. Surface activity and proteins of milk,” *J. Dairy Res.*, vol. 14, no. 3, pp. 316–329, 1946.
- [168] “original-almond-drink @ www.fatsecret.com.” .
- [169] B. H. Schwendel, T. Wester, P. Morel, M. Tavendale, C. Deadman, N. Shabolt, D. Otter, “Organic and conventionally produced milk—an evaluation of factors influencing milk composition,” *J. Dairy Sci.*, vol. 98, no. 2, pp. 721–746, 2015.
- [170] S. Stocker, F. Foschum, P. Krauter, F. Bergmann, A. Hohmann, C. Scalfi, A. Kienle, “Broadband Optical Properties of Milk,” *Appl. Spectrosc.*, vol. 71, no. 5, pp. 951–962, 2016.
- [171] ESHA Research and USDA Database, “Nutrition facts of milk.” <http://nutrition.healthgrove.com/d/c/Milks>.